From Greenhouse to Icehouse: Understanding Earth's Climate Extremes Through Models and Proxies

Clay Richard Tabor

A dissertation submitted in partial fulfillment
of the requirements for the degree of
Doctor of Philosophy
(Geology)
in the University of Michigan
2016

Doctoral Committee:

Professor Chris J. Poulsen, Chair
Associate Professor Jeremy N. Bassis
Associate Professor Brian K. Arbic
Senior Scientist David Pollard

Acknowledgements

Foremost, I would like to thank my advisor Chris Poulsen for his exceptional mentoring throughout my time as a graduate student. My accomplishments over the past five and a half years were the result of his continual assistance, understanding, and friendship. I look forward to our continuing and future collaborations.

I would also like to thank my collaborator and committee member Dave Pollard. His impressive body of work and guidance were the foundation for my research; my dissertation would not have been possible without his help. To my other committee members, Brian Arbic and Jeremy Bassis, who graciously gave their time to many fruitful conversations, I would like to thank you for your help improving this dissertation. Thanks to my other collaborators, Bette Otto-Bleisner, Nan Rosenbloom, and Dan Lunt, for sharing your experience and research with me; I am excited about our ongoing collaboration. I would like to thank the past and current members of the Climate Change Research Lab for their numerous discussions and friendship over the years. Ran Feng, Rich Fiorella, Louise Jeffery, Dan Horton, Jing Zhou, Adam Herrington, Nadja Insel, Sierra Petersen, Chris Skinner, Chana Tilevitz, Phoebe Aron, Alex Thompson, Hong Shen, and Dan Lowry, you all have kept the lab both entertaining and productive. Further I would like to thank Mike Messina for tolerating my Unix ignorance time and time again.

Beyond research, I am grateful to my friends. They have been a constant source of relaxation, entertainment, and support throughout my graduate career. I would not have made it this far without them. Finally, I would like to thank my family, especially my parents, who have always supported and believed in me, even when I clearly have no idea what I am doing. Thank you for reading!

Table of contents

Chapter 1

Chapter 2

Chapter 3

Chapter 4

Chapter 5

Chapter 6

List of figures

List of tables

Chapter 1: Introduction

1.1 Motivation

Within the last century, global temperatures have risen from nearly the coldest to warmest levels of the past 11,300 years (Marcott et al., 2013). Studies suggest that this warming, due in large part to anthropogenic greenhouse gas (GHG) emissions, will have profound impacts on all aspects of life over the next century regardless of realized GHG emission scenario (5th IPCC report). However, there remains uncertainty about Earth system sensitivity to changes in GHG concentrations (Rohling et al., 2012). Feedbacks and decadal variability within the exceptionally complex Earth system lead to a large range of model predictions and hinder our ability to accurately forecast the amplitude and heterogeneity of climate change into the next century and beyond (Knutti et al., 2010b).

One of the greatest difficulties about modeling future climate change is the unique nature of the problem. Civilization has not experienced this magnitude of CO_2 increase (Petit et al., 1999) and many of the climate responses will take centuries to unfold (Hansen et al., 1984). Observations only extend back a few hundred years, with relatively poor spatial coverage before the satellite era beginning in the 1970s. As a result, they provide limited data to benchmark climate models and little insight into how climate responds to large GHG forcing. Further, without sufficient records for calibration, climate models run the risk of being over-tuned to the short observation period, which might prevent them from accurately simulating the future climate state.

Paleoclimate research is a powerful method for testing climate model capability and understanding key periods in Earth's history (Taylor et al., 2012). Studying past greenhouse climates, such as the Cretaceous or Eocene, gives us the ability to better understand high CO_2 conditions (e.g. Poulsen et al., 1999; Lunt et al., 2012) while studying past glacial cycles provides insight into ice sheet stability (e.g. Pollard and DeConto, 2009; Abe-Ouchi et al., 2013). Specifically, modeling paleoclimates and comparing the outputs against proxy records provides a powerful tool for improving climate models and increasing confidence in climate projections

(Braconnot et al., 2012). In this dissertation, I take a model/proxy comparison approach toward solving global problems in paleoclimatology. By studying extreme conditions in Earth's past, I advance our understanding of Earth system responses to dramatically different forcings and assess the ability of climate models to accurately simulate these extreme conditions.

1.2 Methods

This dissertation utilizes General Circulation Models (GCMs) in combination with proxy reconstructions to explore extreme climates in Earth's past. All original data contributions come from GCM experiments. Here, I use the following Earth system models to explore the Quaternary (2.588 – 0.005 Ma) and Late Cretaceous (100 - 66 Ma): Global ENvironmental and Ecological Simulation of Interactive Systems **(**GENESIS) and Community Earth System Model (CESM) developed by the National Center for Atmospheric Research, and Hadley Centre Model (HadCM3L) developed by the UK Met Office. They are considered Earth system models and simulate the interactions of the atmosphere, ocean, land, ice, and biosphere. Models with the same underlying architecture have been used in IPCC reports and many other paleoclimate studies (e.g. Lunt et al., 2010; Zhou et al., 2012; Rosenbloom et al., 2013). The chosen model configurations are on the upper end of complexity commonly used for paleoclimate research. My results and those of previous studies (e.g. Horton et al., 2010) demonstrate the value of added complexity for solving the enigmas of paleoclimatology.

1.3 Background

1.3.1 Quaternary ice ages

Proxy evidence suggests that the past 2.7 Myr of Earth's history were some of the most climatically variable, cycling from interglacial conditions similar to the present-day to glacial conditions with massive Northern Hemisphere ice sheets. These glacial-interglacial cycles display quasi-cyclic variations on timescales of 10^4 to 10^6 years that loosely fluctuate with changes in Earth's orbit (Hays et al., 1976), which varies with degree of axial tilt (obliquity), direction of axial tilt (precession), and circularity (eccentricity). The most robust evidence for the cyclicity and trends in ice-volume through the Quaternary come from the combination of many benthic $\delta^{18}O$ records (Lisiecki and Raymo, 2005). These "stacked" records clearly show $\delta^{18}O$ variability at periods of eccentricity and obliquity, and provide details about Northern

Hemisphere ice sheet initiation, changes in ice age cycles through time, and global temperature trends. Yet despite the significance of these records, there remain uncertainties as to what the changes in $\delta^{18}O$ represent. $\delta^{18}O$ is the relative abundance of ^{18}O to ^{16}O. The $\delta^{18}O$ value recorded in foraminifera is a function of temperature and $\delta^{18}O$ of the water, which is dependent on $\delta^{18}O$ of the water source region and ice-volume. Most attempts to interpret the long-term $\delta^{18}O$ records agree that the ice-volume/temperature relationship changes through time (Bintanja et al., 2005) and could vary in response to different orbital forcings (Lisiecki et al., 2008). However, the spatial variability and physical mechanisms responsible for these differences remain poorly resolved.

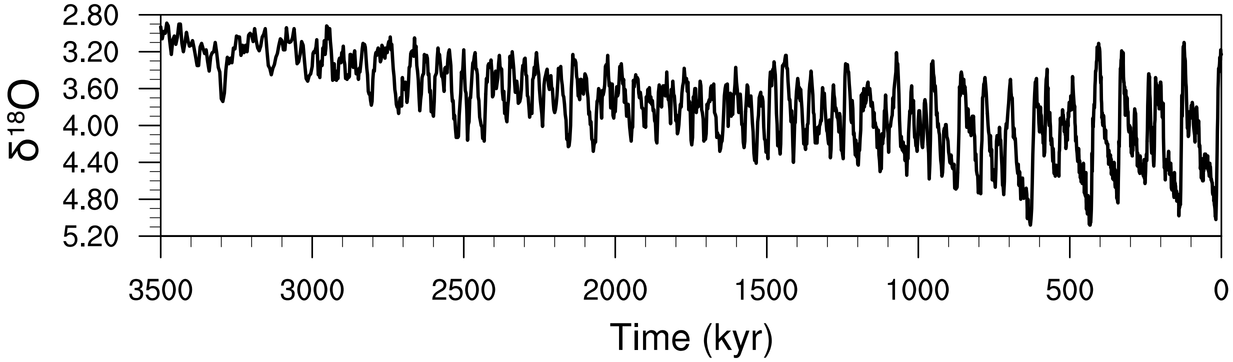

Figure 1.1: Oxygen isotope record of glacial cycles
The $\delta^{18}O$ stacked record of Lisiecki and Raymo (2005) from 3.5 Ma to present. The decrease in $\delta^{18}O$ over this period suggests a cooling trend while the increasing variability at lower frequencies is thought to represent more extreme glacial-interglacial cycles.

Even if we assume $\delta^{18}O$ records responds linearly to changes in ice-volume, our understandings of the glacial-interglacial cycles remain incomplete. The most widely held theory for the relationship between ice-volume and Earth's orbit comes from the calculations of Milutin Milankovitch who proposed that high-latitude summer insolation determines the amount of snow cover that can survive summer melt and consequently, the amount of ice-sheet growth or retreat (Milankovitch, 1941). However, there are many intriguing inconsistencies between Milankovitch's theory and proxy records of the Plio-Pleistocene. For instance, early Pleistocene (2.6 - 0.8 Ma) ice-volume proxy records vary almost exclusively at the frequency of the obliquity, despite the fact that changes in precession account for most of the variability in high-latitude summer insolation (Raymo and Nisancioglu, 2003; Figure 1.1). Further, a transition from 41 kyr to 100 kyr ice-volume cycles occurs between ~1.2 - 0.7 Ma with seemingly little change in orbital forcing or CO_2 (Clark et al., 2006). This transition, known as the mid-Pleistocene transition (MPT), is particularly perplexing since the 100 kyr ice-volume cycles of the late Pleistocene (0.8 – 0.117 Ma) suggest eccentricity forcing, which has almost no direct influence on insolation. Here, I use a complex Earth system model with a 3-dimensional thermomechanical ice sheet to help resolve these apparent paradoxes between Milankovitch theory and the Pleistocene ice-volume proxy records.

1.3.2 Cretaceous Greenhouse

Proxy temperature reconstructions define the Cretaceous as one of the warmest periods of the past 140 Ma. Throughout much of the Late Cretaceous (100-66 Ma), climate was characterized by a reduced equator-to-pole temperature gradient (Huber et al., 2002) and dense vegetation extending into the polar regions (Upchurch et al., 1999). Warmth peaked during the Cenomanian-Turonian (100 - 90 Ma) when evidence suggests Earth was in a greenhouse state, free of polar ice sheets (MacLeod et al., 2013). Temperatures then cooled considerably into the Maastrichtian (72 – 66 Ma) (Friedrich et al., 2012; Linnert et al., 2014) with the possible appearance of land-ice (Miller et al., 2005); however, reconstructions suggest that temperatures remained significantly warmer than present-day (Upchurch et al., 2015).

The origins of the Late Cretaceous warmth and subsequent cooling are ambiguous. CO_2 reconstructions for the period have large uncertainty but most estimates suggest that CO_2 remained below 8x-preindustrial (2240 ppmv) during the Cenomanian-Turonian, with a mean estimate closer to 4x-preindustrial (Wang et al., 2014). This is concerning given the evidence for extreme warmth, especially if the warmth was entirely attributable to CO_2. The IPCC Representative Concentration Pathway 8.5 scenario has CO_2 concentrations exceeding 1120 ppm by the end of the century (5th IPCC report). If the Cretaceous can be considered an analog for the future, it suggests that model simulated Earth system sensitivity to CO_2 changes is too low, and hence, the models might be missing some key climate system feedbacks. However, the Cretaceous spanned from 140 – 66 Ma; there were many differences from present-day that potentially had substantial impacts on the climate system, besides CO_2 (Poulsen et al., 2003; Zhou et al., 2012; Hunter et al., 2013). For instance, other GHGs such as methane could have been in higher concentration during the Cretaceous due to greater prevalence of wetlands (Beerling et al., 2011). Heat transport, due to differences in the distribution of land and sea or tropical storms, might have helped transport heat poleward (Poulsen et al., 2001; Korty et al., 2008). Cloud microphysics also may have been different than in the present-day due to more pristine air having less cloud condensation nuclei (Kump and Pollard, 2008). Finally, Cretaceous vegetation likely had different properties during the Cretaceous, which might alter temperatures through different amounts of transporation (Boyce et al., 2010).

Climate models provide a unique way to test Earth system sensitivity to these differences between the Cretaceous and present-day, and to help determine if the Cretaceous can be labeled as an analog for a future, warmer world. Further, modeling the Cretaceous allows the opportunity to better understand proxy reconstructions. Here I use complex Earth system models with a compilation of Late Cretaceous temperature reconstructions to better understand the mechanisms responsible for climate change through the Cretaceous.

1.4 Outline

This dissertation consists of 6 chapters. Four results chapters (2-5) and a concluding chapter (6) follow this introductory chapter (1). Chapters 2-5 use the GENESIS GCM coupled with the BIOME4 vegetation model and Penn State University ice sheet model. To better understand the 41 kyr ice-volume cycles of the early Pleistocene, Chapter 2 focuses on the climate and land-ice responses to the independent orbital cycles of obliquity and precession. In contrast with traditional Milankovitch theory, I show that the ice-volume cycles are not a direct response to summer insolation. Instead, sea-ice and vegetation feedbacks amplify the ice-volume response to obliquity relative to precession. Chapter 3 extends these results by modeling the interactions of obliquity and precession on climate and ice-volume. Here I find that, in addition to climate feedbacks, seasonal offset of the precession insolation signal and differences in cycle duration are necessary to understand the contributions of obliquity and precession to the ice-volume response. The combination of these factors allow obliquity to have the dominant influence on ice-volume variability, which is in agreement with early Pleistocene δ^{18}O records (Lisiecki and Raymo, 2005). Chapter 4 explores the appearance of the 100 kyr ice-volume cycles that characterize the late Pleistocene. My research supports the hypothesis that a surface transition from regolith to crystalline bedrock in the high-latitudes of North America by multiple cycles of ice advance and retreat can explain the MPT (Clark and Pollard, 1998). Finally, I assess the cause of Late Cretaceous cooling through a multi-model/proxy comparison study in Chapter 5.

My results show that CESM and HadCM3L do a reasonably good job simulating the late Cretaceous sea surface temperature (SST) gradients. Further, model results suggest that the proxy identified Late Cretaceous cooling was mainly a result of CO_2 reduction, not changes in geography. In Chapter 6, I summarize my finding and provide avenues for future research.

1.5 Publications and abstracts resulting from this dissertation

Publications:

Tabor, C.R., Poulsen, C.J., and Pollard, D. (2014), Mending Milankovitch's theory: obliquity amplification by surface feedbacks, Clim. Past, doi:10.5194/cp-10-41-2014 (**Chapter 2**)

Tabor, C.R., Poulsen, C.J., and Pollard, D. (2015), How obliquity cycles powered early Pleistocene global ice-volume variability, Geophys. Res. Lett., doi:10.1002/2015GL063322 (**Chapter 3**)

Tabor, C.R. and Poulsen, C.J. (2015), Simulating the mid-Pleistocene transition through regolith removal, Earth Planet. Sci. Lett., doi:10.1016/j.epsl.2015.11.034 (**Chapter 4**)

Tabor, C.R., Poulsen, C.J., Lunt, D.J., Otto-Bliesner, B., Rosenbloom, N., and Markwick, P. (*in prep*) (2015), The contributions of paleogeography and CO_2 to Late Cretaceous Cooling: A multi-model/proxy comparison (**Chapter 5**)

Conference Abstracts:

Tabor, C.R., Poulsen, C.J., and Pollard, D. (2012), Modeling the North American ice sheet response to changes in precession and obliquity, American Geophysical Union Fall Meeting.

Tabor, C.R., Poulsen, C.J., and Pollard, D. (2013), Using a complex earth system model to replicate the ice volume signal of the early Pleistocene, American Geophysical Union Fall Meeting.

Rosenbloom, N., Otto-Bliesner, B., Esther, B., Lunt, D.J., Poulsen, C.J., and **Tabor, C.R.** (2014), CESM for deep time paleoclimate, Paleoclimate Modeling Intercomparison Project: Second General Meeting.

Lunt, D.J., Otto-Bliesner, B., Poulsen, C.J., Rosenbloom, N., and **Tabor, C.R.** (2014), Pre-Pliocene PMIP working group: results so far, and questions for discussion, Paleoclimate Modeling Intercomparison Project: Second General Meeting.

Tabor, C.R., Poulsen, C.J., Lunt, D.J., Otto-Bliesner, B., Rosenbloom, N., and Markwick, P.J. (2014), Simulating Cenomanian climate with the Community Earth System Model, The Geological Society of America Annual Meeting.

Tabor, C.R., Poulsen, C.J., and Pollard, D. (2014), The potential role of regolith in the mid-Pleistocene transition, American Geophysical Union Fall Meeting.

Tabor, C.R., Poulsen, C.J., Lunt, D.J., Otto-Bliesner, B., Rosenbloom, N., and Markwick, P.J. (2015), Simulating climate response to changes in paleogeography through the Cretaceous, CESM Workshop.

Peterson, S.V., **Tabor, C.R.**, Meyer, K.W., Lohmann, K.C., and Poulsen, C.J. (2015), Equator

To Pole in the Cretaceous: A comparison of clumped isotope data with CESM model runs, American Geophysical Union Fall Meeting.

Peterson, S.V., **Tabor, C.R.**, Carpenter, S.J., Meyer, K.W., Lohmann, K.C., and Poulsen, C.J. (2015), A Fresh Look: Salinity and Temperature of the Western Interior Seaway using the Clumped Isotope Paleothermometer, The Geological Society of America Annual Meeting.

Tabor, C.R., and Poulsen, C.J. (2015), The Role of Paleogeography and CO2 in Late Cretaceous Ocean Circulation, American Geophysical Union Fall Meeting.

Tabor, C.R., Poulsen, C.J., and Pollard, D. (2015), Using an Earth System Model to Better Understand Ice Sheet Variability Through the Pleistocene, American Geophysical Union Fall Meeting.

Bibliography

Beerling, D. J., and D. L. Royer (2011), Convergent Cenozoic CO_2 history, Nature Geosci, 4(7), 418–420, doi:10.1038/ngeo1186.

Bintanja, R., R. van de Wal, and J. Oerlemans (2005), Modelled atmospheric temperatures and global sea levels over the past million years, Nature, 437(7055), 125–128, doi:10.1038/nature03975.

Boyce, C. K., and J. E. Lee (2010), An exceptional role for flowering plant physiology in the expansion of tropical rainforests and biodiversity, Proc. Royal Soc. B: Bio. Sci., 277(1699), 3437–3443, doi:10.1080/00241160310004657.

Braconnot, P., S. P. Harrison, M. Kageyama, P. J. Bartlein, V. Masson-Delmotte, A. Abe-Ouchi, B. Otto-Bliesner, and Y. Zhao (2012), Evaluation of climate models using palaeoclimatic data, Nat. Clim. Change, 2(6), 417–424, doi:doi:10.1038/nclimate1456.

Clark, P. U., and D. Pollard (1998), Origin of the middle Pleistocene transition by ice sheet erosion of regolith, Paleoceanography, 13(1), 1–9.

Clark, P. U., D. Archer, D. Pollard, J. D. Blum, J. A. Rial, V. Brovkin, A. C. Mix, N. G. Pisias, and M. Roy (2006), The middle Pleistocene transition: characteristics, mechanisms, and implications for long-term changes in atmospheric pCO_2, Quat. Sci. Rev., 25(23-24), 3150–3184, doi:10.1016/j.quascirev.2006.07.008.

Hansen, J. et al. (1984) Climate sensitivity: analysis of feedback mechanisms. Climate Processes and climate sensitivity. AGU Geophysical Monograph 29, Maurice Ewing Volume 5. 130-163.

Hays, J. D., J. Imbrie, and N. J. Shackleton (1976), Variations in the Earth's orbit: Pacemaker of the ice ages, Science, 194, 1121-1132, doi: 10.1126/science.194.4270.1121

Horton, D. E., C. J. Poulsen, and D. Pollard (2010), Influence of high-latitude vegetation feedbacks on late Palaeozoic glacial cycles, Nature Geosci, 3(8), 572–577, doi:10.1038/ngeo922.

Huber, B. T., R. D. Norris, and K. G. MacLeod (2002), Deep-sea paleotemperature record of extreme warmth during the Cretaceous, Geology, 30(2), 123-126.

Hunter, S. J., A. M. Haywood, P. J. Valdes, J. E. Francis, and M. J. Pound (2013), Modelling equable climates of the Late Cretaceous: Can new boundary conditions resolve data–model discrepancies?, Palaeogeography, Palaeoclimatology, Palaeoecology, 392(C), 41–51, doi:10.1016/j.palaeo.2013.08.009.

Knutti, R., R. Furrer, C. Tebaldi, J. Cermak, and G. A. Meehl (2010), Challenges in Combining Projections from Multiple Climate Models, J. Climate, 23(10), 2739–2758, doi:10.1175/2009JCLI3361.1.

Korty, R. L., K. A. Emanuel, and J. R. Scott (2008), Tropical Cyclone–Induced Upper-Ocean Mixing and Climate: Application to Equable Climates, J. Climate, 21(4), 638–654, doi:10.1175/2007JCLI1659.1.

Kump, L. R., and D. Pollard (2008), Amplification of Cretaceous warmth by biological cloud feedbacks, Science, 320(5873), 195–195, doi:10.1126/science.1153883.

Linnert, C., Robinson, S. A., J. A. Lees, P. R. Brown, I. P. E. R.-Rodriguez, M. R. Petrizzo, F. Falzoni, K. Littler, J. E. A. Arz, and E. E. Russell, (2014), Evidence for global cooling in the

Late Cretaceous, Nat. Comm., 5, 1–7, doi:10.1038/ncomms5194.

Lisiecki, L. E., and M. E. Raymo (2005), A Pliocene-Pleistocene stack of 57 globally distributed benthic delta O-18 records, Paleoceanography, 20(1), doi:10.1029/2004PA001071.

Lisiecki, L. E., M. E. Raymo, and W. B. Curry (2008), Atlantic overturning responses to Late Pleistocene climate forcings, Nature, doi:10.1038/nature07425.

Lunt, D. J. et al. (2012), A model–data comparison for a multi-model ensemble of early Eocene atmosphere–ocean simulations: EoMIP, Clim. Past, 8(5), 1717–1736, doi:10.5194/cp-8-1717-2012-supplement.

Lunt, D. J., P. J. Valdes, T. D. Jones, A. Ridgwell, A. M. Haywood, D. N. Schmidt, R. Marsh, and M. Maslin (2010), CO_2-driven ocean circulation changes as an amplifier of Paleocene-Eocene thermal maximum hydrate destabilization, Geology, 38(10), 875–878, doi:10.1130/G31184.1.

MacLeod, K. G., B. T. Huber, A. J. Berrocoso, and I. Wendler (2013), A stable and hot Turonian without glacial $\delta^{18}O$ excursions is indicated by exquisitely preserved Tanzanian foraminifera, Geology, 41(10), 1083–1086, doi:10.1130/G34510.1.

Marcott, S. A., J. D. Shakun, P. U. Clark, and A. C. Mix (2013), A Reconstruction of Regional and Global Temperature for the Past 11,300 Years, Science, 339(6124), 1198–1201, doi:10.1126/science.1228026.

Milankovitch, M. (1941), Kanon der Erdbestrahlung und seine Andwendung auf das Eiszeiten-problem. R. Serbian Acad., Belgrade.Petit, J. R. et al. (1999), Climate and atmospheric history of the past 420,000 years from the Vostok ice core, Antarctica, Nature, 399(6735), 429–436, doi:10.1038/20859.

Poulsen, C. J., E. J. Barron, W. H. Peterson, and P. A. Wilson (1999), A reinterpretation of mid-Cretaceous shallow marine temperatures through model-data comparison, Paleoceanography, 14(6), 679-697.

Poulsen, C. J., E. J. Barron, M. A. Arthur, and W. H. Peterson (2001), Response of the mid-Cretaceous global oceanic circulation to tectonic and CO2 forcings, Paleoceanography, 16(6), 576-592.

Poulsen, C. J., A. S. Gendaszek, and R. L. Jacob (2003) Did the rifting of the Atlantic Ocean cause the Cretaceous thermal maximum?, Geology, 31, 473-476.

Raymo, M. E., and K. Nisancioglu (2003), The 41 kyr world: Milankovitch's other unsolved mystery, Paleoceanography, 18, 1011, doi:10.1029/2002PA000791.

Rohling, E. J. et al. (2013), Making sense of paleoclimate sensitivity, Nature, 1–10, doi:10.1038/nature11574.

Rosenbloom, N. A., B. L. Otto-Bliesner, E. C. Brady, and P. J. Lawrence (2013), Simulating the mid-Pliocene Warm Period with the CCSM4 model, Geosci. Model Dev., 6(2), 549–561, doi:10.5194/gmd-6-549-2013.

Stocker, T.F., D. Qin, G.-K. Plattner, M. Tignor, S.K. Allen, J. Boschung, A. Nauels, Y. Xia, V. Bex and P.M. Midgley (eds.) (2013) IPCC: Climate Change: The Physical Science Basis. Contribution of Working Group I to the Fifth Assessment Report of the Intergovernmental Panel on Climate Change, Cambridge University Press, Cambridge, United Kingdom and New York, NY, USA, 1535 pp.

Taylor, K. E., R. J. Stouffer, and G. A. Meehl (2012), An Overview of CMIP5 and the Experiment Design, Bull. Amer. Meteor. Soc., 93(4), 485–498, doi:10.1175/BAMS-D-11-00094.1.

Upchurch, G. R., B. L. Otto-Bliesner, and C.R. Scotese (1999), Terrestrial vegetation and its effects on climate during the latest Cretaceous, Geo. Soc. America, 332.

Upchurch, G. R., Jr, J. Kiehl, C. Shields, J. Scherer, and C. Scotese (2015), Latitudinal temperature gradients and high-latitude temperatures during the latest Cretaceous: congruence of geologic data and climate models, Geology, 43(8), 683–686, doi:10.1130/G36802.1.

Wang, Y., C. Huang, B. Sun, C. Quan, J. Wu, and Z. Lin (2014), Paleo-CO_2 variation trends and the Cretaceous greenhouse climate, Earth Sci. Rev., 129(C), 136–147, doi:10.1016/j.earscirev.2013.11.001.

Zhou, J., C. J. Poulsen, N. Rosenbloom, C. Shields, and B. Briegleb (2012), Vegetation-climate interactions in the warm mid-Cretaceous, Clim. Past, 8(2), 565–576, doi:10.5194/cp-8-565-2012.

Chapter 2: Mending Milankovitch Theory: Obliquity Amplification by Surface Feedbacks

2.1 Abstract

Milankovitch theory states that orbitally induced changes in high-latitude summer insolation dictate the waxing and waning of ice-sheets. Accordingly, precession should dominate the ice-volume response because it most strongly modulates summer insolation. However, Early Pleistocene (2.588-0.781 Ma) ice-volume proxy records vary almost exclusively at the frequency of the obliquity cycle. To explore this paradox, we use an Earth system model coupled with a dynamic ice-sheet to separate the climate responses to idealized transient orbits of obliquity and precession that maximize insolation changes. Our results show that positive surface albedo feedbacks between high-latitude annual-mean insolation, ocean heat flux and sea-ice coverage, and boreal forest/tundra exchange enhance the ice-volume response to obliquity forcing relative to precession forcing. These surface feedbacks, in combination with modulation of the precession cycle power by eccentricity, help explain the dominantly 41 kyr cycles in global ice volume of the Early Pleistocene.

2.2 Introduction

Paleoclimate proxy records often display variations on timescales of 10^4 to 10^6 years. These climate variations, known as Milankovitch cycles, are quasi-cyclic. They are attributed to the direct and combined effects of changes in Earth's degree of axial tilt (obliquity), direction of axial tilt (precession), and circularity of orbit (eccentricity) (Hays et al., 1976). Milankovitch cycles are thought to be responsible for the growth and retreat of the large Northern Hemisphere (NH) ice sheets that characterize the Pleistocene through the influence of Earth's three orbital / rotational parameters on high-latitude summer insolation. According to Milankovitch theory, times of high (low) summer insolation produce high (low) rates of summer melting, leading to NH ice-sheet retreat (growth). This theory is the most widely accepted explanation for the strong correlation between ice-volume proxy records and orbital variations (Hays et al., 1976).

One of the most intriguing inconsistencies between Milankovitch theory and proxy records is the lack of a strong precession signal in Early Pleistocene (2.588-0.781 Ma) ice-volume proxies (i.e. benthic δ^{18}O from sediment cores), despite the fact that precession accounts for most of the variability in high-latitude summer insolation (Raymo and Nisancioglu, 2003). While the orbital influences of precession/eccentricity can produce a high-latitude (60-75°N) May, June, July (MJJ) average insolation amplitude that is more than 2.5 times that of obliquity for the cycle extremes of the Pleistocene, the power spectra of the Early Pleistocene δ^{18}O sediment records show almost no variability at the precession cycle frequency (~21 kyr). Instead, the bulk of the signal strength appears at the obliquity cycle frequency (~41 kyr) (Lisiecki and Raymo, 2005).

This apparent failure of Milankovitch theory has led to new hypotheses for how orbital cycles influence ice-volume. The recognition that obliquity has a larger influence on the summer half-year meridional insolation gradient, defined as the 25 to 70°N insolation difference averaged over the period between vernal and autumnal equinoxes, than precession has led to the suggestion that variations in gradient-driven northward moisture fluxes enhance ice-sheet sensitivity (Raymo and Nisancioglu, 2003). Alternatively, it has been proposed that changes in the integrated summer energy, the total insolation received over the summer half-year period, may drive changes in ice volume (Huybers, 2006). Though precession has a substantial influence on summer insolation strength, because summer insolation amplitude and summer duration are anti-correlated, the changes in integrated summer energy resulting from variations in precession are smaller than the changes in integrated summer energy resulting from variations in obliquity. Finally, it has been suggested that precessional variations in marine δ^{18}O records are damped because precession insolation forcing is out-of-phase between hemispheres, potentially causing simultaneous (and partially offsetting) ice-sheet growth and retreat (Raymo et al., 2006; Lee and Poulsen, 2009). Despite these numerous hypotheses, there is no strong consensus as to the cause of the Early Pleistocene δ^{18}O signal.

Here we employ an Earth system model asynchronously coupled with a thermo-mechanical ice-sheet to better understand the differences in climate response to changes in precession and obliquity. We examine the high-latitude climate response to insolation forcing through a sensitivity analysis in which we separate the system responses to obliquity and precession. Our results demonstrate that internal climate feedbacks not considered in Milankovitch theory help explain the relatively strong obliquity signal observed in the Early Pleistocene δ^{18}O sediment records.

2.3 Methods

In this study, we use an Earth system model consisting of the GENESIS 3.0 atmospheric global climate model (AGCM) and land-surface model with a slab ocean coupled to a thermo-mechanical sea-ice model (Pollard and Thompson, 1997), the Pennsylvania State University ice-sheet model (Pollard and DeConto, 2012), and the BIOME4 vegetation model (Kaplan et al., 2003). To gain a better understanding of the climate feedbacks and ice dynamics associated with changes in orbital configuration, we design two sets of transient orbit experiments, one without an ice-sheet model (climate-only) and one with an ice-sheet model (climate-ice sheet). For each set of experiments, we run two transient orbital configurations in which either precession or obliquity systematically varies through a full orbital cycle (Table 2.1) with ranges representing extremes of the Pleistocene (Berger and Loutre, 1991). In our experiments, obliquity and precession cycles are 40 and 20 kyrs respectfully, slightly less than the known durations of 41 and 21 kyrs, for computational efficiency and ease of comparison (DeConto and Pollard 2003; Horton and Poulsen 2009). The ice-sheet model is run over a domain consisting of Greenland and North America at latitudes greater than 40°N. Since our focus is the role of orbital configuration, greenhouse gas concentrations (GHG) are fixed with values representing averages of the last 400 kyr (Petit et al., 1999; Bender, 2002) (CO_2=230 ppmv, CH_4=520 ppbv, N_2O=250 ppbv). All simulations use modern continental arrangement and start with modern ice-sheet extents. Resolutions for the AGCM, land surface, and ice-sheet models are T31 (~3.75 X 3.75°), 2 X 2°, and 0.5 X 0.25°, respectively. We decrease high Alaskan elevations in our simulations to prevent excessive ice build-up caused by the inability of the AGCM to capture valley ablation in Alaska (Marshall and Clarke, 1999). For these experiments, no floating ice or grounding-line advance into water is allowed in the ice-sheet model. Sea level is lowered by 275 m relative to modern to allow ice-sheet growth over the Hudson Bay and continental shelf. We found ~275 m to be the smallest amount of sea level lowering required to prevented flooding of the Hudson

Experiment	Obliquity	Precession	Eccentricity
OBL	22.079° - 24.538°	NA	0
PRE	23.3085°	0° – 360°	0.056596

Table 2.1: Orbital configurations

Bay when considering isostatic subsidence. The sea level lowering of 275 m has little influence elsewhere in the model because this is a terrestrial ice model with no explicit marine physics.

Because response times of the atmosphere and ice sheets differ by several orders of magnitude, we apply an asynchronous technique to couple the AGCM and the ice-sheet model (Birchfield et al., 1981). This process involves running the AGCM for short durations of 20 years, passing AGCM outputs to the ice-sheet model, running the ice-sheet model for longer durations of 2.5 kyr, and updating the AGCM with new topography and land-surface type. We use an average of the final 10 years of AGCM outputs to force the ice-sheet model. Due to the continuous nature of the orbital changes and the rapid response time of the slab ocean, 10 years of spin-up prior to the averaging period is sufficient to produce near equilibrium climate states. Herrington and Poulsen (2011) show that ice-sheet volume is sensitive to the asynchronous coupling period due to ice albedo and atmospheric circulation feedbacks. Here the model produces fairly continuous ice-volume and area responses to the transient orbital forcings, which suggests our coupling time is sufficiently small to capture the majority of the transient climate signal. In the ice-sheet model, we implement an insolation/temperature melt (ITM) scheme (van den Berg, 2008) calculated using AGCM outputs instead of the default positive degree-day melt (PDD) scheme (Pollard and DeConto, 2012). Robinson et al. (2010) find that the ITM approach produces greater and more realistic ice-sheet sensitivity in transient climate experiments than the PDD approach, making the ITM scheme preferable for paleoclimate simulations.

We run all ice-sheet experiments for 160 kyr model years, representing 4 cycles of obliquity and 8 cycles of precession. The first 40 kyr model years are not considered in our analysis since the ice sheets are still equilibrating during that time. Subsequent cycles are averaged to simplify the results. Because orbits with high eccentricity and transient precession cause significant changes in seasonal duration, we convert monthly AGCM outputs from a Gregorian calendar to an angular calendar using the methods detailed in Pollard and Reusch (2003). All monthly and seasonal analyses use the converted angular calendar outputs. For example, here June refers to the angular month most temporally similar to June in the Gregorian calendar. Furthermore, for our results we define high-latitude insolation as the shortwave radiation received at the top of the atmosphere between 60-75°N. Summer insolation is the average insolation of the angular calendar months May, June, and July. While our results focus mainly on the high-latitudes of North America because it is encompassed by ice sheet domain, the same general climate responses also occur in the high-latitudes of Europe.

2.4 Results

2.4.1 Climate-only experiments

Our initial analysis examines the climate response to transient cycles of obliquity and precession in absence of dynamic ice sheets. Model results show that differences in the ocean and vegetation feedbacks to the cycles of obliquity and precession produce greater climate sensitivity to insolation forcing from obliquity (described below). This climate sensitivity difference is due in part to the influence of obliquity-controlled variations in annual-mean insolation on the high-latitude ocean. The amount of absorbed insolation by the high-latitude ocean is mainly controlled by the amount of surface incident insolation and sea-ice cover. Because the obliquity cycle generates variations in annual-mean insolation, the high-latitude oceans absorb a greater range of insolation annually from obliquity than precession (Figure 2.1).

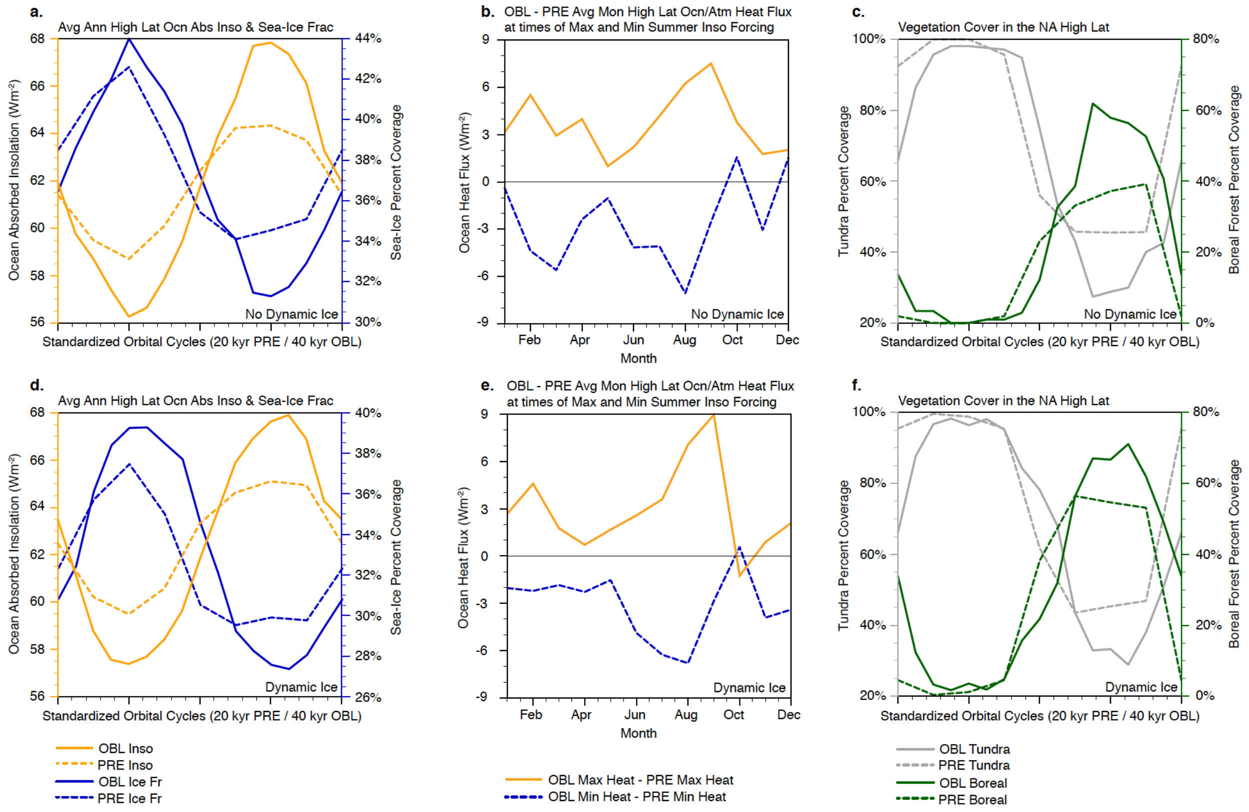

Figure 2.1: High-latitude climate feedbacks to orbital forcing
a) Annual-mean ocean-absorbed insolation (Wm^{-2}) and sea-ice coverage (%) between 60-75°N through time for the climate-only experiments. b) Differences in monthly average sensible + latent heat flux (Wm^{-2}) over the ocean between 60-75°N during the maximum and minimum

high-latitude summer insolation forcing from obliquity and precession for the climate-only experiments. c) Annual-mean coverage (%) of tundra and boreal forest over North America between 60-75°N through time for the climate-only experiments. d) Annual-mean ocean-absorbed insolation (Wm^{-2}) and sea-ice coverage (%) between 60-75°N through time for climate-ice sheet experiments. e) Differences in monthly average sensible + latent heat flux (Wm^{-2}) over the ocean between 60-75°N during the maximum and minimum high-latitude summer insolation forcing from obliquity and precession for climate-ice sheet experiments. f) Annual-mean coverage (%) of tundra and boreal forest over North America between 60-75°N through time for climate-ice sheet experiments. Cycle lengths were standardized and aligned by peak summer insolation in a), c), d), and f) to more easily compare the 40 kyr obliquity cycle with the 20 kyr precession cycle. In a) and d), the annual-mean insolation (orange lines) and sea-ice coverage (blue lines) amplitudes are greater over the cycle of obliquity (solid lines) than the cycle of precession (dashed lines). The greater annual-mean ocean-absorbed insolation causes the high-latitude ocean to emit a greater range of heat to the atmosphere for the obliquity cycle, which is illustrated in b) and e) as the difference (obliquity minus precession) in ocean/atmosphere heat flux for the maximum summer insolation orbit (solid orange) and the minimum summer insolation orbit (dashed blue). High-latitude vegetation change is also more influenced by obliquity than precession. In c) and f), obliquity (solid lines) produces a greater transition between tundra (gray lines) and boreal forest (green lines) than precession (dashed lines).

Changes in the amount of ocean-absorbed insolation modify the timing of sea-ice growth and retreat (Figure 2.1). Sea-ice coverage produces a positive feedback with ocean-absorbed insolation because of the albedo difference between ocean and ice. The annual-mean insolation signal of obliquity causes the change in ocean-absorbed insolation due to obliquity to be greater than those due to precession, resulting in a larger sea-ice response (Figure 2.1). Direct insolation also accounts for some of the sea-ice melting. However, the strong correlation between annual-absorbed insolation and seasonal sea-ice coverage suggests the direct insolation signal is of less importance. The contrast in sea-ice coverage is particularly apparent during spring and fall (not shown). For example, total April sea-ice area varies by ~2,065,900 km^2 through an obliquity cycle but only ~1,340,300 km^2 through a precession cycle, a difference of ~43%. Interestingly, the sea-ice difference does not lead to a large cloud albedo response. In April, when the difference in sea-ice coverage is largest, the variation in high-latitude cloud albedo over the ocean is only 0.013 for obliquity and precession.

Although smaller than obliquity, precession does have an effect on annual-mean high-latitude ocean-absorbed insolation and sea-ice coverage, despite no annual-mean insolation forcing, due to changes in the timing of seasonal insolation and interactions with sea-ice coverage. Because sea-ice coverage is smallest in the summer, when summer insolation is relatively high the lower albedo of the open-ocean allows it to absorb more of the surface incident insolation, leading to an increase in the amount of annual-mean ocean-absorbed insolation even if there is no change in annual-mean insolation forcing. The summer insolation amplitude changes from obliquity also have some effect on the amount of annual-mean ocean-absorbed insolation, but it is smaller than precession, and smaller still than the effect of annual-mean insolation forcing from obliquity on ocean-absorbed insolation, so is of secondary importance in the transient obliquity experiments.

In combination, the effects of surface incident insolation and sea-ice feedbacks produce an annual-mean high-latitude ocean absorbed insolation amplitude of ~12 Wm^{-2} from obliquity forcing but only ~6 Wm^{-2} from precession forcing (Figure 2.1). The ocean acts as a seasonal energy integrator, which allows it to store and reemit the absorbed insolation as heat throughout the year. During times of maximum (minimum) high-latitude summer insolation, the high-latitude ocean absorbs and releases to the atmosphere a larger (smaller) amount of heat for obliquity than precession. The difference in high-latitude ocean-atmosphere heat flux is plotted in Figure 2.1. The greater heat flux response to obliquity relative to precession adds to the direct insolation heating, increasing the seasonal climate sensitivity to the insolation forcing.

The larger influences of obliquity compared to precession on ocean-atmosphere heat flux and sea-ice have been found in other modeling studies (e.g. Gallimore and Kutzbach, 1995). Additionally, Eemian sea surface temperature estimates from planktonic foraminifera along a North Atlantic meridional transect correlate well with local changes in mean annual insolation (Cortijo et al., 1999).

Changes in obliquity also produce greater North American high-latitude vegetation responses, mainly between tundra and boreal forest, than precession (Figure 2.1). In BIOME4, annual net-primary-productivity (NPP) and number of growing degree-days (GDD) above 0 °C determine the threshold between tundra and boreal forest (Kaplan et al., 2003). Due to annual-mean insolation changes, obliquity produces a larger range of annual temperature and sunlight reaching the surface and accordingly, a larger amount of tundra/boreal forest exchange. While the precession cycle causes large average insolation changes on seasonal timescales, its insolation forcing sums to zero on an annual basis, which reduces the annual-mean changes in surface incident insolation and temperature. As a result, NPP and GDD variations favor obliquity with 22.7% more land area transitions from tundra to boreal forest in the high-latitudes of North America during periods of peak summer insolation from obliquity forcing than precession forcing. The greater boreal forest coverage decreases annual-mean high-latitude North American surface albedo by an additional 0.040 (27.6%) for obliquity compared to precession; the differences are especially large in the winter and spring months (over 0.077 in March) when the tree canopy masks the snow cover.

The lower albedo and greater moisture content of boreal forest compared to tundra causes more near-surface warming year-round. Additionally, like sea-ice changes, the boreal forest/tundra exchange influences the timing of spring warming and fall cooling and amplifies seasonal temperature differences of the orbital extremes. In turn, the timing of snowmelt varies, further modifying surface albedo and temperature responses.

While proxy studies show a correlation between vegetation and orbit (e.g. Gonzalez-Samperiz et al., 2010), we are not aware of any records directly documenting cycles of orbitally-driven Arctic taiga-tundra feedback. This feedback has, however, been recognized in modeling studies that looked at snapshots outputs from several orbital configurations (Gallimore and Kutzbach, 1996; Koenig et al., 2011) as well as transient experiments with models of intermediate complexity (Crucifix and Loutre, 2002; Claussen et al., 2006). For instance, Crucifix and Loutre (2002) observe a large high-latitude vegetation (and sea-ice) response to changes in insolation when modeling the transition out of the last interglacial period. In contrast to our results, precession was found to control most of their vegetation feedback. Differences in vegetation transition thresholds and the strength of the insolation forcing might be in part to blame for this discrepancy. Moreover, Horton et al. (2010) found the taiga-tundra feedback was essential for producing orbitally-driven ice-sheet retreat in simulations of Late Paleozoic glacial cycles.

The cycles of obliquity and precession both affect seasonal temperatures. However, annual-insolation-enhanced positive feedbacks of ocean heat flux, sea-ice coverage, and vegetation type work synergistically to amplify the temperature sensitivity to changes in the obliquity compared to precession. For all months, obliquity-forced changes in high-latitude insolation produce a larger temperature response than precession (see Appendix Figure 2.1). Arguably the most important temperature sensitivity to insolation forcing for ice-sheet response is during the summer months. The regression in mean high-latitude North American June, July, August (JJA) surface temperature with MJJ insolation is 1.73 times steeper for obliquity than precession (Figure 2.1), resulting in a similar range of summer temperatures despite a large difference in summer insolation amplitude. Even though summer insolation is the dominant factor for determining perennial snow cover through seasonal melting in the high-latitudes of North America, annual-mean insolation intensifies the climate response to changes in obliquity.

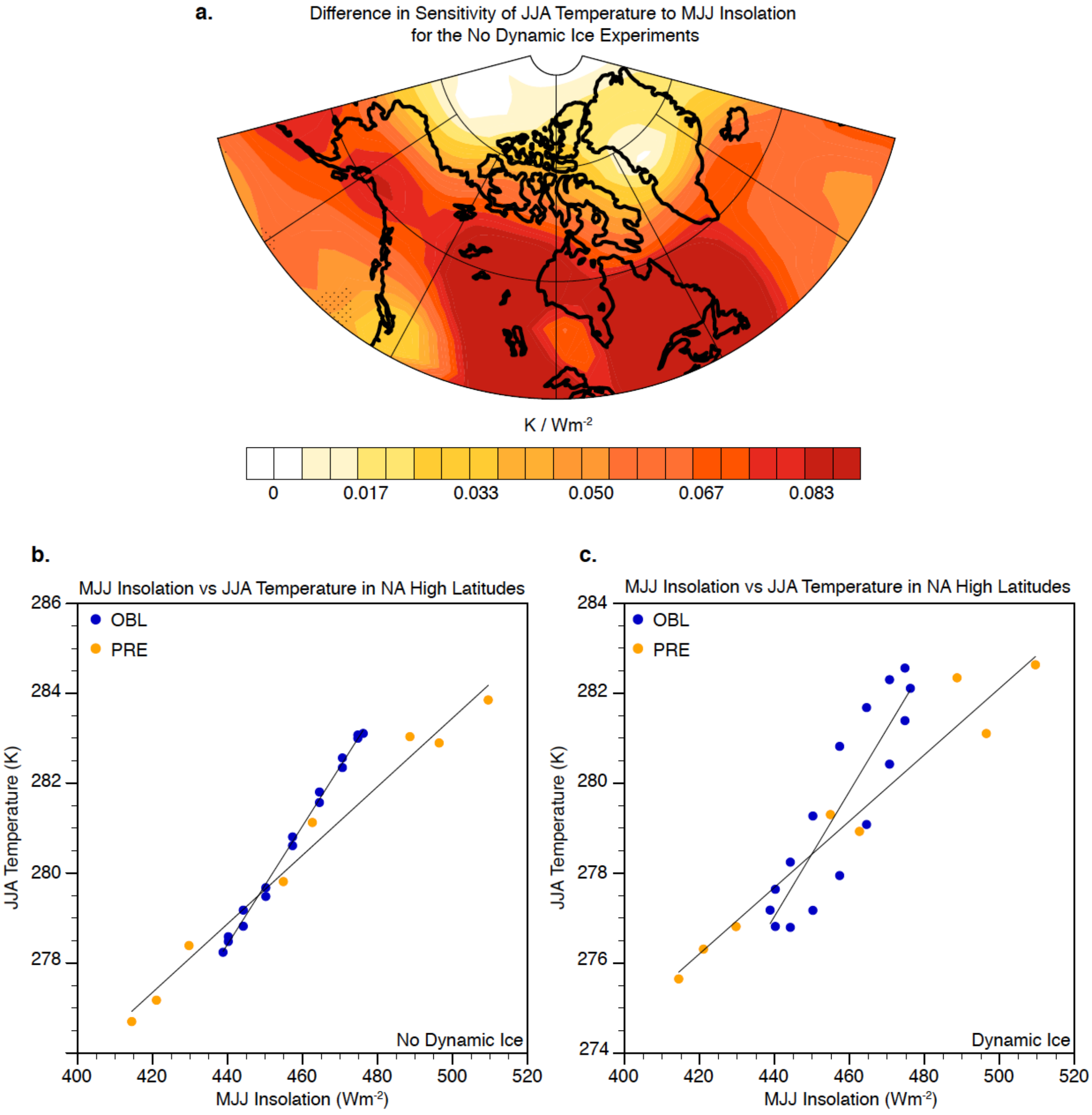

Figure 2.2: High-latitude temperature sensitivity to obliquity and precession
a) The regression slope of MJJ insolation against JJA temperature (K/Wm^{-2}) for obliquity minus precession over northern North America for the climate-only experiments. Stippling represents areas where linear regressions are not significant at the 95% confidence level. b) JJA temperature response to MJJ insolation forcing from obliquity and precession averaged over North America between 60-75°N for climate-only experiments. c) JJA temperature response to MJJ insolation forcing from obliquity and precession averaged over North America between 60-75°N for

climate-ice sheet experiments. In b) and c), each dot represents the AGCM averaged equilibrium output for a given orbital configuration. Here we choose a 1-month delay for the temperature response to incoming insolation because it has the best linear relationship. Using a 2-month delay produces a similar insolation/temperature relationship with obliquity still having much greater temperature sensitivity than precession.

Studies have proposed that the greater latitudinal summer insolation gradient caused by the obliquity cycle enhances eddy fluxes, which leads to greater Arctic snowfall variability (e.g. Jackson and Broccoli, 2003; Lee and Poulsen, 2008). While the mid-latitudes eddy fluxes vary as a result of changes in insolation gradient, we find little difference in the NH high-latitude eddy heat and moisture flux between obliquity and precession (see Appendix Figure 2.2). The small differences in transport that do exist do not reflect the high-latitude temperature sensitivity responses. Therefore, we do not believe transport significantly influences the climate sensitivity differences to orbital forcing we discuss here. Instead, local changes appear to control most of the climate response. Furthermore, moisture flux appears to be of secondary importance, as ablation, not snowfall, dictates the majority of the ice volume response in our model.

2.4.2 Climate-ice sheet experiments

We ran the same transient orbital configurations of obliquity and precession with the inclusion of an asynchronously coupled thermo-mechanical ice-sheet model. Results show that while high-latitude summer insolation is the main mechanism controlling ice-sheet volume, the ice-sheet rate of change to variations in obliquity and precession are similar (Figure 2.3), despite summer insolation changes due to precession being much larger. This is due to ocean heat flux, sea-ice, and vegetation feedbacks that enhance the temperature response to insolation forcing from obliquity (Figure 2.1; Figure 2.2). The enhanced temperature range promotes ice growth and retreat. The similar growth and decay rate, combined with the longer cycle duration for obliquity (40 versus 20 kyr), results in a total ice-volume amplitude that is 42% larger for obliquity than precession (Figure 2.3).

To evaluate the influence of the different durations of obliquity and precession cycles on ice volume, we ran an additional experiment with a transient obliquity cycle scaled to 20 kyr. The percent difference in ice-volume range through a precession cycle is larger by only 22.5% (Figure 2.4) even though the high-latitude summer insolation range is larger for precession by 87%. The similar ice volume rate of change and ranges in Figure 2.4 demonstrate that the annual-mean insolation forcing of obliquity and resulting surface feedbacks are strong enough to cancel the nearly 2 times greater MJJ summer insolation forcing of precession. Additionally, the standardized duration experiment shows that the potential lesser damping of the 40 kyr obliquity forcing due to ice-sheet mass inertia and isostasy (vs. 20 kyr for precession) would be insufficient on their own to yield the greater obliquity response in Figure 2.3. Without considering the surface feedbacks to the annual-mean insolation forcing from obliquity, traditional Milankovitch theory is unable to explain the relative amplitudes of ice sheet response in our model results.

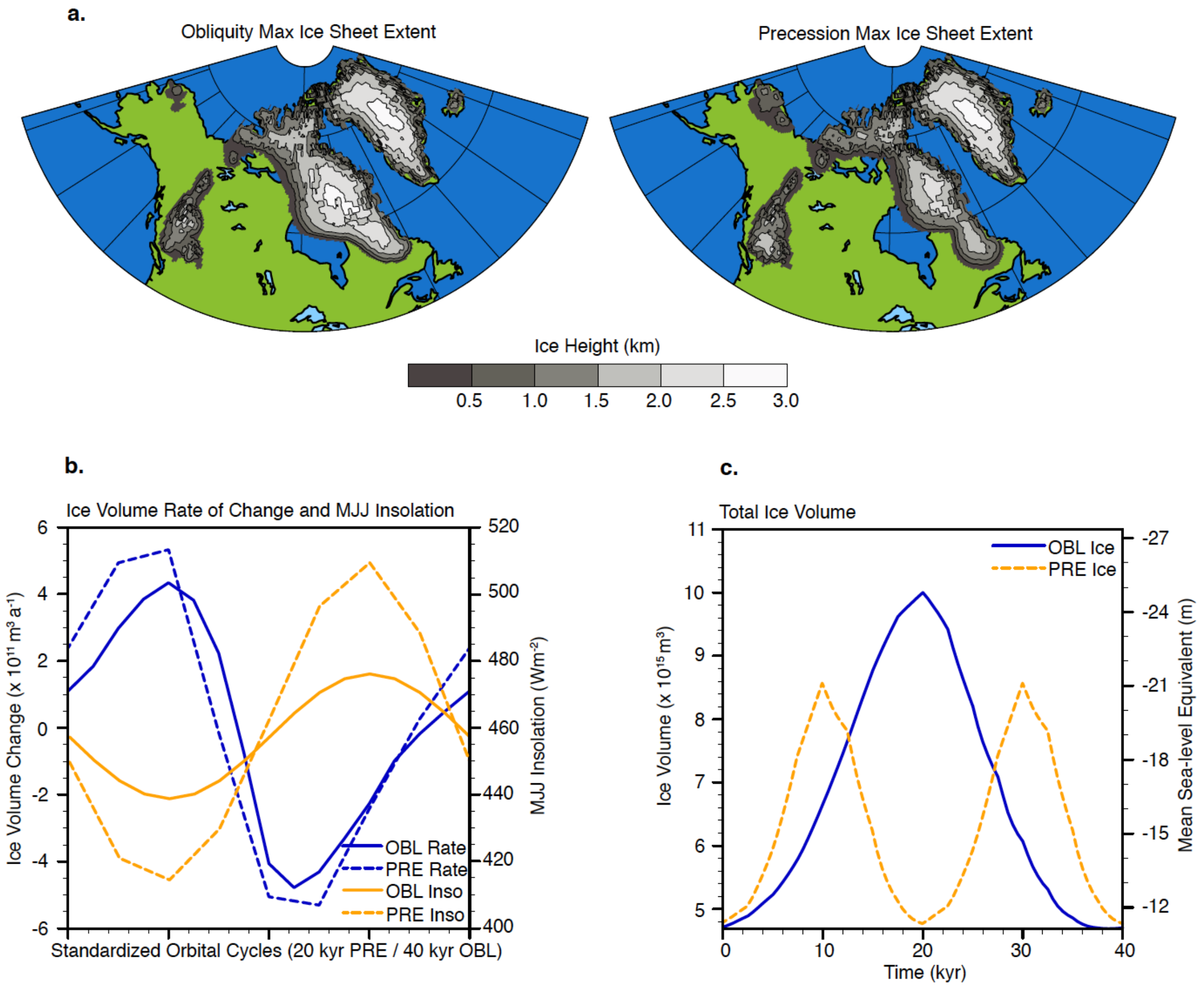

Figure 2.3: Ice volume responses to obliquity and precession
a) Maximum ice-sheet extents simulated over the 40 kyr obliquity and 20 kyr precession cycles. b) Ice-volume rate of change (ma^{-1}) and MJJ insolation forcing between 60-75°N (Wm^{-2}) through a 40 kyr cycle of obliquity and a 20 kyr cycle of precession. Cycle lengths were standardized and aligned by peak summer insolation for comparison. c) Total North American ice-volume (m^3)

from obliquity and precession orbital forcing over a 40 kyr period. Mean sea-level equivalent values (m^2) relative to modern-day are also provided.

In all climate-ice experiments, the ice volume cycles of growth and retreat are fairly symmetric. We note that the $\delta^{18}O$ signal of the Early Pleistocene is also fairly symmetric; only after the mid-Pleistocene transition with the appearance of the 100 kyr cycle does asymmetry become significant. The near-symmetry of the modeled ice volume cycles is likely in part a response to the idealized nature of our experiments that include a large, fixed value of eccentricity and no greenhouse gas fluctuations. We do not expect the ice volume responses would maintain the same amount of symmetry if these additional factors were included in the model.

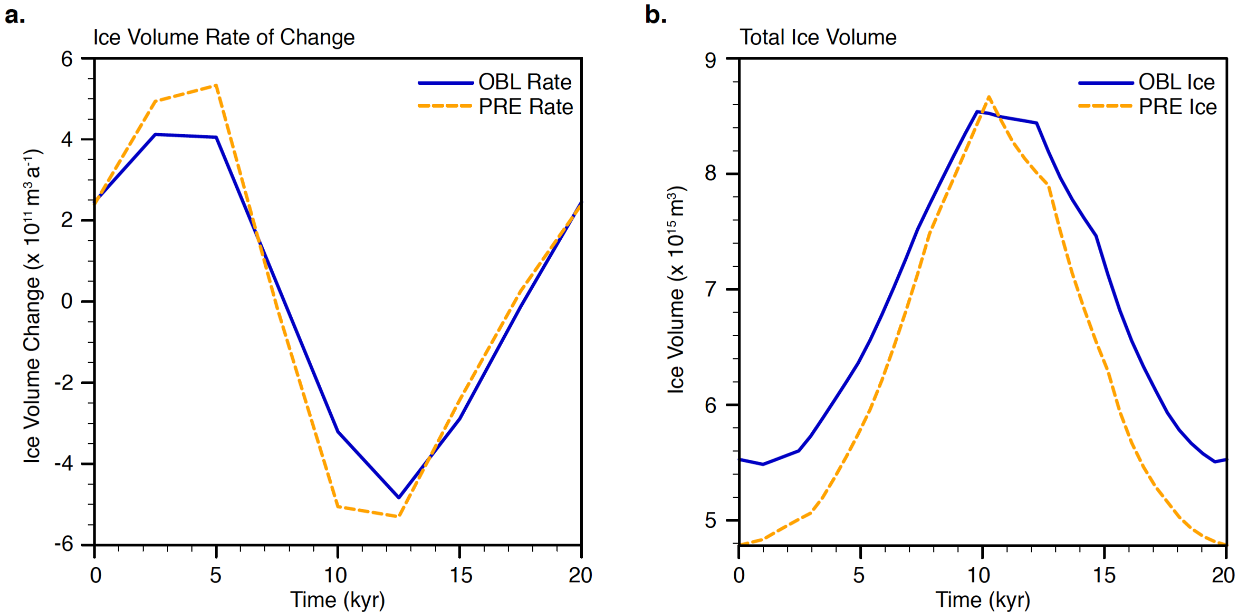

Figure 2.4: Ice volume responses to standardized orbital forcing
a) The ice-volume rate of change (ma^{-1}) and b) total North American ice volume (m^3) for a 20 kyr cycle of obliquity and a 20 kyr cycle of precession.

2.5 Discussion and conclusion

The results of this study show that positive surface feedbacks enhance the ice-volume response to the cycles of obliquity relative to precession. Our choice of orbital configurations further highlights the influence of obliquity on the climate system. Insolation forcing from precession changes significantly between cycles due to power modulation by eccentricity. Here we use the largest eccentricity value of the Pleistocene, producing the maximum precession summer insolation amplitude. A precession cycle with similar summer insolation amplitude to these experiments occurs at most once every 100 kyr. Like the precession cycle, the obliquity cycle in these experiments represents the maximum range of the Pleistocene; however, the extreme orbital amplitude of obliquity is a smaller deviation from the average (47% difference) than the extreme orbital amplitude of eccentricity/precession (66% difference).

In this study, we do not examine the ice-volume response to combined changes in precession, obliquity, and eccentricity. Nevertheless, assuming similar climate feedbacks to our current results, we would expect to find a strong obliquity signal when applying combined orbital forcing as well. The obliquity signal should appear continuously while the precession cycle will only have a significant influence on ice-volume when eccentricity is large (every ~100 kyr), reducing the signal frequency. Combined with the potential for melting offset by Antarctica from precession forcing (Raymo et al., 2006; Lee and Poulsen, 2009), the obliquity dominated $\delta^{18}O$ record of the Early Pleistocene might not be difficult to replicate. However, without invoking a hemispheric offset we expect our current model configuration will produce a smaller, yet significant, precession ice volume signal, which is not found in the Early Pleistocene ice volume proxy records (Lisiecki and Raymo, 2007). Future work will examine the combined interactions between obliquity and precession to help quantify the synergistic interactions.

Our model experiments reveal feedbacks that help explain the Early Pleistocene $\delta^{18}O$ record; yet, the 100 kyr ice volume cycle of the Late Pleistocene remains an enigma. It is possible that the amplifying feedbacks associated with annual insolation are lost when considering the much larger ice-sheets of the Late Pleistocene. Simply covering a much greater area of the Arctic with ice could reduce the vegetation feedbacks. Likewise, the cooling effect of a large ice-sheet might push the permanent sea-ice extent below latitudes with a large annual-mean insolation signal from obliquity. In this case, the combined insolation forcing of precession and obliquity may be required to trigger ice-sheet retreat. Indeed, statistical analysis of $\delta^{18}O$ indicates that both obliquity and precession forcings influence ice-sheet retreat during the Late Pleistocene (Huybers, 2011).

The goal of this study was to investigate climate sensitivity to orbital configuration rather than simulate specific intervals of ice-volume change. However, it is worth noting that the ice sheets in our experiments are fairly small; over obliquity and precession cycles, the mean sea-level equivalent change is 13.5 and 9.5 m (Figure 2.3), significantly less than Early Pleistocene global sea-level change estimates of 60-80 m (Sosdian and Rosenthal, 2009). Much of this volume change is due to variations in the North American ice sheets, and our simulated ice sheets are much smaller than those at glacial maxima, even for the Early Pleistocene (Clark and Pollard, 1998). This discrepancy is likely a combination of factors. First, there is a known warm bias in modern-day GENESIS AGCM climate simulations over Northern Canada (Herrington and Poulsen, 2011). Second, our idealized orbits do not capture the strongly reduced NH summer insolation produced by combinations of obliquity, precession, and eccentricity that lead to past glacial maxima. Thirdly, a lack of GHG fluctuations might contribute to the small ice-volume changes in our model (Abe-Ouchi et al., 2007). We plan to address the significance of more realistic climate variability in a future study. Regardless, we believe our results are robust even if the model under predicts the scales of the changes in ice-volume.

Our findings support Milankovitch theory; of all insolation forcings, high-latitude summer insolation forcing has the strongest correlation with ice volume rate of change ($r = -0.85$ for obliquity and -0.89 for precession) (Figure 2.3). Yet Milankovitch theory alone cannot explain the Early Pleistocene $\delta^{18}O$ records or our model results. Surface feedbacks remedy these incongruities. The changes in high-latitude annual-mean insolation resulting from a transient obliquity orbit leads to significant modification in high-latitude ocean heat flux, sea-ice cover, and vegetation type, which work in concert to amplify the annual and seasonal climate sensitivity to changes in insolation. This causes the summer climate sensitivity to changes in insolation from obliquity to become magnified, producing a larger ice-sheet response than expected given the much smaller summer insolation amplitude than precession. These results highlight the significance of annual-mean insolation on the climate and help explain the strength of the obliquity signal found in $\delta^{18}O$ proxies, particularly before the mid-Pleistocene transition. We demonstrate the amplification of surface feedbacks by obliquity with and without dynamic ice sheets and in a duration-standardized experiment. Our results offer a new explanation of the mechanisms related to the Early Pleistocene Milankovitch theory paradox and emphasize the importance of using complex models when investigating long-term changes in climate.

2.6 Caveats

The long-run time required for our transient orbital experiments makes use of a dynamic ocean unfeasible. Instead, we apply a 50-m thermodynamic slab ocean that calculates ocean heat transport through linear diffusion based on the local temperature gradient and a latitude-dependent diffusion coefficient (Thompson and Pollard, 1995a). This method of heat transport works well for paleoclimate simulations because a flux correction is not prescribed as in many other slab ocean models. The model also includes a dynamic-thermodynamic sea ice model with six layers. Previous studies show the slab ocean can fairly accurately replicate the modern climate (Thompson and Pollard, 1997) and the GENESIS GCM has been used extensively for paleoclimate simulations (e.g. DeConto and Pollard, 2003; Horton et al. 2007). We expect our model correctly captures the short-term ocean response to orbital changes, but we cannot address the longer-term changes such as those from the thermohaline circulation. Orbital sensitivity experiments using a dynamic ocean have found sea-ice results that are in agreement with the slab ocean response (Tuenter et al. 2004). Furthermore, dynamic ocean studies suggest that the fast acting sea-ice response controls the changes in the thermohaline circulation (e.g. Tuenter et al. 2004; Poulsen and Zhou, 2013). Nevertheless, additional transient orbital studies using a dynamic ocean model are needed to assess the full impact of the ocean on the ice response.

While we demonstrate the significance of surface feedbacks on climate response, we are unable to quantify the relative significance of the ocean, sea-ice, and vegetation feedbacks due to the large computational expense of a complete feedback analysis. To isolate the effects of the differences in vegetation response, we switch the equilibrium vegetation outputs of obliquity and precession for the climate-only experiments, and then rerun the snapshots to new equilibriums. We find that swapping vegetation decreases the temperature sensitivity difference to insolation forcing between obliquity and precession from 1.73 to 1.60 times. More significantly, the maximum high-latitude summer temperature response decreased by 0.35°C to obliquity and increase by 0.85°C to precession. The temperature responses are as expected; lower surface albedo, caused by a transition from tundra to boreal forest, allows great surface warming. Unfortunately, the same technique cannot be used to explore the ocean and sea-ice feedbacks because swapping ocean temperatures and sea-ice coverage compromises the energy balance of the system.

As previously mentioned, other studies find surface feedbacks to be important climate response modifiers. For example, Horton et al. (2009) report the vegetation feedback is critical for ice sheet retreat in the Paleozoic. Furthermore, Claussen et al. (2009) observe sea-ice and vegetation to be important for surface temperature with synergy between the feedbacks amplifying both responses. Recently, Erb et al. (2013) use the radiative kernel method to deconstruct the feedback responses in several orbital snapshot experiments. However, their study did not look at the feedbacks associated with vegetation and land-ice. We plan to perform a feedback analysis of "slow" climate responses in the future. Despite these limitations, our study is the first to examine the role of obliquity and precession using transient orbits with a complex Earth system model that includes dynamic land-ice.

2.7 Acknowledgements

We thank the Climate Change Research Lab at the University of Michigan for their discussion and suggestions. We are grateful to Kerim Nisancioglu and two anonymous reviews, Roland Zech, and editor Marie-France Loutre whose comments greatly improved this manuscript. This research was funded by NSF-OCE-0902258.

2.8 Appendix A

There is a greater difference in the moisture flux between obliquity and precession, mainly due to the transient eddy component (Appendix Figure 2.2). Still, the differences are rather minimal, especially compared to the mid-latitude flux. It is possible that that greater moisture flux in response to precession during summer perihelion slows the rate of ice retreat. However, studies, including our own, suggest that ablation is more important than accumulation for determining ice sheet mass balance.

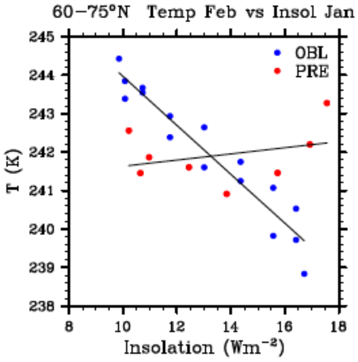
60–75°N Temp Feb vs Insol Jan
OBL
PRE
T (K)
245
244
243
242
241
240
239
238
8
10
12
14
16
18
Insolation (Wm^{-2})

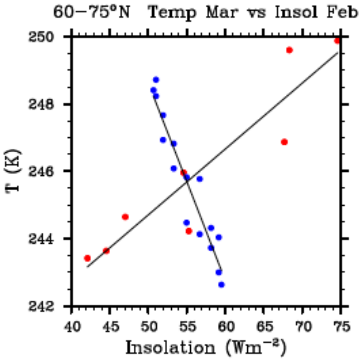
60–75°N Temp Mar vs Insol Feb
T (K)
250
248
246
244
242
40
45
50
55
60
65
70
75
Insolation (Wm^{-2})

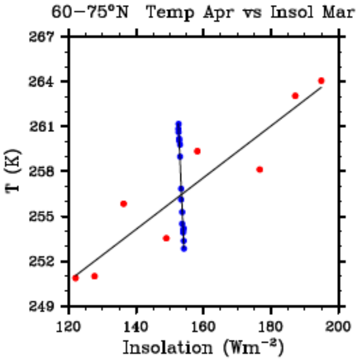
60–75°N Temp Apr vs Insol Mar
T (K)
267
264
261
258
255
252
249
120
140
160
180
200
Insolation (Wm^{-2})

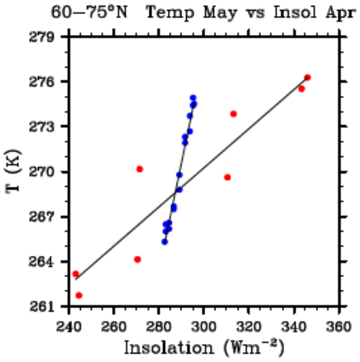
60–75°N Temp May vs Insol Apr
T (K)
279
276
273
270
267
264
261
240
260
280
300
320
340
360
Insolation (Wm^{-2})

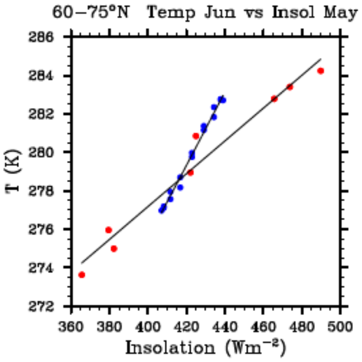
60–75°N Temp Jun vs Insol May
T (K)
286
284
282
280
278
276
274
272
360
380
400
420
440
460
480
500
Insolation (Wm^{-2})

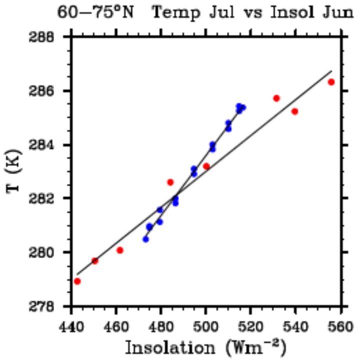
60–75°N Temp Jul vs Insol Jun
T (K)
288
286
284
282
280
278
440
460
480
500
520
540
560
Insolation (Wm^{-2})

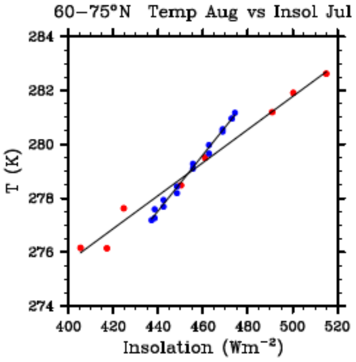
60–75°N Temp Aug vs Insol Jul
T (K)
284
282
280
278
276
274
400
420
440
460
480
500
520
Insolation (Wm^{-2})

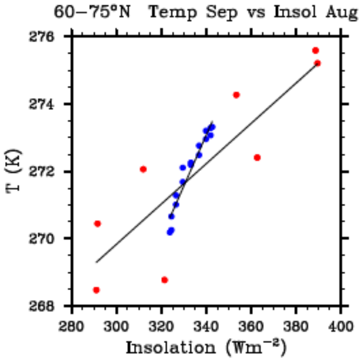
60–75°N Temp Sep vs Insol Aug
T (K)
276
274
272
270
268
280
300
320
340
360
380
400
Insolation (Wm^{-2})

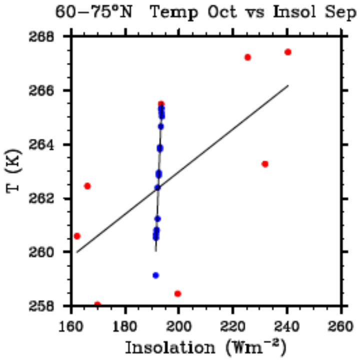
60–75°N Temp Oct vs Insol Sep
T (K)
268
266
264
262
260
258
160
180
200
220
240
260
Insolation (Wm^{-2})

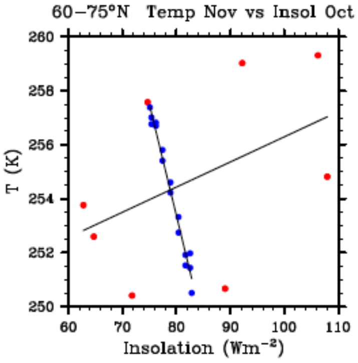
60–75°N Temp Nov vs Insol Oct
T (K)
260
258
256
254
252
250
60
70
80
90
100
110
Insolation (Wm^{-2})

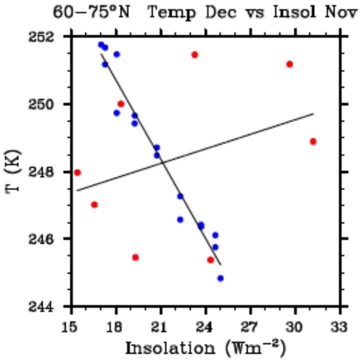
60–75°N Temp Dec vs Insol Nov
T (K)
252
250
248
246
244
15
18
21
24
27
30
33
Insolation (Wm^{-2})

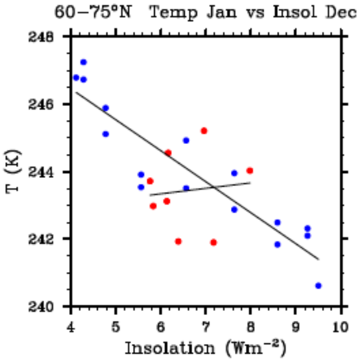
60–75°N Temp Jan vs Insol Dec
T (K)
248
246
244
242
240
4
5
6
7
8
9
10
Insolation (Wm^{-2})

Appendix Figure 2.1: Temperature / insolation relationships
The correlation between monthly temperature and monthly insolation with a 1-month lag for the temperature response. The negative correlation between obliquity insolation forcing and temperature in the winter months is due to the overpowering annual insolation signal. Also, the large temperature range in the spring and fall without a large change in insolation is due to ocean and vegetation feedbacks.

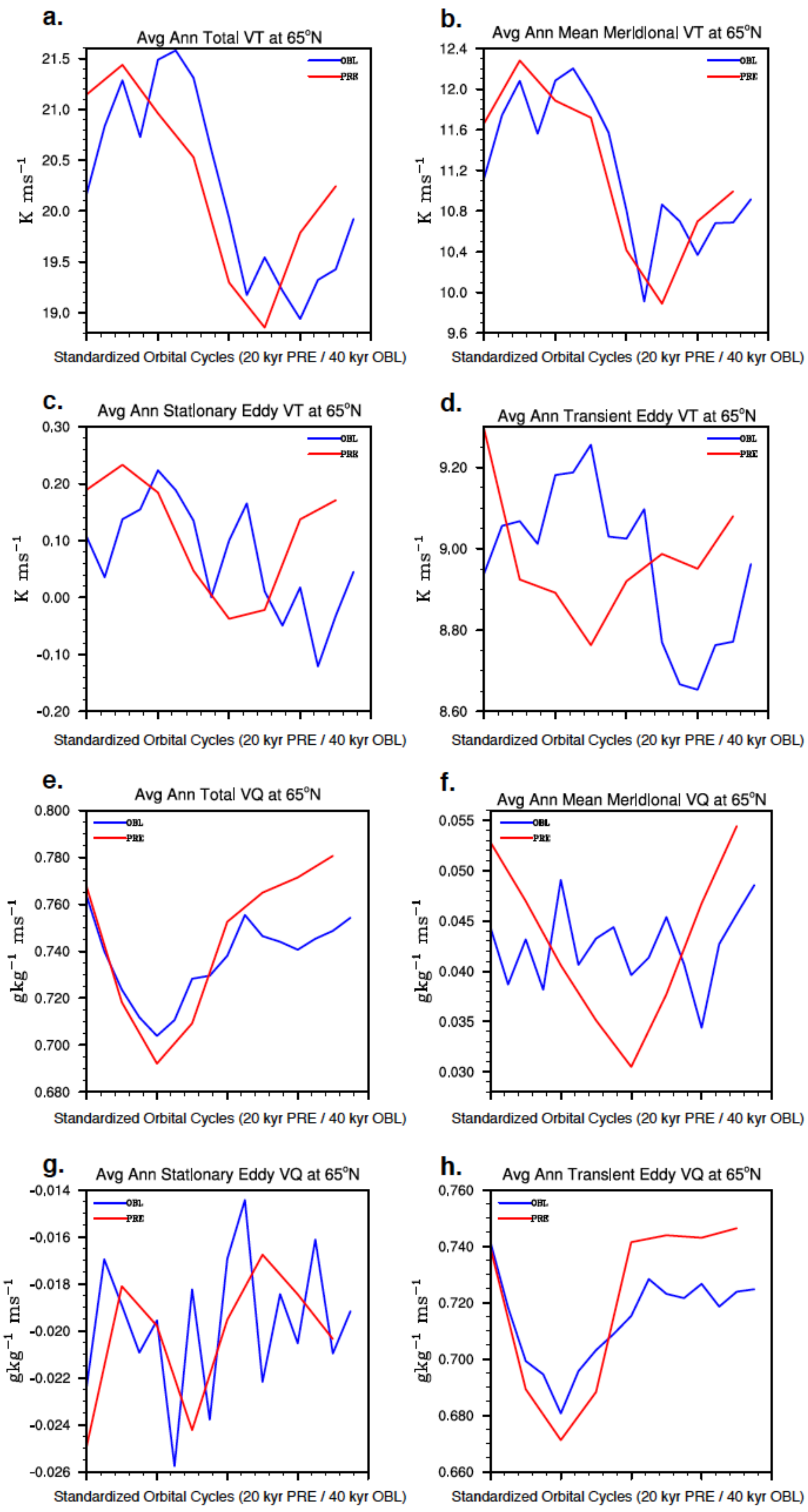
a.
Avg Ann Total VT at 65°N
b.
Avg Ann Mean Meridional VT at 65°N
c.
Avg Ann Stationary Eddy VT at 65°N
d.
Avg Ann Transient Eddy VT at 65°N
e.
Avg Ann Total VQ at 65°N
f.
Avg Ann Mean Meridional VQ at 65°N
g.
Avg Ann Stationary Eddy VQ at 65°N
h.
Avg Ann Transient Eddy VQ at 65°N
OBL
PRE
K ms^{-1}
gkg^{-1} ms^{-1}
Standardized Orbital Cycles (20 kyr PRE / 40 kyr OBL)
21.5
21.0
20.5
20.0
19.5
19.0
12.4
12.0
11.6
11.2
10.8
10.4
10.0
9.6
0.30
0.20
0.10
0.00
-0.10
-0.20
9.20
9.00
8.80
8.60
0.800
0.780
0.760
0.740
0.720
0.700
0.680
0.055
0.050
0.045
0.040
0.035
0.030
-0.014
-0.016
-0.018
-0.020
-0.022
-0.024
-0.026
0.760
0.740
0.720
0.700
0.680
0.660

Appendix Figure 2.2: Heat transport through time
The global annual-average northward heat (VT) and moisture (VQ) flux across 65°N separated into mean-meridional, stationary eddy, and transient eddy components. The total heat flux (S2a) response is almost identical for obliquity and precession. While there are some differences in the transient eddy heat flux (S2d), the variations are small and completely masked by the other heat flux transport terms.

Bibliography

Abe-Ouchi, A., Segawa, T., and Saito, F.: Climatic Conditions for modelling the Northern Hemisphere ice sheets throughout the ice age cycle, Clim. Past, 3, 423–438, doi:10.5194/cp-3- 423-2007, 2007.

Bender, M. L.: Orbital tuning chronology for the Vostok climate record supported by trapped gas composition, Earth Planet. Sc. Lett., 204, 275–289, doi:10.1016/S0012-821X(02)00980-9, 2002.

Berger, A. and Loutre, M. F.: Insolation values for the climate of the last 10 million years, Quaternary Sci. Rev., 10, 297–317, doi:10.1016/0277-3791(91)90033-Q, 1991.

Birchfield, G.E., Weertman, J. and Lunde, A.T.: A paleoclimate model of northern hemispheric ice sheets, Quaternary Research, 15, 126-42, doi: http://dx.doi.org/10.1016/0033-5894(81)90100-9 1981.

Clark, P. U. and Pollard, D.: Origin of the middle Pleistocene transition by ice sheet erosion of regolith, Paleoceanography, 13, 1–9, doi:10.1029/97PA02660, 1998.

Claussen, M.: Late Quaternary vegetation–climate feedbacks, Clim. Past, 5, 203-216, doi:10.5194/cp-5-203-2009, 2009.

Claussen, M., Fohlmeister, J., Ganopolski, A., and Brovkin, V.: Vegetation dynamics amplifies precessional forcing, Geophys. Res. Lett., 33, L09709, doi:10.1029/2006GL026111, 2006.

Cortijo, E., Lehman, S., Keigwin, L., Chapman, M., Paillard, D., and Labeyrie, L.: Changes in meridional temperature and salinity gradients in the North Atlantic Ocean (30–72N) during the last interglacial period, Paleoceanography, 14, 23–33, doi:10.1029/1998PA900004, 1999.

Crucifix, M. and Loutre, M. F.: Transient simulations over the last interglacial period (126-115 kyr BP): feedback and forcing analysis, Clim. Dyn., 19, 419-433, doi: 10.1007/s00382-002-0234-z, 2002.

DeConto, R. M. and Pollard, D.: A coupled climate-ice sheet modeling approach to the Early Cenozoic history of the Antarctic ice sheet, Palaeogeogr. Paleoclim. Palaeocl., 198, 39–52, doi:10.1016/S0031-0182(03)00393-6, 2003.

Erb, M. P., Broccoli, A. J. and Clement, A. C.: The contribution of radiative feedbacks to orbitally-driven climate change, J. Climate, 26, 5897–5914, doi: http://dx.doi.org/10.1175/JCLI-D-12-00419.1, 2013.

Gallimore, R. G. and Kutzbach, J. E.: Snow cover and sea ice sensitivity to generic changes in Earth orbital parameters, J. Geophys. Res., 100, 1103–1120, doi:10.1029/94JD02686, 1995.

Gallimore, R. G. and Kutzbach, J. E.: Role of orbitally induced changes in tundra area in the onset of glaciation, Nature, 381, 503–505, doi:10.1038/381503a0, 1996.

González-Sampériz, P., Leroy, S. A., Carrión, J. S., Fernández, S., García-Antón, M., Gil-García, M. J., Uzquiano, P., Valero-Garcés, B. and Figueiral, I.: Steppes, savannahs, forests and phytodiversity reservoirs during the Pleistocene in the Iberian Peninsula, Rev. Palaeobot. Palyno., 162, 427–457, doi:10.1016/j.revpalbo.2010.03.009, 2010.

Hays, J. D., Imbrie, J., and Shackleton, N. J.: Variations in the Earth's orbit: pacemaker of the ice age, Science, 194, 1121–1132, doi:10.1126/science.194.4270.1121, 1976.

Herrington, A. R. and Poulsen, C. J.: Terminating the last Interglacial: the role of ice sheet-climate feedbacks in a GCM asynchronously coupled to an ice sheet model, J. Climate, 25, 1871–1882, doi:10.1175/JCLI-D-11-00218.1, 2011.

Horton, D. E. and Poulsen, C. J.: Orbital and CO2 forcing of late Paleozoic continental ice sheets, Geophys. Res. Lett., 34, L19708, doi:10.1029/2007GL031188, 2007.

Horton, D. E. and Poulsen, C. J.: Paradox of late Paleozoic glacioeustasy, Geology, 37, 715–718, doi:10.1130/G30016A.1, 2009.

Horton, D. E., Poulsen, C. J., and Pollard, D.: Influence of high-latitude vegetation feedbacks on late Palaeozoic glacial cycles, Nat. Geosci., 3, 572–577, doi:10.1038/ngeo922, 2010.

Huybers, P.: Early Pleistocene Glacial cycles and the integrated summer insolation forcing, Science, 313, 508–511, doi:10.1126/science.1125249, 2006.

Huybers, P.: Combined obliquity and precession pacing of late Pleistocene deglaciations, Nature, 480, 229–232, doi:10.1038/nature10626, 2011.

Jackson, C. S. and Broccoli, A. J.: Orbital forcing of Arctic climate: mechanisms of cli- mate response and implications for continental glaciation, Clim. Dynam., 21, 539–557, doi:10.1007/s00382-003-0351-3, 2003.

Kaplan, J. O., Bigelow, N. H., Prentice, I. C., Harrison, S. P., Bartlein, P. J., Christensen, T. R., Cramer, W., Matveyeva, N. V., McGuire, A. D., Murray, D. F., Razzhivin, V. Y., Smith, B., Walker, D. A., Anderson, P. M., Andreev, A. A., Brubaker, L. B., Edwards, M. E., and Lozhkin, A. V.: Climate change and Arctic ecosystems: 2. modeling, paleodata-model comparisons, and future projections, J. Geophys. Res., 108, 8171–8188, doi:10.1029/2002JD002559, 2003.

Koenig, S. J., DeConto, R. M., and Pollard, D.: Late Pliocene to Pleistocene sensitivity of the Greenland Ice Sheet in response to external forcing and internal feedbacks, Clim. Dynam., 37, 1247–1268, doi:10.1007/s00382-011-1050-0, 2011.

Lee, S.-Y. and Poulsen, C. J.: Amplification of obliquity forcing through mean annual and seasonal atmospheric feedbacks, Clim. Past, 4, 205–213, doi:10.5194/cp-4-205-2008, 2008.

Lee, S. Y. and Poulsen, C. J.: Obliquity and precessional forcing of continental snow fall and melt: implications for orbital forcing of Pleistocene ice ages, Quaternary Sci. Rev., 28, 2663–2674, doi:10.1016/j.quascirev.2009.06.002, 2009.

Lisiecki, L. E. and Raymo, M. E.: A Pliocene-Pleistocene stack of 57 globally distributed benthic δ18O records, Paleoceanography, 20, PA1003, doi: 10.1029/2004PA001071, 2005.

Lisiecki, L. E. and Raymo, M. E.: Plio–Pleistocene climate evolution: trends and transitions in glacial cycle dynamics, 26, 56-69, Quaternary Sci. Rev., doi:http://dx.doi.org/10.1016/j.quascirev.2006.09.005, 2007.

Marshall, S. J. and Clarke, G. K. C.: Modeling North American freshwater runoð through the Last Glacial Cycle, Quaternary Res., 52, 300–315, doi:10.1006/qres.1999.2079, 1999.

Petit, J. R., Jouzel, J., Raynaud, D., Barkov, N. I., Barnola, J. M., Basile, I., Bender, M., Chappellaz, J., Davis, M., and Delaygue, G.: Climate and atmospheric history of the past 420000 yr from the Vostok ice core, Antarctica, Nature, 399, 429–436, doi:10.1038/20859, 1999.

Pollard, D. and DeConto, R. M.: Modelling West Antarctic ice sheet growth and collapse through the past five million years, Nature, 458, 329–332, doi:10.1038/nature07809, 2009.

Pollard, D. and DeConto, R. M.: Description of a hybrid ice sheet-shelf model, and application to Antarctica, Geosci. Model Dev., 5, 1273–1295, doi:10.5194/gmd-5-1273-2012, 2012.

Pollard, D. and Reusch, D. B.: A calendar conversion method for monthly mean paleoclimate model output with orbital forcing, J. Geophys. Res., 107, 4615–4622, doi:10.1029/2002JD002126, 2002.

Poulsen, C. J. and Zhou, J.: Sensitivity of Arctic Climate Variability to Mean State: Insights from the Cretaceous, J. Climate, 26, 7003-7022, doi: http://dx.doi.org/10.1175/JCLI-D-12-00825.1, 2013.

Raymo, M. E. and Nisancioglu, K.: The 41kyr world: Milankovitch's other unsolved mystery, Paleoceanography, 18, 1011–1017, doi:10.1029/2002PA000791, 2003.

Raymo, M. E., Lisiecki, L. E., and Nisancioglu, K. H.: Plio-Pleistocene ice volume, Antarctic climate, and the global à18O record, Science, 313, 492–495, doi:10.1126/science.1123296, 2006.

Robinson, A., Calov, R., and Ganopolski, A.: An eðcient regional energy-moisture balance model for simulation of the Greenland Ice Sheet response to climate change, The Cryosphere, 4, 129–144, doi:10.5194/tc-4-129-2010, 2010.

Ruddiman, W. F.: Orbital changes and climate, Quaternary Sci. Rev., 25, 3092–3112, doi:http://dx.doi.org/10.1016/j.quascirev.2006.09.001, 2006.

Sosdian, S. and Rosenthal, Y.: Deep-sea temperature and ice volume changes across the Pliocene-Pleistocene climate transitions, Science, 325, 306–310, doi:10.1126/science.1169938, 2009.

Thompson, S. L. and Pollard, D.: A global climate model (GENESIS) with a land-surface transfer scheme (LSX). part I: present climate simulation, J. Climate, 8, 732-761, doi:http://dx.doi.org/10.1175/1520-0442(1995)008<0732:AGCMWA>2.0.CO;2, 1995.

Thompson, S. L. and Pollard, D.: Greenland and Antarctic mass balances for present and doubled atmospheric CO2 from the GENESIS version-2 global climate model, J. Climate, 10, 871–900, doi:10.1175/1520-0442(1997)010à0871:GAAMBF_2.0.CO;2, 1997.

Tuenter, E., Weber, S. L. and Hilgen, F. J.: Sea-ice feedbacks on the climatic response to precession and obliquity forcing, Geophys. Res. Lett., 32, L24704, doi:10.1029/2005GL024122, 2005.

van den Berg, J., van de Wal, R., and Oerlemans, H.: A mass balance model for Eurasian Ice Sheet for the last 120000yr, Global Planet. Change, 61, 194–208, doi:10.1016/j.gloplacha.2007.08.015,2008.gloplacha.2007.08.015, 2008.

Chapter 3: How Obliquity Cycles Powered Early Pleistocene Global Ice-Volume Variability

3.1 Abstract

Milankovitch theory proposes that the magnitude of high-latitude summer insolation dictates the continental ice-volume response by controlling summer snow melt, thus anticipating a substantial ice-volume contribution from the strong summer insolation signal of precession. Yet almost all of the early Pleistocene δ^{18}O records' signal strength resides at the frequency of obliquity. Here we explore this discrepancy using a climate-vegetation-ice sheet model to simulate climate-ice sheet response to transient orbits of varying obliquity and precession. Spectral analysis of our results shows that despite contributing significantly less to the summer insolation signal, almost 60 % of the ice-volume power exists at the frequency of obliquity due to a combination of albedo feedbacks, seasonal offsets, and orbital cycle duration differences. Including eccentricity modulation of the precession ice-volume component and assuming a small Antarctic ice response to orbital forcing produces a signal that agrees with the δ^{18}O ice-volume proxy records.

3.2 Introduction

The most widely held theory for the relationship between ice-volume and insolation comes from the calculations of Milankovitch (1941), who proposed that high-latitude (HL) caloric summer half-year insolation determines the amount of snow cover that can survive summer melt and consequently, the amount of ice-sheet growth or retreat. Changes in both Earth's obliquity and precession contribute significantly to the caloric summer half-year insolation forcing. Therefore, Milankovitch theory predicts that precession should produce a considerable ice-volume signal, a prediction born out by climate models (e.g., Berger et al., 1999). However, the δ^{18}O ice-volume proxy records do not show the same signal. Rather, little spectral power exists at the frequency of precession, with practically none of the signal strength in the early Pleistocene (EP) (2.588-0.781 Ma) (Figure 3.1) (Lisiecki and Raymo, 2007). The surprising dominance of the obliquity signal in opposition to Milankovitch theory has been coined the "41 kyr problem" (Raymo and Nisancioglu, 2003). Multiple hypotheses have been proposed to remedy the discrepancies between traditional Milankovitch theory and the ice-volume proxy record (e.g., Clark and Pollard, 1998; Berger et al., 1999; Philander and Fedorov, 2003; Raymo and Nisancioglu, 2003; Loutre et al., 2004; Ravelo et al., 2004; Vettoretti and Peltier, 2004; Huybers and Wunsch, 2005; Lee and Poulsen, 2005; Huybers, 2006; Raymo et al., 2006; Lee and Poulsen, 2008; Tabor et al., 2014) but the contributions of these hypotheses to the ice-volume record have not been systematically explored with a model that includes both dynamic atmosphere and ice components.

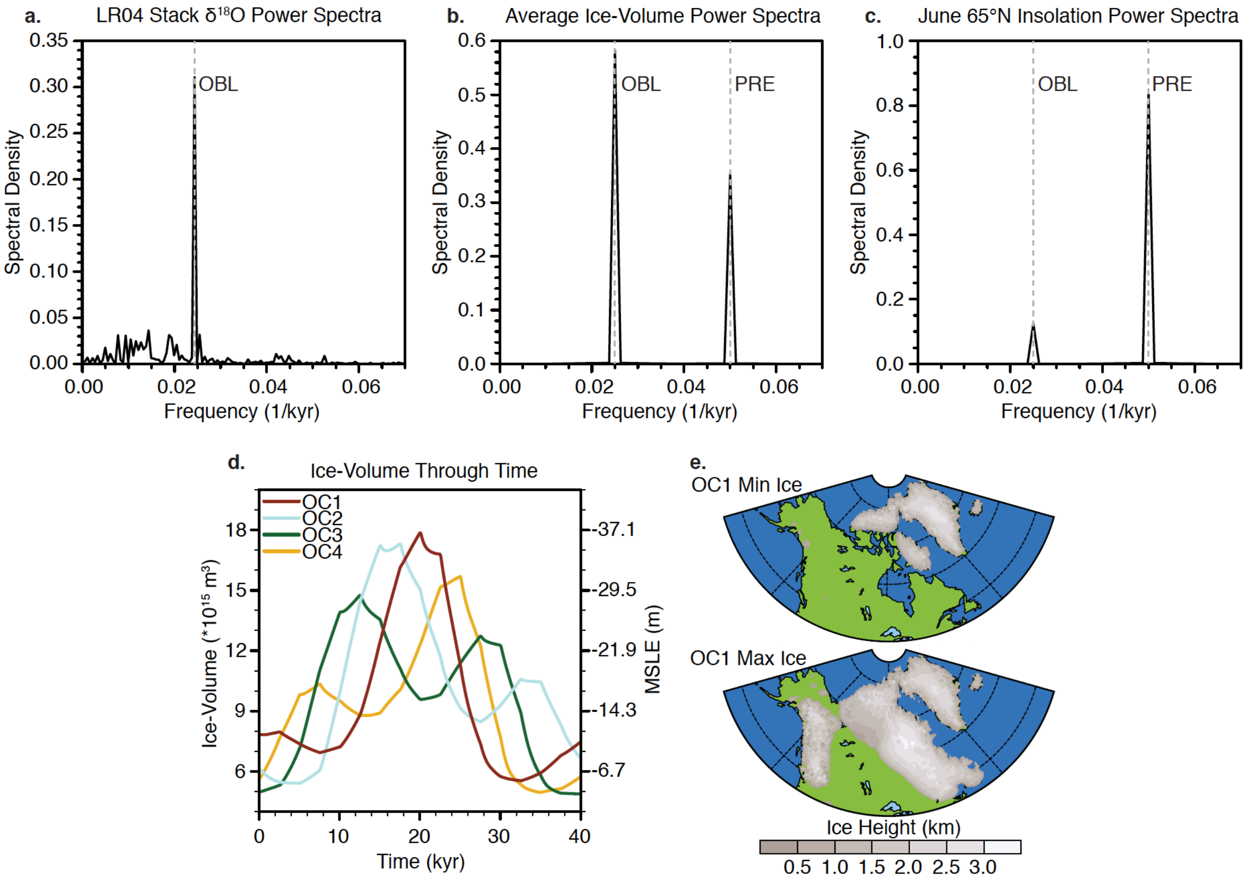

Figure 3.1: The 41 kyr problem and the ice sheet responses to orbital forcing
a) The power spectra of EP (2.588-0.781 Ma) detrended δ^{18}O stack [Lisiecki and Raymo, 2005]. Almost all of the power is at the frequency of obliquity. b) Average standardized spectral power distribution of the ice-volume response to our four transient orbital configurations (OC1-OC4). The ice-volume response produces more power at the frequency of obliquity than precession. c) Plot of the 65°N June insolation spectral power distribution. Here we chose 65°N June insolation because it is a standard commonly associated with modeling studies of Milankovitch theory. Vertical dashed gray lines highlight the location of the obliquity and precession frequencies. d)

Simulated ice-volume (10^{15} m^3) for our four transient orbital configurations (OC1-4). e) The minimum and maximum ice extents for OC1. Ice extents for OC2-OC4 are comparable.

Here we use an Earth system model to investigate the role of orbital forcing on climate. In contrast to previous studies, which model the climate responses to orbital forcing without dynamic land-ice (e.g., Lee and Poulsen, 2008; Mantsis et al., 2011; Erb et al., 2013) or with only individual orbital parameters (e.g., Tabor et al., 2014), our simulations use a series of transient orbital configurations with dynamic land-ice and simultaneously varying obliquity and precession. This model setup allows us to explore the climate interactions produced by combined orbital forcings and use statistical time-series analysis to make direct comparisons between the modeled ice-volume cycles and proxy data. We find that the ice-volume signal is not entirely a direct response to summer insolation. Instead, climate feedbacks involving sea ice, vegetation, and clouds, seasonal offset of the insolation forcing from precession, and greater cycle duration of obliquity enhance the ice-volume response to obliquity relative to precession. Combined, these factors give obliquity about 60% of the ice-volume power. Though substantially muted, our experiments still produce a larger precession ice-volume response than recorded in Pleistocene $\delta^{18}O$ records. In our discussion, we provide methods to resolve the remaining discrepancies between the modeled ice-volume signal and the $\delta^{18}O$ records of the early Pleistocene. We quantitatively show that the ice-volume spectral power shifts to the obliquity cycle frequency when modulating the precession component by eccentricity or including a small amount of ice-volume response from Antarctica. Our findings are an important step towards explaining the ice-volume records of the early Pleistocene.

3.3 Methods

3.3.1 Earth system model

We use a global climate-vegetation-ice model consisting of the GENESIS 3.0 GCM (Alder et al., 2011), the BIOME4 vegetation model (Kaplan et al., 2003), and the Pennsylvania State University (PSU) ice-sheet model (Pollard and DeConto, 2012). The GENESIS 3.0 GCM contains coupled atmosphere (AGCM) and land-surface (LSX) components. The AGCM is run at T31 horizontal resolution (~3.75°) with 18 vertical sigma levels, and the LSX model is run at 2° horizontal resolution with a 50-m slab ocean that calculates ocean heat transport through linear diffusion based on local temperature gradient and a latitude-dependent diffusion coefficient and dynamic sea-ice. GENESIS 3.0 is synchronously coupled with the BIOME4 vegetation model. Ecosystem types are calculated annually from a combination of prescribed soil and atmospheric CO_2, and monthly mean GCM averages of temperature, insolation, and precipitation. The PSU ice-sheet model is a 3D thermomechanical model; here its marine ice capability is suppressed so all dynamics are based on the shallow ice approximation. Further, we use an insolation/temperature melt scheme (ITM) (Pollard, 1980; van den Berg et al., 2008) in place of the commonly employed positive-degree-day (PDD) melt scheme. Robinson et al. (2010) find the ITM scheme produces a heightened ice-sheet sensitivity compared to the PDD scheme, which better represents ice-volume changes over long time scales.

3.3.2 Experiment design

We force the Earth system model with a series of four idealized, transient orbital configurations that represent the extremes of the Pleistocene (Berger and Loutre, 1991) to explore the interactions of obliquity and precession on climate and northern hemisphere (NH) ice-volume. For ease and efficiency, obliquity and precession vary through time as pure (simple, idealized) sinusoids with durations of 40 kyr and 20 kyr respectfully, approximations of the actual durations. The four orbital configurations (OC1-4) differ only in the timing of precession with respect to obliquity. From a fixed obliquity perspective, precession cycles are staggered by 5 kyr (Appendix Table 3.1). All experiments are initialized with modern continental configuration and land surface type including modern Greenland and Antarctica, and no other ice sheets. The dynamic ice-sheet domain includes Greenland and North America above 40°N. Due to computational costs, we use an asynchronous coupling technique to capture the responses of the Earth system to the transient orbits (e.g., Birchfield et al., 1981; Herrington and Poulsen, 2012). We look at the climate response to orbital forcing both with (climate-ice) and without (climate-only) a dynamic ice-sheet. For experiments without dynamic ice, the ice-sheet model is not run, and land surface type and topography are held fixed at modern. Because EP GHG fluctuations are not well known, we use values representing the average of the last 400 kyr (CO_2=230 ppmv, CH_4=520 ppbv, N_2O=250 ppbv) (Petit et al., 1999; Bender, 2002). See supporting material for additional experiment design details.

3.4 Results

3.4.1 Ice-volume spectral power

The ice-volume responses to our four transient orbital configurations produce mean-sea-level equivalent (MSLE) variations between 25 and 31 m (Figure 3.1). Transient orbital forcing causes substantial variations in the areal extent of both the Laurentian and Cordilleran ice-sheets (Figure 3.1). Spectral analysis of the transient ice-volume signals shows that, on average, there is more power at the frequency of obliquity (40 kyr^{-1}) than precession (20 kyr^{-1}) (Figure 3.1). There is some minor variability in the power density distribution between the four transient orbital configurations, but the greatest signal strength is always at the frequency of obliquity (Appendix Figure 3.1). In contrast, most of the spectral power of June 65°N insolation intensity, a commonly used metric for Milankovitch forcing in climate models, is at the frequency of precession (Figure 3.1), which indicates this common Milankovitch metric is not a direct driver of ice-volume in our model. Like other modeling studies, our results also display too great of an ice-volume response to precession, which is absent in the ice-volume proxy records of the EP (Lisiecki and Raymo, 2005; Huybers, 2007) (Figure 3.1). We propose several explanations for this discrepancy below.

3.4.2 Climate signal decomposition

The prominent ice-volume response at the obliquity frequency occurs through climate amplification of the insolation forcing. To better and more easily understand the climate responses to changes in orbital forcing, we decompose the climate responses of the climate-only experiments into contributions from obliquity and precession using a least-squares fitting procedure similar to that of Jackson and Broccoli (2003). The deviation of a given variable through time from its mean, $\mathrm{X(t)}$, is expressed as:

$$\mathrm{X(t)} = \mathrm{A_o}\phi'(\mathrm{t}) + \mathrm{A_p}\cos[\lambda(\mathrm{t}) - \phi_\mathrm{p}] + \mathrm{R(t)}. \text{ (1)}$$

where ϕ' is the deviation of obliquity from its mean, λ is the longitude of perihelion, and R is the residual that accounts for nonlinearity of the system. The fitting procedure finds the amplitude of response to obliquity $\mathrm{A_o}$, the amplitude of response of precession $\mathrm{A_p}$, and the phase angle of precession ϕ_p. Because eccentricity is constant, it is excluded from equation 1.

The following analysis focuses on the North American (NA) HL (area between 55-75°N and 57-165°W) responses of insolation, surface-absorbed shortwave radiation, and near-surface temperature because these variables are used to calculate ablation in the ice-sheet model (equation S1). Precipitation also contributes to the mass balance of the ice-sheets; however, our ice-volume responses are dominated by ablation, not accumulation, a finding mirrored in other studies (e.g., DeConto et al., 2008; Tabor et al., 2014). Furthermore, precipitation responses to orbital changes are less linear than surface-absorbed shortwave radiation and near-surface temperature, which reduces the appropriateness of the least-squares fitting procedure. Conversely, the NA HL surface-absorbed shortwave radiation and near-surface temperature responses to insolation changes are quite linear in the summer months. The decomposed climate responses discussed below are spatially, temporally, and experiment-averaged signal decompositions from all four transient orbital configurations. We find that the climate responses are similar for all orbital configurations and therefore, Figure 3.2 shows the outputs of OC1 for simplicity. Note, we focus on NA for our analysis because it is within the dynamic ice domain; however, similar responses are found throughout the NH HL.

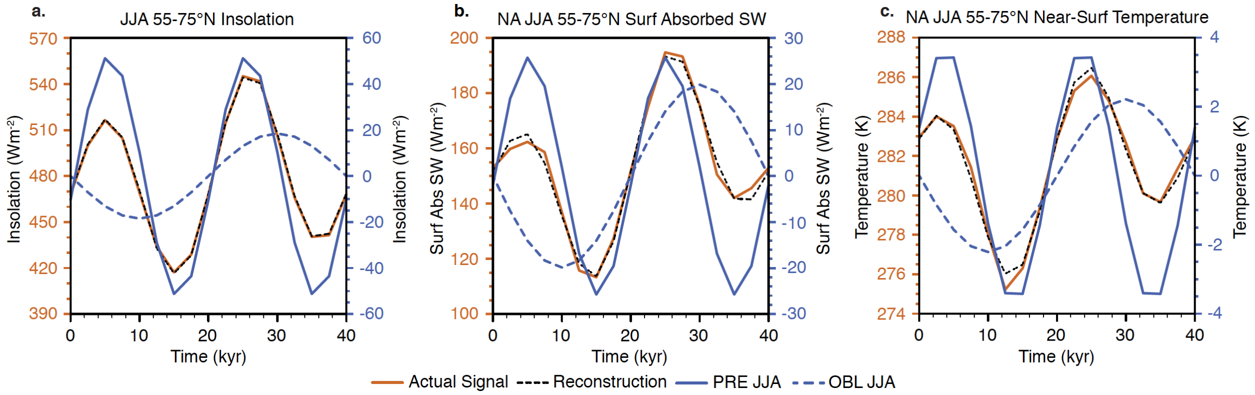

Figure 3.2: Decomposition of high-latitude climate feedbacks to orbital forcing
Spatial and temporal averages of NA HL (55-75°N, 57-165°W) June, July, August (JJA) signals from OC1 over an orbital cycle. The model responses (solid orange line) and least-squares reconstructions (dashed black line) are plotted on the primary y-axis. The contributions from obliquity (dashed blue line) and precession (solid blue line) are plotted on the secondary y-axis. a) The insolation forcing (Wm^{-2}). b) The amount of surface-absorbed shortwave radiation (Wm^{-2}). c) The near-surface temperature (K) response. Obliquity contributes nearly twice as much to the NA HL summer variations in surface-absorbed shortwave radiation and near-surface temperature as it does to insolation forcing, which suggests internal amplification.

3.4.3 Summer season feedbacks

The total HL June, July, August (later referred to as summer) insolation variability is over 124 Wm^{-2} (Figure 3.2). By decomposing the summer insolation forcing into obliquity and precession components, we find that only 11 % of the variance is due to obliquity with the remaining 89 % attributable to precession. On the other hand, the variance of the 78 Wm^{-2} fluctuations in NA HL summer surface-absorbed radiation is split 36 % to 62 %, and the 10°C fluctuations in NA HL summer near-surface temperature are split 24 % and 75 % between obliquity and precession, respectively (Figure 3.2). While precession still controls the majority of the NA HL summer surface-absorbed shortwave radiation and near-surface temperature responses, obliquity contributes nearly twice what would be expected assuming a direct surface response to insolation forcing.

The amplification of the surface responses to insolation forcing is mainly a result of albedo feedbacks that are significantly larger for obliquity than the incoming insolation would suggest. For instance, obliquity forcing accounts for 49 % of the NA HL summer planetary albedo variance. The planetary albedo signal is, in part, a result of variations in surface albedo, which oscillates by 0.14 during the summer months, with a 39 % to 57 % split in the variance between obliquity and precession, respectively. Changes in NH HL sea-ice fractional coverage, split 57 % to 38 % between obliquity and precession, and NA HL tundra/boreal forest exchange, split 38 % to 58 % between obliquity and precession cause much of the summer surface albedo variability. We focus on the summer response because of its significance to ice ablation, but the sea-ice contribution from obliquity is even larger in the spring and fall months. Furthermore, in the model, vegetation distributions do not vary seasonally, enhancing the obliquity response all year. In addition to their direct effects, the surface albedo feedbacks of sea-ice and vegetation also influence the amount of snow cover through melting and canopy masking, which further magnifies the surface albedo response. However, the snow cover fluctuations are less linear than sea-ice and vegetation and therefore, are difficult to decompose through least-squares fitting. These surface albedo feedbacks allow the surface to warm disproportionately relative to the insolation forcing, amplifying the obliquity signal relative to precession.

The obliquity contribution to cloud albedo response is also larger than the insolation forcing with a 47 % to 46 % split in variance between obliquity and precession. The total cloud albedo changes over an orbital cycle are only 0.033 and are mainly a result of changes in stratus clouds. In these experiments cooler HL summer temperatures during periods of low summer insolation allow more snow and soil moisture to persist into the summer months. The surface moisture source, combined with a weak low-level lapse rate due to the cold surface, allows greater low-level relative humidity and stratus cloud cover. In the summer, enhanced cloud cover reduces surface absorbed shortwave radiation and temperature, and provides a positive ice-volume feedback. As previously mentioned, the changes in cloud albedo are fairly small.

The amplified responses of sea-ice fraction and vegetation to obliquity relative to precession are a consequence of the annual-mean insolation changes due to obliquity. Latitudinal redistribution of annual-mean insolation due to changes in obliquity causes variations in ocean-absorbed shortwave to be greater than those due to precession, resulting in more ocean heat release and a larger sea-ice response. Likewise, obliquity forced annual-mean insolation variations in the high latitudes produce a larger range of annual temperature and sunlight reaching the surface than precession, which boosts the range of net-primary productivity and allows for a greater vegetation transition between tundra and boreal forest. Other studies have also found important vegetation and sea-ice responses to orbital variations (e.g., Gallimore and Kutzbach, 1995; 1996; Tuenter et al., 2004; 2005; Claussen et al., 2006; Horton et al., 2010; Tabor et al., 2014); however, this research is the first to examine surface feedbacks under the combined effects of obliquity and precession with a complex Earth system model that includes dynamic land-ice.

3.4.4 Precession seasonal insolation offset

In addition to differences in summer insolation and climate response, obliquity and precession also contribute differently to insolation timing and duration. Even though precession dominates the summer insolation signal, precession produces no changes in annual-mean insolation. Conversely, obliquity does alter the latitudinal distribution of annual-mean insolation, especially in the HLs. The difference in mean-annual insolation between obliquity and precession works to amplify the climate influence of obliquity while dampening the influence of precession (Huybers, 2006). Using the least-squares signal decomposition, we illustrate the difference in insolation forcing from precession and obliquity by examining differences in NH HL insolation forcing between April and September (Appendix Figure 3.2). When April insolation forcing from precession is anomalously large, September insolation forcing from precession is anomalously small, and vice versa. The difference in seasonal phasing of the precession insolation signal causes offset in the NA HL surface-absorbed shortwave (Appendix Figure 3.2) and, to a lesser amount due to inertia of the system, near-surface temperature (Appendix Figure 3.2) while the concurrent seasonal phasing of obliquity amplifies the response. These differences in seasonal forcing shorten the melt season for precession but lengthen it for obliquity.

The amount of ablation that occurs during the spring and fall is small, about 5 % of the total climate-only HL NA land potential ablation (based on equation S1), which makes seasonal offset of secondary importance in our experiments. However, our experimental design uses relatively low GHG concentrations. While not well constrained, the EP was potentially warmer than the mean climate produced by our model configuration. In a warmer world, the melt threshold is more easily reached, allowing a longer melt season that both enhances the seasonal cancellation effect from precession and melt of obliquity (Huybers and Tziperman, 2008). Therefore, our experiments represent a conservative estimate of the seasonal offset response to precession forcing.

3.4.5 Cycle frequencies and nonequilibrium

Even with surface amplification of obliquity signal and seasonal offset of precession forcing, the ablation response favors precession; however, the ice-volume response favors obliquity. Much of this remaining discrepancy is a consequence of the nonequilibrium response of the ice sheets to orbital forcing in combination with differences in cycle duration between obliquity and precession (Roe, 2006; Huybers and Tziperman, 2008). Our results show that ablation has a nearly linear control on ice-volume rate of change while ice-volume lags ablation and has no direct correlation (Appendix Figure 3.3). Using these relationships, we can describe the magnitude of the ice-volume as a combination of obliquity and precession (Huybers and Tziperman, 2008):

$$\mathrm{V} = \frac{\mathrm{A_o}}{\omega_\mathrm{o}} \sin(\omega_\mathrm{o} \mathrm{t}) + \frac{\mathrm{A_p}}{\omega_\mathrm{p}} \sin(\omega_\mathrm{p} \mathrm{t}). \quad (2)$$

where t is time, V is ice-volume, $\mathrm{A_o}$ is the amplitude response to obliquity, ω_o is the frequency of obliquity (40 kyr^{-1}), $\mathrm{A_p}$ is the amplitude response to precession, and ω_p is the frequency of precession (20 kyr^{-1}). Here we assume a 90° phase lag response of the ice sheets to forcing. Equation 2 demonstrates that the influence of obliquity on the ice-volume rate of change is relatively enhanced simply because the frequency of the obliquity cycle is half that of the precession cycle.

We approximate relative magnitudes of $\mathrm{A_o}$ and $\mathrm{A_p}$ in our simulations to be 40 % and 58 % by calculating the HL NA land potential ablation (based on equation S1) contributions from obliquity and precession. Due to its lower frequency, we estimate that obliquity accounts for over 58% of the ice-volume signal. The actual ice-volume responses to obliquity and precession are quite similar to this estimate (Figure 3.1).

3.5 Discussion

3.5.1 Orbital bias

One cause for the overly large precession ice-volume signal in our model results is our choice of orbital configuration. In these experiments, the value of eccentricity is a larger deviation from the mean orbit (66 % difference) than the cycle of obliquity (47 % difference). To address this bias, we ran an additional experiment using the OC1 phasing of obliquity and precession with the Pleistocene average eccentricity (0.0285) and obliquity range (22.791-24.085). The total ice-volume response decreases with a more moderate transient orbit (22 m vs. 31 m), and the resulting ice-volume spectral power distribution transfers signal strength to the obliquity frequency (73 %) compared to the default OC1 configuration (63 %) (Figure 3.3). Nonetheless, the precession ice-volume signal strength remains larger than that observed in δ^{18}O records of the EP (Lisiecki and Raymo, 2005; Huybers, 2007).

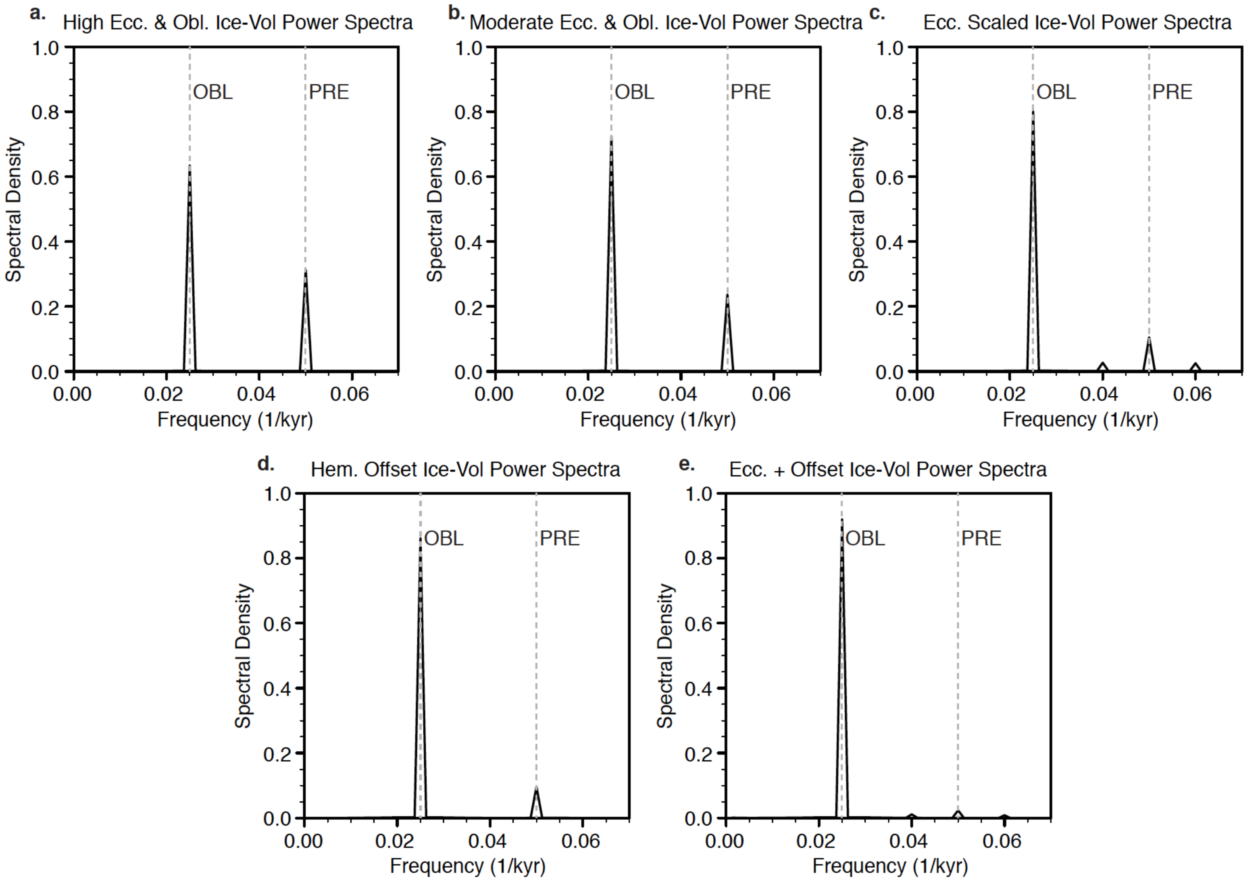

Figure 3.3: Comparison of ice-volume spectral power under different scenarios
a) Ice-volume spectral power distribution from the high eccentricity and obliquity orbital configuration (OC1). b) Ice-volume spectral power distribution from the moderate eccentricity

and obliquity orbital configuration. A moderate orbit results in a weaker precession ice-volume signal, but the precession signal is still larger than the δ^{18}O records of the EP. c) Ice-volume spectral power distribution that includes transient eccentricity modulation of the precession response shows a reduction in the precession power. d) Ice-volume spectral power distribution of the global ice-volume response that includes contributions from both hemispheres. The precession power is significantly reduced with only 15 m of MSLE fluctuations from Antarctica. e) The combination of transient eccentricity modulation and ice-volume fluctuations from Antarctica almost completely removes the precession signal, creating the “41 kyr world.”

An additional bias in our orbital configuration is that eccentricity remains constant, giving precession a large insolation forcing every 20 kyr instead of every 100 kyr or 400 kyr. We approximate the effect of transient eccentricity on modeled ice-volume spectral power distribution by decomposing the ice-volume signals into obliquity and precession components, then temporally scaling the precession signal amplitude by the percent difference between the original eccentricity (0.056596) and a 100 kyr eccentricity cycle (0.000267-0.056596). Recombining the obliquity ice-volume component with the scaled precession ice-volume component produces an eccentricity-cycle modulated ice-volume signal. The resulting spectral power distribution amplifies the obliquity power from 63 % to 80 % and reduces the precession power to 10 % (Figure 3.3).

3.5.2 Ice-volume hemispheric offset

Another consideration is that the δ^{18}O ice-volume record is not completely driven by NH forcing (Raymo et al., 2006). Because insolation forcing from precession is out of phase between hemispheres and ocean δ^{18}O proxies record global ice-volume, precession might have a significant influence on local ice-volume without producing a global δ^{18}O signal. Raymo et al. (2006) show that changes in Antarctic ice-volume during the EP can cause the precession signal to vanish from the δ^{18}O records. Given the already relatively small precession ice-volume signal strength in our model results, the precession signal also disappears with minimal variations in southern hemisphere (SH) ice-volume. If we assume that other EP ice sheets, including the Fennoscandian and Antarctic ice sheets, respond to orbital forcing in a similar manner to our NA ice sheets, we can scale our ice-volume signal to match the estimated EP MSLE variability of ~70 m (Sosdian and Rosenthal, 2009). As an example, if we use the ice-volume signal from OC1 to represent the NH ice-volume response and assume SH variations equivalent to 15 m MSLE in combination with ice δ^{18}O compositions of -30 ‰ and -45 ‰ for NH and SH ice, respectively

(Raymo et al., 2006), the precession signal contribution to the global $\delta^{18}O$ signal reduces to less than 10% with only 15 m of MSLE contribution from Antarctica (Figure 3.3). Further, combining hemispheric offset with eccentricity modulation of the precession signal almost completely removes power at the frequency of precession (2 %) (Figure 3.3). Note, here we posit that the Antarctic ice sheets respond to orbital forcing in the same manner as the modeled NA ice sheets; however, Antarctica response to orbital forcing is uncertain and might be more significantly influenced by changes in ocean currents than land-based ablation (e.g., Pollard and DeConto, 2009). Nevertheless, our results lend credibility to the hemispheric offset hypothesis given the relatively small amount of Antarctic ice melt required to remove most of the precession signal. Antarctic ice-volume variability of 15 m is reasonable since proxy evidence suggests an unstable East Antarctic ice-sheet (EAIS) during the Late Pliocene, with sea-level fluctuations of up to 10 m (Cook et al., 2013).

3.5.3 GHG fluctuations

Due to the lack of high-resolution atmospheric composition data available for the EP, we omit GHG fluctuations from our experiments. However, other modeling studies suggest a significant role for CO_2 during the last deglaciation (Abe-Ouchi et al., 2007). Further, Ruddiman (2003, 2006) shows that during the Late Pleistocene CO_2 fluctuations were significantly larger at the frequency of obliquity than precession, and these 41 kyr fluctuations in CO_2 acted nearly in-phase with ice-volume, implying a positive feedback. If such a relationship existed during the EP, it would be yet another mechanism to enhance the 41 kyr ice-volume signal. Variations in CO_2 could further reduce the amount of hemispheric offset required to produce the EP $\delta^{18}O$ records. However, additional proxy and modeling data are required to discern the magnitude and time of EP CO_2 variability.

3.5.4 Response changes after the mid-Pleistocene transition

Our simulations address the ice-volume record prior to the mid-Pleistocene transition (MPT), at which point ice-volume varies predominantly at a period of 100 kyrs. The change in the response to orbital forcing might be related to ice sheet extent. Summer insolation forcing from obliquity is strongest over the high-latitudes and reverses sign below ~45° latitude, while summer insolation forcing from precession remains uniform over much of the hemisphere. Therefore, once an ice sheet reaches lower latitudes, precession controls almost all insolation variability in the main ice sheet ablation zone. The simultaneous appearance of larger NA ice sheets and a stronger eccentricity ice-volume response after the MPT might be a consequence of more extensive ice sheets requiring a greater magnitude, low-latitude forcing to retreat. Furthermore, a more extensive ice sheet would likely not be as susceptible to vegetation feedbacks, further reducing the influence of obliquity. This theory is somewhat dependent on an increasing areal extent of the ice sheets after the MPT. While some research proposes little change in the maximum ice sheet extent through the Pleistocene (e.g., Clark and Pollard, 1998), other proxies support a less extensive ice sheet during much of the EP (e.g., Balco and Rovey, 2010).

3.6 Conclusion

Our results illustrate that no single factor completely explains the modeled ice-volume signal. Instead, amplification of the obliquity forcing by sea-ice, vegetation, and cloud feedbacks, seasonal offset of the precession forcing, and differences in cycle duration are necessary to understand the contributions of obliquity and precession to ice-volume response. These factors cause obliquity to have the dominate influence on ice sheet variability, in agreement with the Pleistocene $\delta^{18}O$ records (Lisiecki and Raymo, 2005; Huybers, 2007). Furthermore, by including eccentricity modulation of the precession ice-volume signal and invoking a reasonably small amount of ice response from Antarctica, we are able to reduce the global ice-volume response to precession and produce a signal that compares favorably with the ice-volume proxy records of the EP. Based on these results, a possible hypothesis for the “40 kyr world” involves a marginally unstable Antarctic ice sheet during the EP, which dampens the precession contribution to the $\delta^{18}O$ records, while albedo feedback amplifications allow obliquity to produce a strong signal throughout the Pleistocene.

3.7 Acknowledgements

We are grateful to William Ruddiman and anonymous reviewers whose comments improved this manuscript. We thank the Climate Change Research Lab at the University of Michigan for their discussion and suggestions. This research was funded by NSF grant OCE-0902258 awarded to C. Poulsen. Model data are available upon request.

3.8 Appendix B

In our ice sheet experiments, we used an insolation/temperature melt scheme. The melt, M, is calculated with the following equation:

$\mathrm{M} = \Delta\mathrm{t}\,(\mathcal{T}(1-\alpha)\mathrm{Q} + \mathrm{c} + 10\mathrm{T})/(1000\mathrm{L_m})$. (S1)

where M is the melt in meters, $\Delta\mathrm{t}$ is a day in seconds, α is the albedo, $\mathcal{T}$ is the transmissivity of the atmosphere, T is the lowest atmospheric layer temperature in °C, Q is the daily insolation at the top of the atmosphere in W m^{-2}, $\mathrm{L_m}$ is the latent heat of melting in J kg^{-1}, and c is a constant equal to -100 based on our modern day model experiments. Here α, $\mathcal{T}$, Q, and T, are taken from the daily GCM outputs.

The asynchronous coupling technique that allows us to capture the transient climate response to long-term orbital changes involves running the GCM with a fixed orbital configuration for 25 yr. The final 10 yr of the GCM integration are averaged and passed to the ice-sheet model to calculate surface mass balance. After forcing the ice-sheet model for 2.5 kyr with the GCM outputs, updated land surface type and topography data are fed back into the GCM along with an appropriately advanced orbital configuration (Pollard et al., 1990). Because orbits with large eccentricity alter seasonal duration, we use an angular calendar for all monthly and seasonal comparisons following Joussaume and Braconnot (1997). Each month in our angular calendar corresponds with 30° arc length of Earth's orbit around the Sun.

For the climate-ice experiments, we run two orbital cycles, equivalent to 80 kyr. The ice-sheets require a cycle to equilibrate; therefore, the first cycle is removed from our analysis. We confirm that the ice-volume signals are producing consistent cycle responses by running the OC4 orbital configuration for an additional orbital cycle (40 kyr) (Appendix Figure 3.4) and find virtually no difference in the ice-volume response between the 40-80 kyr and 80-120 kyr cycles. Given consistent cycles, we combine several of the same ice-volume cycles together to calculate the ice-volume power spectra.

No floating ice or grounding-line advance into water is allowed in the ice-sheet model. Because the Scandinavian ice sheet contains a large shelf component, we limit our ice domain to North America and Greenland. In order for ice to advance onto the continental shelf and over the Hudson Bay, we lower sea level by 275 m in this region in the ice-sheet model relative to modern day. Our artificial sea level reduction might be justified since there is no evidence that the Hudson Bay was below sea level during the Pliocene (Sohl et al., 2009). Additionally, due to the inability of the AGCM to capture valley ablation in Alaska (Marshall and Clarke, 1999), a 6°C temperature bias correction is applied to the region when running the ice-sheet model to prevent permanent ice build up. The temperature adjustment only applies to the ice sheet model component, not the GCM, and therefore, has no impact on the climate-only experiments. Furthermore, previous tests suggest that the temperature bias correction does not significantly change the pattern of our ice sheet response.

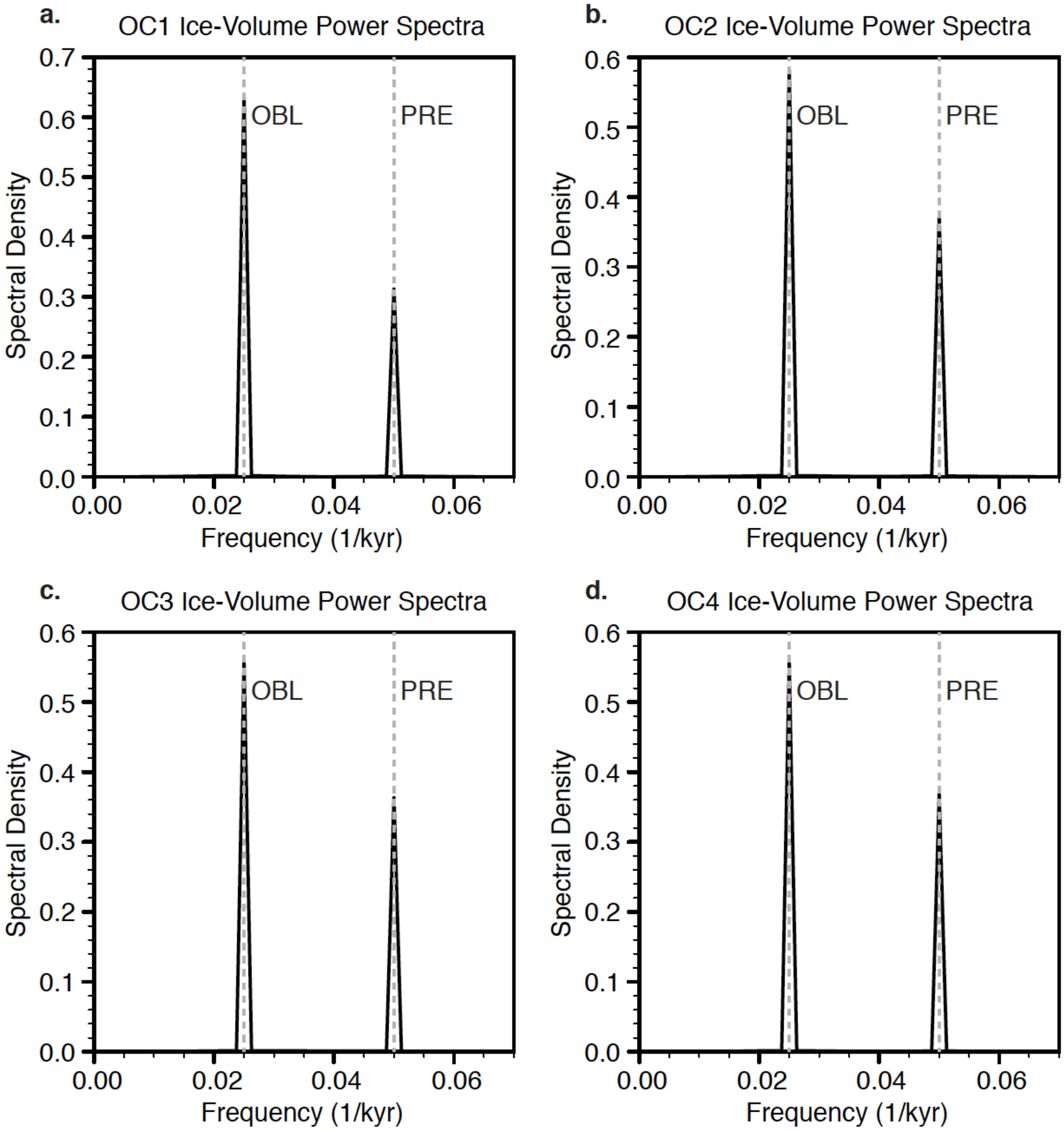

Appendix Figure 3.1: Ice-volume spectral power for all orbital configurations
(a-d) Power spectra plots for orbital configurations OC1-4. While there is a bit of variability in frequency power distribution between orbital configurations, the obliquity frequency produces a

stronger ice-volume signal than precession for all orbital configurations. Vertical dashed gray lines highlight the location of the obliquity and precession frequencies.

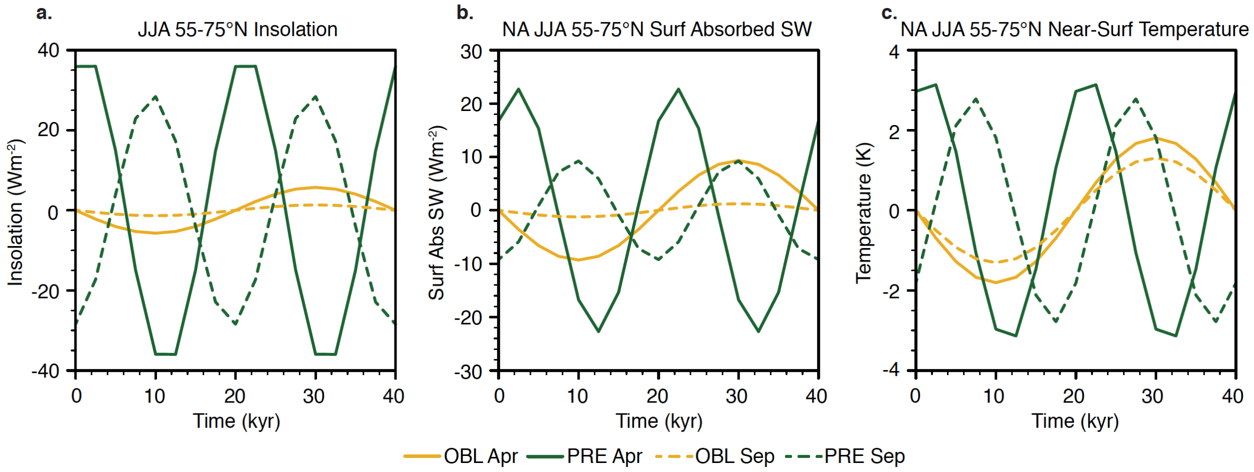

Appendix Figure 3.2: Decomposition of spring and fall climate to orbital forcing

Spatial and temporal averages of NA HL (55-75°N, 57-165°W) April (solid lines) and September (dashed lines) signals are decomposed into obliquity (oranges lines) and precession (green lines) components to highlight the seasonal differences in insolation forcing and climate response. Plots show the differences in insolation forcing between obliquity and precession over 40 kyr, equivalent to one obliquity cycle and two precession cycles. a) The insolation (W m^{-2}) contributions from obliquity and precession for April and September. b) The surface-absorbed shortwave radiation (W m^{-2}) contributions from obliquity and precession for April and September. c) The near-surface temperature (K) contributions from obliquity and precession for April and September. These plots show that the in-phase seasonal forcing of obliquity amplifies absorbed shortwave radiation and near-surface temperature responses while the out-of-phase seasonal precession forcing leads to some offset in the same responses.

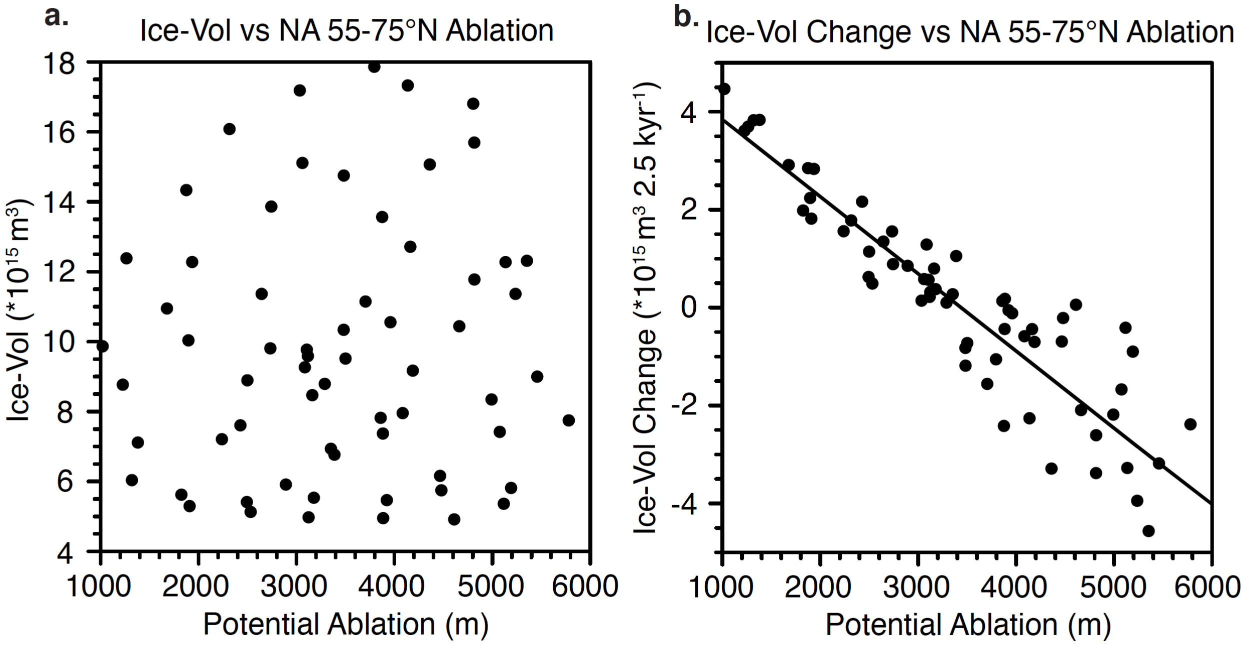

Appendix Figure 3.3: The relationship between ice and ablation

a) Ice-volume (m^3) on the y axis is plotted against average NA HL (55-75°N, 57-165°W) potential ablation (m) over land from the climate-only experiments on the x axis. There is no correlation between ice-volume and ablation. b) Ice-volume change on the y axis is plotted against potential ablation (m) over land from the climate-only experiments on the x axis. There is a strong linear relationship between the change in ice-volume and NA HL ablation, suggesting the model ice-volume is mainly in response to changes in ablation.

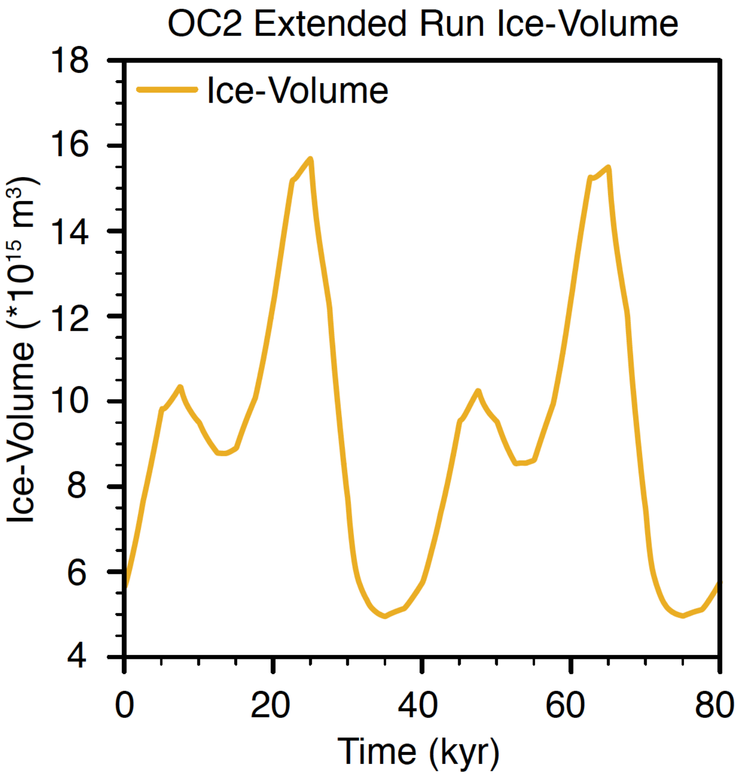

Appendix Figure 3.4: Additional orbital cycle test
OC2 was run for an additional orbital cycle to show that the differences in the ice-volume (m^3) response between cycles are minimal. The ice-volume response over the first 40 kyr is nearly identical to the second 40 kyr and shows almost no difference in spectral power.

	Starting Precession	**Starting Obliquity**	**Eccentricity**
OC1	0°	23.3085°	0.056596
OC2	90°	23.3085°	0.056596
OC3	180°	23.3085°	0.056596
OC4	270°	23.3085°	0.056596

Appendix Table 3.1: Orbital configuration
The starting values of precession, obliquity, and eccentricity for the four transient orbital configurations. The only difference between orbital configurations is the phasing of precession relative to obliquity. Obliquity ranges from 22.079 to 24.538°, precession includes 360° cycles representing the prograde angle from perihelion to NH Vernal Equinox, and eccentricity is held constant at 0.056596. Both the obliquity range and eccentricity represent the extremes of the Pleistocene.

Bibliography

Abe-Ouchi A., T. Segawa, and F. Saito (2007), Climatic Conditions for modelling the Northern Hemisphere ice sheets throughout the ice age cycle. Clim. Past, 3, 423-438, doi:10.5194/cp-3-423-2007.

Alder, J. R., S. W. Hostetler, D. Pollard, and A. Schmittner (2011), Evaluation of a present-day climate simulation with a new coupled atmosphere-ocean model GENMOM, Geosci. Model Devel., 4, 69-83, doi:10.5194/gmd-4-69-2011.

Balco, G., and C. W. Rovey (2010), Absolute chronology for major Pleistocene advances of the Laurentide Ice Sheet, Geology, 38(9), 795–798, doi:10.1130/G30946.1.

Bender, M. L. (2002), Orbital tuning chronology for the Vostok climate record supported by trapped gas composition, Earth Planet. Sci. Lett., 204(1-2), 275–289, doi:10.1016/S0012-821X(02)00980-9.

Berger, A., and M. F. Loutre (1991), Insolation values for the climate of the last 10 million years, Quat. Sci. Rev., 10(4), 297–317, doi:10.1016/0277-3791(91)90033-Q.

Berger, A., X. S. Li, and M. F. Loutre (1999), Modelling northern hemisphere ice volume over the last 3 Ma, Quat. Sci. Rev., 18(1), 1–11, doi:10.1016/S0277-3791(98)00033-X.

Birchfield, G. E., J. Weertman, and A. T. Lunde (1981), A paleoclimate model of Northern Hemisphere ice sheets, Quat. Res., 15(2), 126–142, doi:10.1016/0033-5894(81)90100-9.

Clark, P. U., and D. Pollard (1998), Origin of the middle Pleistocene transition by ice sheet erosion of regolith, Paleoceanography, 13(1), 1–9, doi:10.1029/97PA02660.

Claussen, M., J. Fohlmeister, and A. Ganopolski (2006), Vegetation dynamics amplifies precessional forcing, Geophys. Res. Lett., 33(9), L00709, doi:10.1029/2006GL026111.

Cook, C. P. et al. (2013), Dynamic behaviour of the East Antarctic ice sheet during Pliocene warmth, Nature Geosci, 6(9), 765–769, doi:10.1038/NGEO1889.

DeConto, R. M., D. Pollard, P. A. Wilson, H. Palike, C. H. Lear, and M. Pagani (2008), Thresholds for Cenozoic bipolar glaciation, Nature, 455, 652–656, doi:10.1038/nature07337.

Erb, M. P., A. J. Broccoli, and A. C. Clement (2013), The Contribution of Radiative Feedbacks to Orbitally Driven Climate Change, J. Climate, 26(16), 5897–5914, doi:10.1175/JCLI-D-12-00419.1.

Gallimore, R. G., and J. E. Kutzbach (1995), Snow Cover and Sea-Ice Sensitivity to Generic Changes in Earth Orbital Parameters, J. Geophys. Res., 100(D1), 1103–1120, doi:10.1029/94JD02686.

Gallimore, R. G., and J. E. Kutzbach (1996), Role of orbitally induced changes in tundra area in the onset of glaciation, Nature, 381(6582), 503–505, doi:10.1038/381503a0.

Herrington, A. R., and C. J. Poulsen (2012), Terminating the Last Interglacial: The Role of Ice Sheet–Climate Feedbacks in a GCM Asynchronously Coupled to an Ice Sheet Model, J. Clim., 25(6), 1871–1882, doi:10.1175/JCLI-D-11-00218.1.

Horton, D. E., C. J. Poulsen, and D. Pollard (2010), Influence of high-latitude vegetation feedbacks on late Palaeozoic glacial cycles, Nature Geosci, 3(8), 572–577, doi:10.1038/ngeo922.

Huybers, P. (2006), Early Pleistocene Glacial Cycles and the Integrated Summer Insolation Forcing, Science, 303(5786), 508-511, doi:10.1126/science.1125249.

Huybers, P. (2007), Glacial variability over the last two million years: an extended depth-derived age model, continuous obliquity pacing, and the Pleistocene progression, Quat. Sci. Rev., 26(1-2), 37–55, doi: 10.1016/j.quascirev.2006.07.013.

Huybers, P., and C. Wunsch (2005), Obliquity pacing of the late Pleistocene glacial terminations, Nature, 434(7032), 491–494, doi:10.1038/nature03401.

Huybers, P., and E. Tziperman (2008), Integrated summer insolation forcing and 40,000-year glacial cycles: The perspective from an ice-sheet/energy-balance model, Paleoceanography, 23(1), doi:10.1029/2007PA001463.

Jackson, C. S., and A. J. Broccoli (2003), Orbital forcing of Arctic climate: mechanisms of climate response and implications for continental glaciation, Clim. Dynam., 21(7-8), 539–557, doi:10.1007/s00382-003-0351-3.

Joussaume, S., and P. Braconnot (1997), Sensitivity of paleoclimate simulation results to season definitions, J. Geophys. Res., 102(D2), 1943-1956, doi:10.1029/96JD01989.

Kaplan, J. O. et al. (2003), Climate change and Arctic ecosystems: 2. Modeling, paleodata-model comparisons, and future projections, J. Geophys. Res., 108(D19), 8171, doi:10.1029/2002JD002559.

Lee, S. Y., and C. J. Poulsen (2005), Tropical Pacific climate response to obliquity forcing in the Pleistocene, Paleoceanography, 20(4), PA4010, doi:10.1029/2005PA001161.

Lee, S. Y., and C. J. Poulsen (2008), Amplification of obliquity forcing through mean-annual and seasonal atmospheric feedbacks, Clim. Past, 4, 205-213, doi:10.5194/cp-4-205-2008.

Lisiecki, L. E., and M. E. Raymo (2005), A Pliocene-Pleistocene stack of 57 globally distributed benthic delta O-18 records, Paleoceanography, 20(1), PA1003, doi:10.1029/2004PA001071.

Lisiecki, L. E., and M. E. Raymo (2007), Plio–Pleistocene climate evolution: trends and transitions in glacial cycle dynamics, Quat. Sci. Rev., 26(1-2), 56–69, doi:10.1016/j.quascirev.2006.09.005.

Loutre, M. F., D. Paillard, F. Vimeux, and E. Cortijo (2004), Does mean annual insolation have the potential to change the climate? Earth Planet. Sci. Lett., 221(1-4), 1–14, doi:10.1016/S0012-821X(04)00108-6.

Mantsis, D. F., A. C. Clement, A. J. Broccoli, and M. P. Erb (2011), Climate Feedbacks in Response to Changes in Obliquity, J. Climate, 24(11), 2830–2845, doi:10.1175/2010JCLI3986.1.

Marshall, S. J., and G. Clarke (1999), Modeling North American freshwater runoff through the last glacial cycle, Quat. Res., 52(3), 300–315, doi:10.1006/qres.1999.2079.

Milankovitch, M. (1941), Kanon der Erdbestrahlung und seine Andwendung auf das Eiszeiten-problem. R. Serbian Acad., Belgrade.

Petit, J. R. et al. (1999), Climate and atmospheric history of the past 420,000 years from the Vostok ice core, Antarctica, Nature, 399, 429–436, doi:10.1038/20859.

Philander, S. G., and A. V. Fedorov (2003), Role of tropics in changing the response to

Milankovich forcing some three million years ago, Paleoceanography, 18(2), 1045, doi:10.1029/2002PA000837.

Pollard, D. (1980), A simple parameterization for ice sheet ablation rate, Tellus, 32(4), 384–388, doi:10.1111/j.2153-3490.1980.tb00965.x.

Pollard, D., I. Muszynski, S. H. Schneider, and S. L. Thompson (1990), Asynchronous coupling of ice sheet and atmospheric forcing models, Ann. Glac., 6, 255-272, doi:10.5194/tc-6-255-2012.

Pollard, D., and R. M. DeConto (2009), Modelling West Antarctic ice sheet growth and collapse through the past five million years, Nature, 458, 329–332, doi:10.1038/nature07809.

Pollard, D., and R. M. DeConto (2012), Description of a hybrid ice sheet-shelf model, and application to Antarctica, Geosci. Model Devel., 5(5), 1273–1295, doi:10.5194/gmd-5-1273-2012.

Ravelo, A. C., D. H. Andreasen, M. Lyle, A. O. Lyle, and M. W. Wara (2004), Regional climate shifts caused by gradual global cooling in the Pliocene epoch, Nature, 429, 263–267, doi:10.1038/nature02567.

Raymo, M. E., and K. Nisancioglu (2003), The 41 kyr world: Milankovitch's other unsolved mystery, Paleoceanography, 18, 1011, doi:10.1029/2002PA000791.

Raymo, M. E., L. E. Lisiecki, and K. H. Nisancioglu (2006), Plio-Pleistocene Ice Volume, Antarctic Climate, and the Global δ^{18}O Record, Science, 313, 492–495, doi:10.1126/science.1123296.

Robinson, A., R. Calov, and A. Ganopolski (2010), An efficient regional energy-moisture balance model for simulation of the Greenland Ice Sheet response to climate change, Cryosphere, 4(2), 129–144, doi:10.5194/tc-4-129-2010.

Roe, G. (2006), In defense of Milankovitch, Geophys. Res. Lett., 33(24), L24703, doi:10.1029/2006GL027817.

Ruddiman, W.F. (2003), Orbital insolation, ice volume, and greenhouse gases. Quat. Sci. Rev. 22, 1597–1629, doi: 10.1016/S0277-3791(03)00087-8.

Ruddiman, W.F. (2006), Orbital changes and climate. Quat. Sci. Rev., 25, 3092–3112, doi: 10.1016/j.quascirev.2006.09.001.

Sohl, L.E., M.A. Chandler, R.B. Schmunk, K. Mankoff, J.A. Jonas, K.M. Foley, and H.J.

Dowsett (2009), PRISM3/GISS topographic reconstruction. USGS.

Sosdian, S., and Y. Rosenthal (2009), Deep-Sea Temperature and Ice Volume Changes Across the Pliocene-Pleistocene Climate Transitions, Science, 325, 306–310, doi:10.1126/science.1169938.

Tabor, C. R., C. J. Poulsen, and D. Pollard (2014), Mending Milankovitch's theory: obliquity amplification by surface feedbacks, Clim. Past, 10(1), 41–50, doi:10.5194/cp-10-41-2014.

Tuenter, E., S. L. Weber, F. J. Hilgen, L. J. Lourens, and A. Ganopolski (2004), Simulation of climate phase lags in response to precession and obliquity forcing and the role of vegetation, Clim. Dyn., 24(2-3), 279–295, doi:10.1007/s00382-004-0490-1.

Tuenter, E., S. L. Weber, F. J. Hilgen, and L. J. Lourens (2005), Sea-ice feedbacks on the climatic response to precession and obliquity forcing, Geophys. Res. Lett., 32(24), doi: 10.1029/2005GL024122.

van den Berg, J., R. van de Wal, and H. Oerlemans (2008), A mass balance model for the Eurasian ice sheet for the last 120,000 years, Global Planet. Change, 61(3-4), 194–208, doi:10.1016/j.gloplacha.2007.08.015.

Vettoretti, G., and W. R. Peltier (2004), Sensitivity of glacial inception to orbital and greenhouse gas climate forcing, Quat. Sci. Rev., 23(3-4), 499–519, doi:10.1016/j.quascirev.2003.08.008.

Chapter 4: Simulating the Mid-Pleistocene Transition Through Regolith Removal

4.1 Abstract

Quaternary $\delta^{18}O$ ice-volume proxy records show a transition from high frequency, small-amplitude glacial cycles to low frequency, large-amplitude glacial cycles. This reorganization of the climate system, termed the mid-Pleistocene transition (MPT), is thought to reflect a change in land-ice response to orbital forcing, despite no significant change in orbital cycles during this period. One potential explanation for the MPT proposes that gradual erosion of high-latitude northern hemisphere regolith by multiple cycles of glaciation caused a transition in ice sheet response to external forcing. Here, we explore this "regolith hypothesis" using a complex Earth system model. We show that simulating a transition from deformable sediment to crystalline bedrock produces an evolution in ice-volume response similar to proxy reconstructions of the MPT. The simulated change in ice-volume response is due to a combination of climate and ice-flow changes, with crystalline bedrock producing thicker, colder ice sheets that accumulate more snowfall and have a smaller ablation zone. Further, experiments that include transient eccentricity-amplifying CO_2 forcing show only small differences in ice response compared to those with orbital forcing only, suggesting that cycles of CO_2 were not the primary cause of the MPT.

4.2 Introduction

The MPT (1.2 to 0.7 Ma) (Clark et al., 2006) represents a change in Earth's climate state from one characterized by 41 kyr glacial cycles with ~70 m sea-level amplitude to one dominated by100 kyr glacial cycles with ~120 m sea-level amplitude (e.g. Elderfield et al., 2012). In this way, the MPT is one of the most dramatic climate transformations of the Quaternary (2.58 to 0 Ma) and represents a fundamental change in the internal variability of the climate system (Pisias and Moore, 1981). The cause of the MPT is uncertain; reconstructions show minimal change in orbital forcing (Berger and Loutre, 1991) or glacial CO_2 (~30 ppmv) (Hönisch et al., 2009) across the interval. In the absence of an obvious direct forcing, numerous hypotheses have been proposed to explain the MPT including gradual cooling (e.g. Berger et al., 1999), sea-ice feedbacks (Tziperman and Gildor, 2003), climate phase-locking with orbital forcing (Rial et al., 2013), and Antarctic ice sheet expansion (Elderfield et al., 2012).

Here, we explore a hypothesis for the MPT that invokes removal of northern North American regolith (Clark et al., 2006; Clark and Pollard, 1998). In theory, chemical and physical weathering of bedrock through the Tertiary produced thick (up to 60 m) regolith on northern North America (Clark et al., 1999; Setterholm and Morey, 1995). With the onset of North American glaciation in early Pleistocene, this thick regolith provided a deformable substrate that reduced basal shear stresses and promoted thin, extensive ice sheets. As a result, early Pleistocene ice sheets were relatively thin and warm with large ablation zones, and therefore, retreated under moderate summer insolation forcing of obliquity. Over time, the erosion of the regolith and gradual exposure of crystalline bedrock by multiple cycles of ice advance and retreat resulted in greater basal shear stresses, which caused ice sheets to grow thicker. Greater insolation forcing, potentially produced by a combination of obliquity and eccentricity/precession, or some other internal feedback triggered by the larger ice sheets was then necessary to cause complete retreat of these thicker, colder ice sheets, resulting in ~100 kyr period glacial cycles.

A unique prediction of the regolith hypothesis is that early Pleistocene ice sheets were as aerially extensive as late Pleistocene ice sheets, despite large differences in ice-volume. In support of this prediction, several proxies show that early Pleistocene ice sheets were as extensive as late Pleistocene ice sheets (Boellstorf, 1978; Balco et al., 2005; Joyce et al., 1993; Roy et al., 2004) and a change in erosion from weathered soils to crystalline bedrock across the MPT (e.g. Andrews, 1993; Farrell et al., 1995; Peucker-Ehrenbrink and Blum, 1998; Roy et al., 2004). While some evidence suggests that most of the regolith was stripped by the Laurentide ice sheet during early Pleistocene glacial advances (Balco and Rovey, 2010; Refsnider and Miller, 2013), temporal gaps and large age uncertainties leave poor constraints on the timing of regolith export with respect to the MPT. Finally, both $\delta^{13}C$ (Raymo et al., 2004; Clark et al., 2006; Lawrence et al., 2010; Lisiecki, 2014) and ε_{Nd} (Pena and Goldstein, 2014) records suggest Atlantic circulation changes occurred across the MPT such as greater glacial shoaling of northern component water, increased 2300-4010 m southern component water, and reduction of the obliquity signal in 2300-4010 m water. The cause of these circulation shifts cannot be directly determined from the data; however, increased ice sheet size resulting from a reduction in regolith provides a possible North Atlantic source for many of the changes in overturning.

Previous modeling studies show basal sliding plays an important role in the cyclic response of ice-volume to orbital forcing (Clark and Pollard, 1998; Ganopolski and Calov, 2011). However, those studies used simplified models that were unable to capture the details of mid- and high-latitude climate dynamics, and thus, were unable to comprehensively examine the climate mechanisms responsible for changes in ice-volume response (See Model Comparison Section for additional discussion). Here, we examine the role of regolith on the ice sheet cycles of the Pleistocene using a complex Earth system model with dynamic atmosphere, vegetation, sea ice, and land-ice components.

4.3 Methods

4.3.1 Model and Coupling

To explore the role of regolith in the MPT, we use the GENESIS GCM and land surface (LSX) model (Alder et al., 2011) coupled with the BIOME4 vegetation model (Kaplan et al., 2003) and Pennsylvania State University (PSU) ice-sheet model (Pollard and DeConto, 2012a). The atmosphere GCM is run at T31 spectral resolution (~3.75°) with 18 vertical levels and the LSX model is run at 2°x2° resolution. GENESIS includes a slab ocean that calculates diffusive heat transport as a function of latitude and temperature gradient, and contains a dynamic sea ice module. The GCM is synchronously coupled with the BIOME4 vegetation model. BIOME4 is an equilibrium vegetation model with plant functional types (PFTs) determined from boundary conditions of soil type and CO_2, and GCM calculations of temperature, insolation, and precipitation. PFTs update annually from GCM outputs. The PSU ice-sheet model is a thermomechanical ice-sheet model based on the shallow ice approximation. Here, only the land-ice component of the model is active and is run at 0.25°x0.5° resolution with 10 vertical levels. The ice domain is limited to North America and Greenland, and sea level is lowered over the Hudson Bay region to allow ice sheet expansion. Further, due to the inability of the AGCM to capture fine-scale valley ablation, a 6°C temperature bias correction is applied to Alaska in the ice-sheet model to prevent unrealistic ice build up (Marshall and Clarke, 1999; Tabor et al., 2015). For this study, an insolation/temperature melt scheme (Pollard, 1980; van den Berg et al.,

2008) is used in place of the commonly employed positive-degree-day melt scheme because it produces a more realistic ice-volume response over long time scales (Robinson et al., 2010, Tabor et al., 2014).

Given the slow response time of the ice sheet model, synchronous coupling of all model components is computationally infeasible. Instead, an asynchronous coupling technique is used in which the GENESIS GCM and BIOME4 vegetation models are run with a fixed orbital and GHG configuration for 25 years. Then, the ice sheet model is forced for 2.5 kyr using climatology from the final 10 years of the GCM. The resulting ice sheet extents and topography with updated orbital conditions are fed into the GCM and run to a new equilibrium state. Due to the continuous nature of the orbital forcing and the rapid response time of the slab ocean, 15 years of spin-up prior to the averaging period is sufficient to produce near equilibrium climate states. This method allows simulation of large-scale climate responses to orbital forcing with current computational limitations (Horton et al., 2010; Pollard et al., 1990).

4.3.2 Experiment Design

All experiments are initialized with preindustrial geography, topography, and land-surface types (Peltier, 2004). Orbital cycles are simulated using pure (simple, idealized) sinusoidal orbits of obliquity, precession, and eccentricity that represent the calculated cyclical ranges of the Pleistocene (Berger and Loutre, 1991) (Figure 4.1). For regular, consistent orbital cycles and computational efficiency, eccentricity, obliquity, and precession are scaled to cycles of 80, 40, and 20 kyr, respectively. This orbital configuration produces two local maxima in high-latitude summer (JJA) insolation at 32.5 and 75 kyr (Figure 4.1). The 32.5 kyr summer insolation peak is relatively moderate and is driven mainly by obliquity, whereas the 75 kyr peak is greater, produced by a combination of high obliquity and eccentricity. Experiments include two greenhouse gas (GHG) configurations, one with fixed GHG concentrations representative of an average of the last 400 kyr (CO_2=230 ppmv, CH_4=520 ppbv, N_2O=250 ppbv) (Bender, 2002; Petit et al., 1999) and the other with a transient CO_2 cycle. The transient CO_2 forcing roughly mimics the saw-tooth CO_2 pattern of the last glacial cycle (Petit et al., 1999), with a range from 180 to 280 ppmv that is appropriately scaled to the idealized orbital configuration duration and acts to enhance ice-volume spectral power at the frequency of eccentricity because it cycles at the same 80 kyr period. The timing of peak CO_2 in our model occurs several thousand years later than the insolation/CO_2 relationship observed in newer high-resolution CO_2 records (Landais et al, 2013; Marcott et al, 2014). We discuss the implications of this timing in the Role of CO_2 Section.

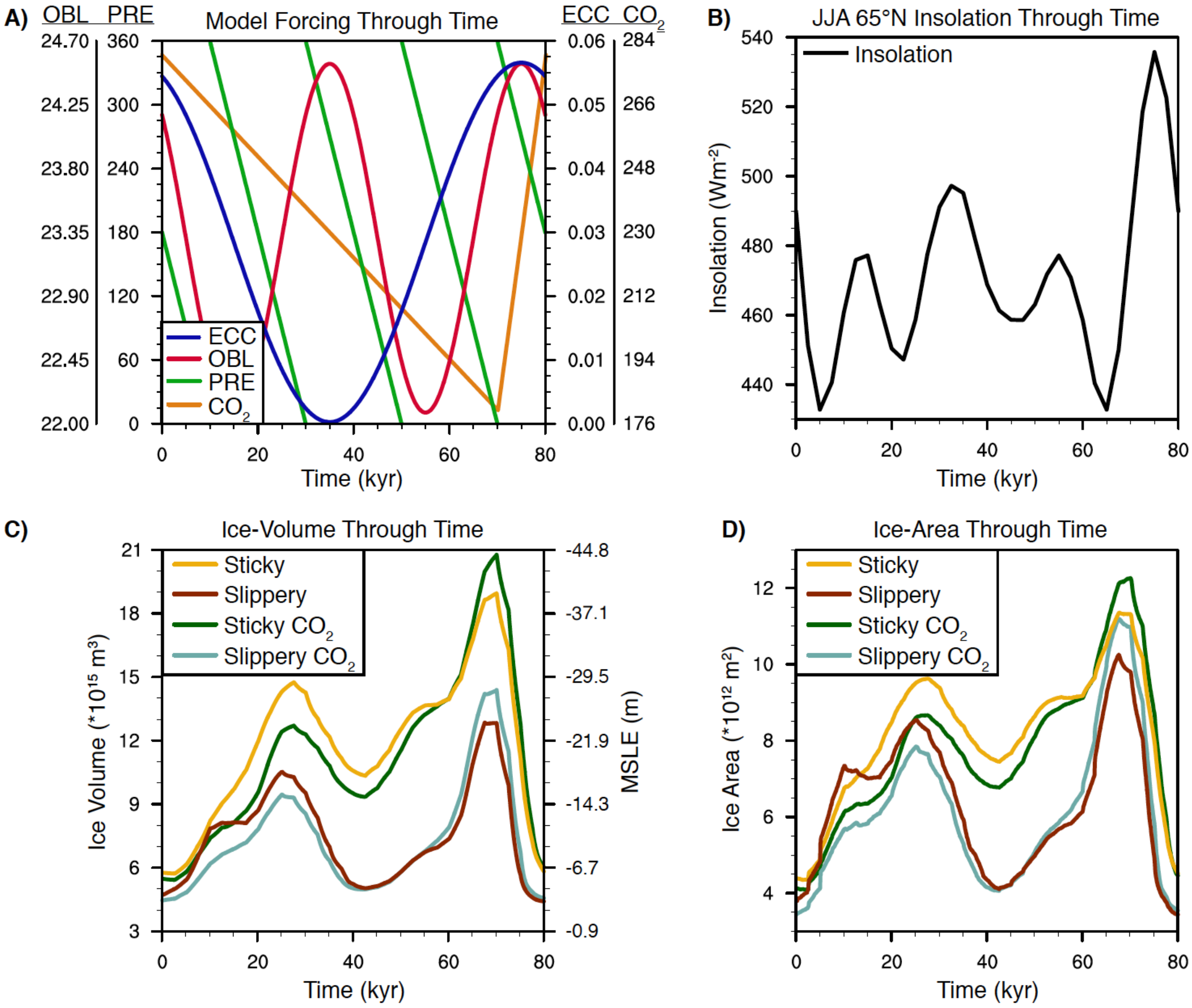

Figure 4.1: Experiment forcings and ice responses
A) Schematic of external model forcings. Model forcings include 20 kyr cycles of precession, 40 kyr cycles of obliquity, and 80 kyr cycles of eccentricity, each with ranges representing those of the Pleistocene (Berger and Loutre, 1991). Transient CO_2 forcing roughly simulates the cycles and range of late Pleistocene reconstructions (Petit et al., 1999). B) High latitude average summer (JJA) insolation at 65°N through time. C) The ice volume (m^3) and D) ice-area (m^2) response to transient orbital and CO_2 forcings.

In the model, different regolith scenarios are simulated by changing the basal sliding coefficient. Basal sliding is calculated with a drag law:

$$\mu_b = C' \, |\tau_b|^{m-1} \, \tau_b. \quad (1)$$

where μ_b is basal sliding velocity, τ_b is basal stress, and m = 2. Implicitly, C' represents basal sedimentology and hydrology and is defined by:

$C' = (1 - r)\, C_{froz} + r\, C(x, y)$ with $r\ = \max\,[0, \min\left(1, \frac{T_b + 3}{3}\right)]$. (2)

where $C(x, y)$ is the full sliding coefficient, C_{froz} is no sliding, and T_b is the basal temperature relative to the pressure melting point. Here $C(x, y) = 10^{-7}$ m a^{-1} Pa^{-2} to represent a bed of deformable sediment and $C(x, y) = 10^{-11}$ m a^{-1} Pa^{-2} to represent crystalline bedrock. These values roughly correspond to the range of values found to be appropriate for simulating flow rates in Antarctica (Pollard and DeConto, 2012b). Four experiments are carried out that simulate the land-ice response to orbital forcing over either regolith (slippery-bed) or crystalline bedrock (sticky-bed), with either fixed or transient CO_2.

Each experiment is run for 160 kyr, equivalent to two complete orbital cycles of eccentricity. Tests show that after the first cycle, the ice sheet model reaches a transient equilibrium state with no significant trend in ice-volume between cycles (Appendix Figure 4.1)(Tabor et al., 2015). For this reason, the first orbital cycle is not included in our analysis. Given the consistent response of subsequent ice-volume cycles, we append several of the same ice-volume cycle together to calculate the ice-volume power spectra. In addition, to account for seasonal changes due to eccentricity variability, an angular calendar is applied to all seasonal comparisons with each month corresponding to 30° arc length of Earth's orbit around the Sun (Joussaume and Braconnot, 1997).

4.4 Results

4.4.1 Ice-Volume and Area

With a sticky-bed, ice-area and volume grow from minima of $4.3*10^3$ km^2 and $5.65*10^6$ km^3 under warm high-latitude summer conditions to maxima of $11.3*10^3$ km^2 and $18.89*10^6$ km^3 when summer temperatures cool. The sticky-bed land-ice cycle has a mean sea level equivalent (MSLE) amplitude of 34 m. In comparison, the slippery-bed ice sheets increase from ice-area and volume minima of $3.4*10^3$ km^2 and $4.34*10^6$ km^3 to maxima of $10.2*10^3$ km^2 and $12.78*10^6$ km^3, corresponding to 20 m MSLE variability. Ice-volume cycle amplitude increases by roughly 70 % with a change from slippery to sticky bedding (Figure 4.1). This result is consistent with modeling and isotopic studies that show late Pleistocene (0.7 – 0 Ma) North American ice-volume cycles had roughly 75 % greater amplitude than early Pleistocene (2.58 – 1.2 Ma) North

American ice-volume cycles (e.g. Bintanja and van de Wal, 2008). Further, visual comparison of the Lisiecki and Raymo (2005; hereafter LR04) stacked benthic foraminifera $\delta^{18}O$ record against our simulated ice-volume record shows similarity between the 41 kyr cycles that characterize the early Pleistocene and the saw-tooth 100 kyr cycles that characterize the late Pleistocene (Lisiecki and Raymo, 2005) (Figure 4.2). Both the LR04 $\delta^{18}O$ records of the early Pleistocene and our slippery-bed experiment have somewhat symmetric, low amplitude cycles that follow the insolation forcing of obliquity, whereas the LR04 $\delta^{18}O$ records of the late Pleistocene and our sticky-bed experiment are less symmetric with larger amplitudes and durations (Ashkenazy and Tziperman, 2004; Huybers, 2007; and Lisiecki and Raymo, 2007).

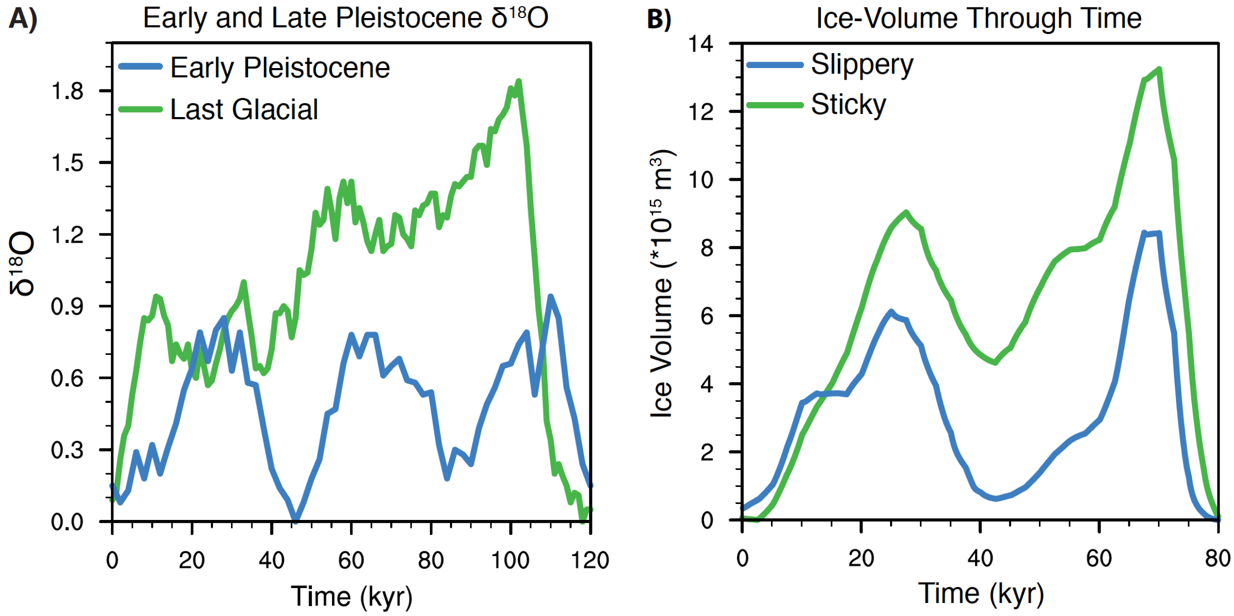

Figure 4.2: Comparison of select glacial cycles and simulated ice-volume
A) Example $\delta^{18}O$ variability from the early (1400 - 1280 ka) and late Pleistocene (120 - 0 ka). B) Model ice-volume responses for the two basal sliding conditions. The sticky-bed produces an ice-volume response almost twice as large as the slippery-bed, similar to the early and late Pleistocene $\delta^{18}O$ signals, respectively. Further, the sticky-bed does not completely retreat under moderate summer insolation forcing. Differences in durations between example $\delta^{18}O$ cycles and simulated ice-volume cycles are due to a shortened duration of orbital cycles in our experiments.

There is also agreement between our simulated ice-area and proxy reconstructions. Many proxy records indicate that ice sheets had similar extents during both the early and late Pleistocene (e.g. Balco et al., 2005; Joyce et al., 1993; Roy et al., 2004). In our simulations, the difference in maximum ice-area between slippery and sticky-beds is only ~10 % (Figure 4.1), with most of the difference coming from the Cordilleran ice sheet. The southern most extents of the Laurentide ice sheets are also quite similar (48.1 versus 46.9 °N) between simulations. While the relative changes in our ice-sheet simulations agree with proxy reconstructions, the absolute magnitudes of simulated ice-area and volume are smaller than proxy reconstructions suggest for North American ice-volume of the late Pleistocene (max amplitude of ~34 versus ~70 msle) (Bintanja and van de Wal, 2008). We discuss possible causes for this discrepancy in the Limitations and Justifications section.

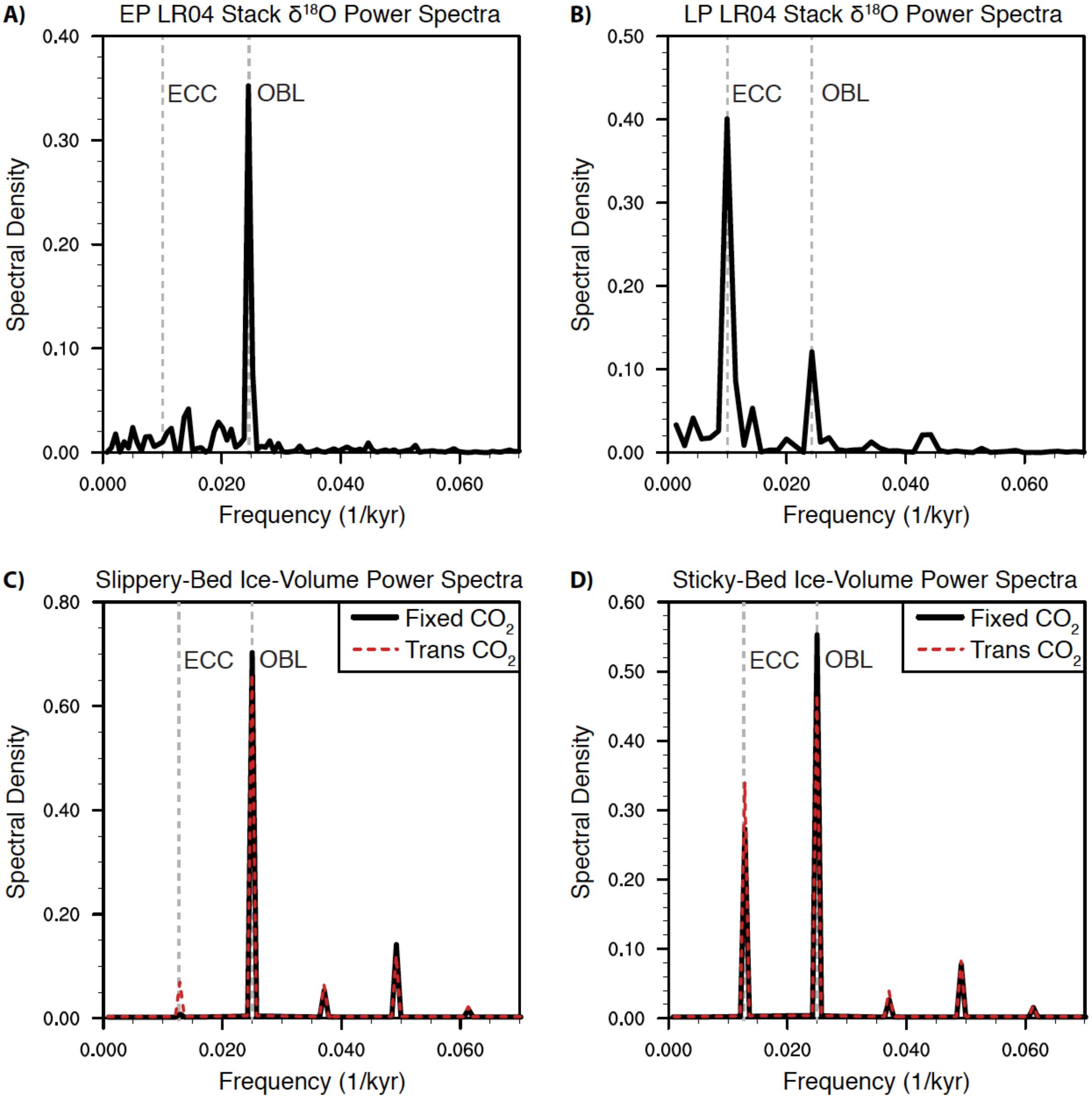

Figure 4.3: Proxy and model ice-volume spectral power

A) Early Pleistocene (EP) δ^{18}O spectral power resides mainly at the frequency of obliquity. B)

Late Pleistocene (LP) $\delta^{18}O$ spectral power resides mainly at 100 kyr^{-1} frequency. C) Slippery-bed ice-volume responses show most power at the frequency of obliquity. D) Sticky-bed ice-volume responses show an increase at the frequency of eccentricity, which is closer to the LR04 late Pleistocene $\delta^{18}O$ record. Idealized CO_2 cycles have a small effect on the distribution of spectral power. Gray dashed lines mark the frequencies of obliquity and eccentricity.

4.4.2 Spectral Power

Spectral analysis of the LR04 $\delta^{18}O$ record over the early Pleistocene shows a dominant signal at the frequency of the obliquity cycles (Figure 4.3). Our slippery-bed model results display a similar response, with 70 % of the ice-volume signal attributable to obliquity and only 0.6 % attributable to eccentricity (Figure 4.3). The dominance of the obliquity signal arises from a combination of albedo feedbacks, seasonal offsets, and orbital cycle duration differences between obliquity and precession (for details see Tabor et al., 2015). In contrast, the late Pleistocene interval of the LR04 $\delta^{18}O$ record shows strong spectral power at the frequencies of both eccentricity and obliquity (Figure 4.3). Likewise, a significant increase in spectral power at the frequency of the eccentricity cycle occurs when we reduce basal sliding in the ice sheet model (Figure 4.3). Obliquity still controls the spectral range with 55 % of the spectral power but eccentricity now contributes 27 %. The redistribution of spectral power in our experiments due to changes in basal sliding are not as dramatic as the LR04 $\delta^{18}O$ record; however, they show a similar shift. Further, the LR04 $\delta^{18}O$ record represents an average of multiple records, over multiple orbital cycles and is not a direct measure of ice-volume (see Model/Proxy Discrepancies Section).

4.4.3 Ice Dynamics

The similarities in ice-area and differences in ice-volume between basal sliding experiments are partially due to differences in ice dynamics. In the slippery-bed experiment, low basal drag results in ice flow mainly by sliding over the substrate. In the sticky-bed experiment, greater basal drag reduces basal sliding and leads to ice flow by internal deformation. Basal sliding allows for faster flowing ice sheets than internal deformation alone (Clark and Pollard, 1998), which causes the slippery-bed ice sheets to flow more quickly than the sticky-bed ice sheets and results in a lower profile (Figure 4.4).

Basal flow relates to the fraction of the ice sheets frozen to the bed. Ice sheets frozen to the bed can only flow through internal deformation while ice sheets at the pressure melting point can also flow by sliding over the substrate. In our experiments, greater portions of the slippery bed ice sheets are frozen to the bed due to a relatively lower pressure melting point, resulting from being thinner (Appendix Figure 4.2). However, between bed configurations, the difference in frozen fraction is small while the difference in sliding rate is large.

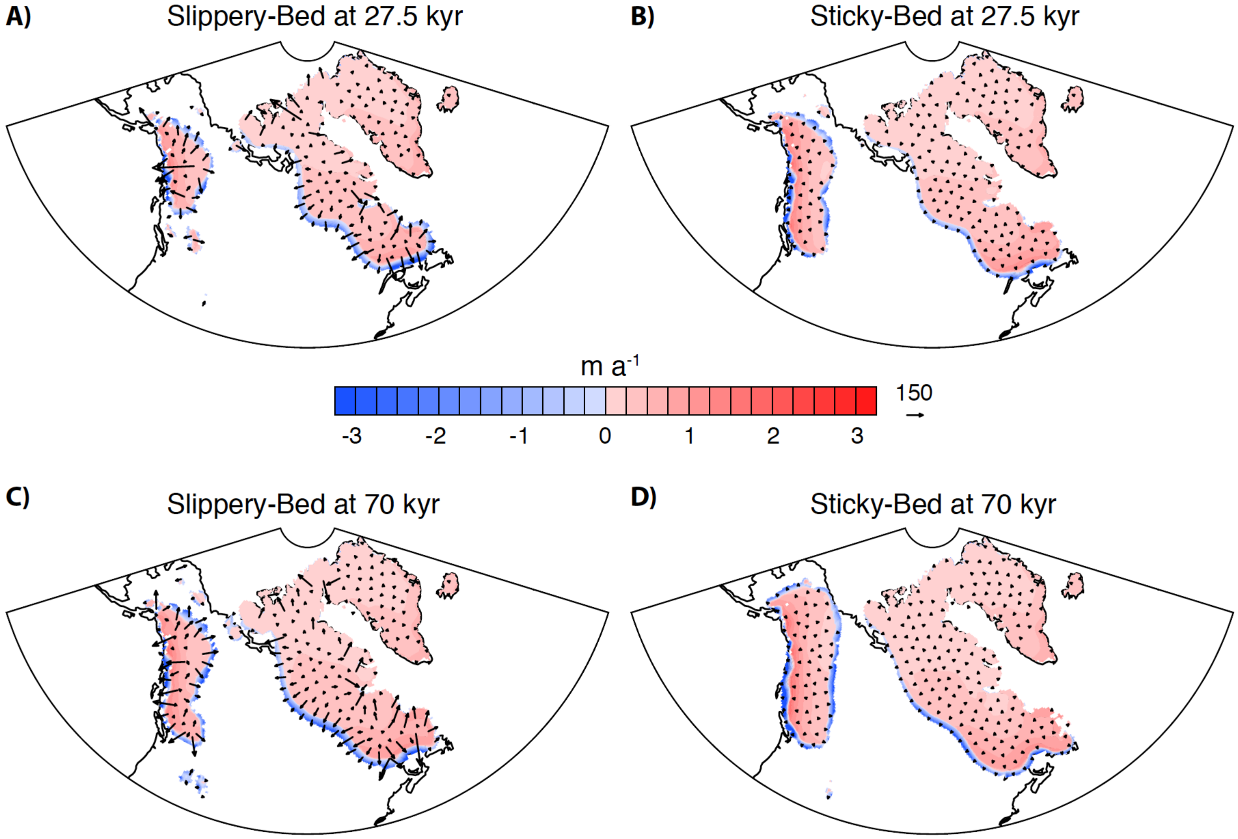

Figure 4.4: Ice ablation and basal sliding during two local maxima in ice-volume
A) Areas of ice accumulation and ablation (m a^{-1}) and basal flow rates (m a^{-1}) of the slippery-bed experiment at 27.5 kyr. B) Areas of ice accumulation and ablation (m a^{-1}) and basal flow rates (m a^{-1}) of the sticky-bed experiment at 27.5 kyr. C) and D) are the same as A) and B), respectively, except at 70 kyr. The slippery-bed ice sheets (A, C) show a larger ablation zone and faster flow than the sticky-bed ice sheets (B, D).

The difference in ice flow rates between experiments helps produce differences in ice sheet sensitivity, with the slippery-bed ice sheets responding more rapidly and significantly to changes in insolation. In the slippery-bed experiment ice both flows and wastes rapidly. When the climate cools, the slippery-bed ice sheets quickly expand over regions favorable to ice accumulation in the high-latitudes of North America. As the climate warms, the low profile and continued rapid ice flow into the warm continental interior exacerbates ice sheet mass loss and retreat (Figure

4.4). In contrast, the sticky-bed ice sheets responses are slower and less pronounced over most of the orbital cycle. During cold summers, the sticky-bed ice sheets grow thicker, creating a larger ice-volume to area ratio than the slippery-bed ice sheets. When the climate subsequently warms, the steeper profile and slow advance of the sticky-bed ice sheets dampen retreat.

These differences in ice response between experiments are evident during the period of moderate high-latitude summer insolation. While both sticky and slippery-bed ice sheets retreat during this period, the slippery-bed ice sheets begin to retreat 2.5 kyr earlier (25 kyr versus 27.5 kyr) and more rapidly (Figure 4.1). By the time summer insolation decreases sufficiently to allow ice re-advance, the slippery-bed ice sheets have almost completely vanished with 90 % loss in ice-volume and 87 % loss in ice-area relative to the previous ice maximum. In contrast, sticky-bed ice sheets remain largely intact, experiencing only 55 % loss in ice-volume and 44 % loss in ice-area relative to the previous ice maximum. Complete retreat of the sticky-bed ice sheets only occurs with the more powerful high-latitude summer insolation starting at 70 kyr.

4.4.4 Climate feedbacks

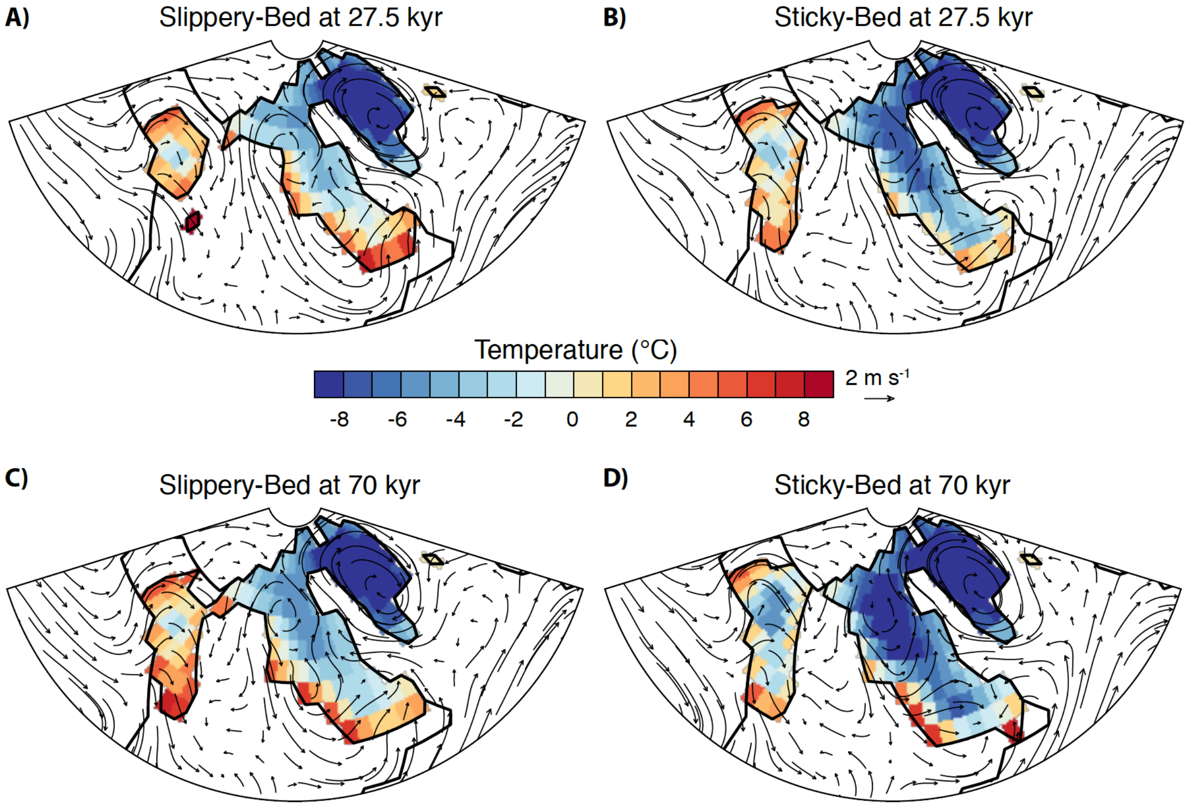

Figure 4.5: Summer surface temperature and low level winds over ice sheets
Summer (JJA) surface temperature (°C) over the ice sheets and low level winds (m s^{-1}) for the

slippery and sticky bed experiments during two local maxima in ice-volume (27.5 and 70 kyr). In general, the slippery bed ice sheets (A, C) are warmer than the sticky bed ice sheets (B, D), resulting in greater summer mass loss.

The differences in ice-volume response between basal sliding experiments result, in part, from a combination of temperature, snowfall, and albedo feedbacks. Consistent with the regolith hypothesis, the higher drag substrate produces thicker ice sheets with greater elevation and steeper slopes. For instance, at maximum extent, the surface elevation of the sticky-bed Laurentide Ice Sheet (LIS) is, on average, 365 m higher than the slippery-bed LIS. Due to the temperature lapse-rate relationship, surface temperatures above the sticky-bed sheets are colder, making them more resistant to melting during warm summer orbital configurations (Figure 4.5; Figure 4.7). June, July, and August (summer) average surface temperature over the Laurentide

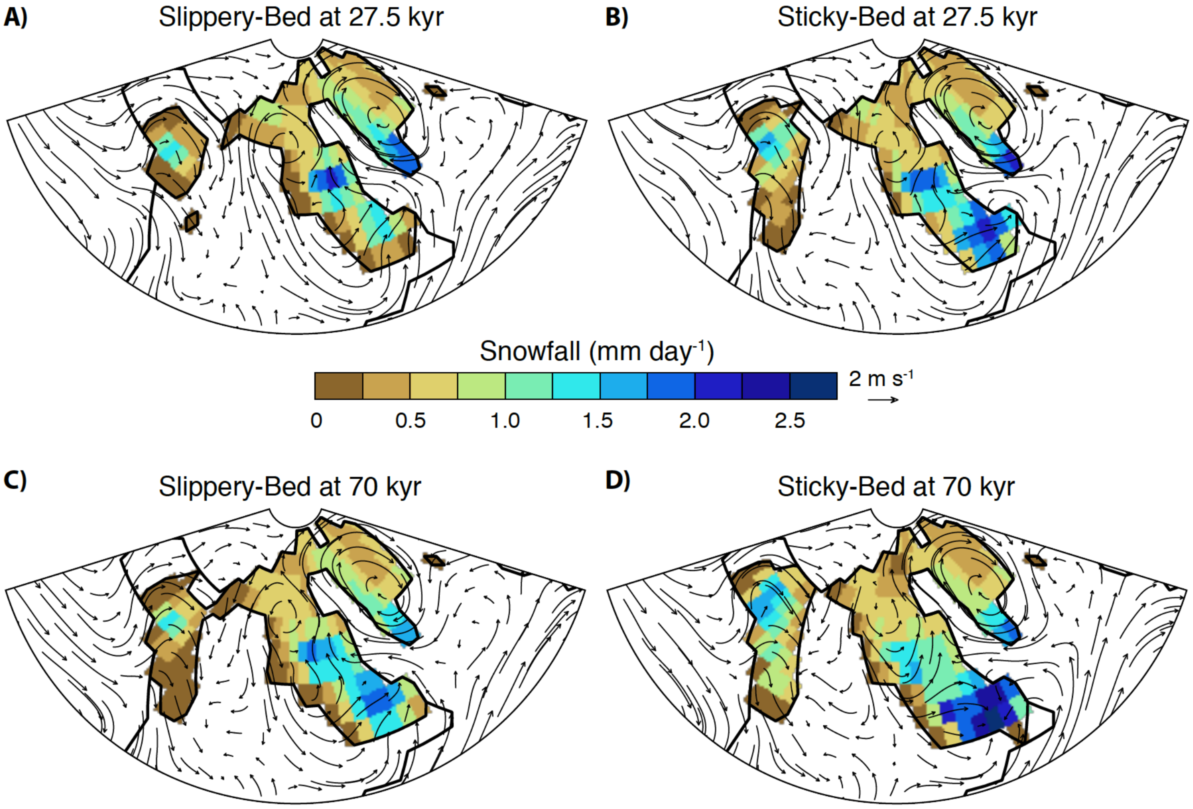

Figure 4.6: Summer snowfall and low level winds over ice sheets
Summer (JJA) snowfall (mm day^{-1}) over the ice sheets and low level winds (m s^{-1}) for the slippery and sticky bed experiments during two local maxima in ice-volume (27.5 and 70 kyr). The slippery bed ice sheets (A, C) receive less snowfall on average in the summer months than the sticky bed ice sheets (B, D), resulting in less accumulation and lower albedo.

portion of the ice sheet is 2.2 °C colder in the sticky-bed experiment than the slippery-bed experiment during initial retreat at ~27.5 kyr. Only during more significant summer warming between 70-80 kyr do both the sticky and slippery-bed ice sheets reach a similar average summer surface temperature and the sticky bed ice sheets retreat rapidly to their minimum extents. In addition, the sticky-bed ice sheets have a steeper and higher ice edge than the slippery-bed ice sheets. Therefore, with increasing summer temperature and insolation, the area of ablation expands more readily over the slippery-bed ice sheets compared to the sticky-bed ice sheets (Figure 4.4).

The sticky-bed ice sheets also tend to have greater snowfall and higher albedo than the slippery-bed ice sheets (Figure 4.6; Figure 4.7; Appendix Figure 4.3). This is a result of several feedbacks. First, less summer snowmelt occurs over the sticky-bed ice sheets than the slippery-bed ice sheets due to colder surface temperatures, leading to a higher surface albedo, since snow has a higher albedo than bare ice. This is significant because surface absorbed insolation, in addition to temperature, contributes to ice melt. Increased moisture convergence and snowfall complement the more persistent snow cover of the sticky-bed ice sheets. Here, the greater slope at the ice edge allows

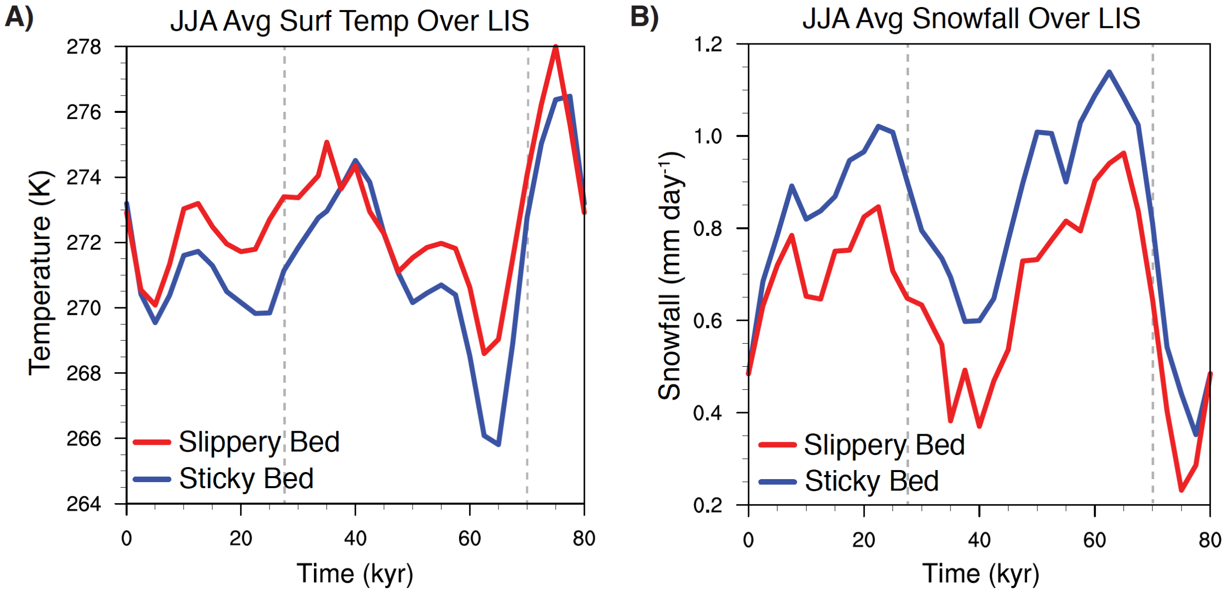

Figure 4.7: Comparison of the climate over the ice sheets through time
Plotted are average surface temperatures and snowfall over the Laurentide ice sheets for slippery and sticky beds. In general, the sticky bed LIS has a lower temperature (A) and receives more snowfall (B) than the slippery bed ice sheet LIS during the summer. Gray dashed lines mark the beginning of major ice sheet retreat.

for somewhat greater condensation and snowfall from upslope winds in the sticky-bed experiments compared to the slippery-bed experiments (Figure 4.6). This feedback acts to dampen net ablation. When ice-volume begins decreasing at 27.5 kyr, the sticky-bed LIS receives 39 % more summer snowfall on average than the slippery-bed LIS, allowing for comparatively less retreat. However, this difference in snowfall is reduced to 25 % at 70 kyr under the strong high-latitude summer warming from combined obliquity and eccentricity/precession, causing both basal configurations to experience complete melt-back.

4.5 Discussion

4.5.1 Role of CO_2

Our simulations that incorporate transient CO_2 forcing suggest that CO_2 variations are of secondary importance to basal sliding and orbital forcing in determining ice-volume cyclicity. The addition of an eccentricity-enhancing CO_2 cycle (Figure 4.1) leads to only moderate increases in maximum ice-volume amplitude of ~4 and 5 m MSLE for slippery-bed and sticky-bed experiments (Figure 4.1), and does not greatly change the spectral power of either the slippery or sticky-bed experiments with increases in the ratio of eccentricity-to-obliquity power of ~9 and ~22 %, respectively (Figure 4.3). These model responses agree with other ice sheet modeling works that find CO_2 forcing was less important than insolation forcing during the last glacial cycle (Abe-Ouchi et al., 2007) and in various CO_2 sensitivity tests (Loutre and Berger, 2000; Ganopolski and Calov, 2011; Abe-Ouchi et al., 2013). Further, our results align with a late Pliocene/early Pleistocene CO_2 record that suggests CO_2 varied with 100 kyr^{-1} frequency and 80-100 ppmv amplitude in the late Pliocene to early Pleistocene (Martínez-Botí et al., 2015) while global ice-volume varied at both 100 kyr^{-1} and 41 kyr^{-1} frequencies in the late Pliocene to early Pleistocene (Lisiecki and Raymo, 2005). These differences in cyclicity imply that the 41 kyr glacial cycles of the early Pleistocene proceeded despite predominately 100 kyr cycles of CO_2 forcing, which our slippery-bed simulations support. Given the coarse temporal resolution of the Martínez-Botí et al. (2015) CO_2 record and its limited overlap with the “41 kyr world” (Lisiecki & Raymo, 2007), we await additional CO_2 reconstructions to confirm this finding.

A slightly larger obliquity signal is possible under the potentially higher CO_2 of the early Pleistocene because the longer melt season of a warmer climate both enhances the seasonal cancellation effect from precession forcing and melt from obliquity forcing (Huybers and Tziperman, 2008). However, our experiments capture the dominant obliquity signal of the early Pleistocene with low basal sliding values, even under relatively low and eccentricity-amplifying transient CO_2 forcing. Given the small changes in ice sheet response to large, transient CO_2 forcing, our results do not support the notion that a ~30 ppmv reduction in glacial CO_2 across the mid-Pleistocene transition (Hönisch et al., 2009) dramatically changed the ice-volume response to orbital forcing.

We note that our prescribed transient CO_2 represents a simplification of reconstructed CO_2 forcing from the last few glacial cycles (e.g. Landais et al., 2013; Marcott et al., 2014). In contrast with proxy records, our peak CO_2 concentration occurs 5 kyr later than peak insolation and aligns with our ice-volume cycles. Given the lesser impact of CO_2 forcing compared to orbital forcing in our ice sheet response, we do not believe a few thousand year shift in the timing of our CO_2 forcing will significantly change our results. A slightly earlier peak in CO_2 forcing would likely accelerate ice sheet retreat to its minimum extent, but not significantly change the ice-volume spectral power of the response. Still, this topic requires additional study.

4.5.2 Model/Proxy Discrepancies

As shown, the LR04 $\delta^{18}O$ record of the late Pleistocene shows a dominant spectral peak at ~100 kyr^{-1} frequency (Lisiecki and Raymo, 2005) (Figure 4.3). However, analysis of individual glacial cycles from the LR04 $\delta^{18}O$ record highlights significant temporal variability in ice-volume spectral power at the frequencies of obliquity, precession, and eccentricity (e.g. Lisiecki and Raymo, 2007). In addition, $\delta^{18}O$ values from foraminifera are a function of both seawater temperature and $\delta^{18}O$ of local water, which is dependent on $\delta^{18}O$ of the water source region and ice-volume. The relative partitioning of the benthic foraminifera $\delta^{18}O$ signal between deep-water temperature and ice-volume fluctuated through the Pleistocene (e.g. Bintanja and van de Wal, 2008; Elderfield et al., 2012; Rohling et al., 2014, Shakun et al., 2015). For instance, temperature and $\delta^{18}O$ reconstructions from a record in the South Pacific show that late Pleistocene deep-sea temperature varied mainly at 100 kyr^{-1} frequency while $\delta^{18}O$ varied significantly at both 100 and 41 kyr^{-1} frequencies (Elderfield et al., 2012) (Appendix Figure 4.4). Although not necessarily representative of the global signal, this example illustrates that the ice-volume cycles of the late Pleistocene behave differently than the deep ocean temperature cycles and might help reduce the discrepancy between our simulated late Pleistocene ice-volume signal and the LR04 $\delta^{18}O$ record.

The strength of the obliquity ice-volume signal in our sticky-bed simulations might be related to the relatively small size of our simulated ice sheets, which do not reach the maximum extents indicated by glacial records. Obliquity cycles primarily affect high-latitude insolation while precession cycles affect insolation more uniformly over most latitudes. Therefore, summer insolation variability in the ablation zone of an ice sheet that reaches mid-latitudes is controlled almost exclusively by precession. Likewise, high latitude vegetation and sea ice feedbacks, which amplify the obliquity ice-volume response, will be muted if the LIS ice sheet extends far enough south and west (Tabor et al., 2014). Accordingly, if our ice sheets reached further south, we might expect a greater transferal of spectral power from obliquity to eccentricity.

Some previous studies find large North American ice sheets trigger threshold responses that are important for producing the 100 kyr ice-volume cycles of the late Pleistocene by way of isostatic subsidence (Abe-Ouchi et al., 2013), dust deposition (Peltier and Marshall, 1995; Ganopolski and Calov, 2011), ice sheet calving into proglacial lakes/marine incursions (Pollard, 1982), sea-ice cover that affects moisture supply (Gildor and Tziperman, 2001), or other non-linear ice-sheet and climate-state responses (Raymo, 1997; Paillard, 1998). Here, we do not simulate dust or proglacial lakes, and ice calving occurs immediately when the ice sheets reach open ocean (see Methods). Therefore, we are unable to consider the potentially varying impact of these mechanisms with changes in ice sheet size. In our model, the isostatic response helps ice sheets retreat, but it affects both sticky and slippery-bed ice sheets. Further, it dampens the resistance of the sticky-bed ice sheets to orbital forcing and thus, reduces the strength of the eccentricity ice-volume signal. Finally, we do not find any shift in our climate state with the appearance of larger ice sheets. However, our modeled maximum ice volumes are relatively small compared to those of the Late Pleistocene. If our ice sheets grew larger, an additional mechanism might become important for triggering rapid destabilization of the ice sheets.

4.5.3 Model Comparison

Many of our results agree with the findings of Ganopolski and Calov (2011). In both studies, simulation of deformable sediment over North America produces thin, extensive ice-sheets with relatively less volume and little to no eccentricity ice-volume signal. Removal of regolith leads to thicker, more resistant ice sheets and the appearance of an eccentricity ice-volume signal in agreement with the regolith hypothesis (Clark et al., 2006). These similarities are encouraging, given the large differences in model components and configuration. Ganopolski and Calov

(2011) use CLIMBER-2, a statistical-dynamical model of intermediate complexity (Brovkin et al., 2002), with the ice sheet model SCOPOLIS (Greve, 1997) while we use the GENESIS GCM (Alder et al., 2011) with BIOME4 (Kaplan et al., 2003) and the PSU ice sheet model (Pollard and DeConto, 2012). Their configuration allows for the simulation of many long-term, transient experiments covering the last 800 kyr; our configuration allows exploration of synoptic-scale climate responses under more idealized orbital conditions. While model results agree, this study provides new insight into the climate mechanisms responsible for the change in ice-volume response due to the removal of regolith.

There are also several noteworthy differences between works. Arguably most important is the difference in ice-volume spectral response between models. In this study, a slippery-bed produces an ice-volume response with almost all of the spectral power at the frequency of obliquity (Figure 4.3) while in Ganopolski and Calov, (2011), a slippery-bed appears to produce slightly more spectral power at the frequency of precession than obliquity (see Figure 3f in Ganopolski and Calov, 2011). In contrast, Ganopolski and Calov (2011) simulate a large North American ice sheet with greatest ice-volume variability at the frequency of eccentricity under late Pleistocene conditions (see Figure 4.3 in Ganopolski and Calov, 2011). Here, the eccentricity ice-volume signal strengthens, but is less pronounced relative to Ganopolski and Calov (2011), when we increase basal drag (Figure 4.3). These differences in ice-volume response likely stem, in large part, from differences in the climate forcing between studies and inclusion of a powerful dust feedback in Ganopolski and Calov (2011).

4.5.4 Limitations and Justifications

Our model configuration is the most complex yet to explore removal of regolith as a mechanism for the MPT. However, there remain several limitations to our model configuration. In our model, ice sheets calve immediately upon reaching the ocean, preventing ice buttressing (e.g. Gagliardini et al., 2010), and might be partly responsible for our relatively small ice-volume cycle amplitudes. Further, the model does not simulate ice sheet instability due to retreat over retrograde bedding for marine-based portions (Schoof, 2007a). We note, however, that retreat of the LIS occurs from the western and southern edges and therefore, omission of retrograde instability is unlikely to significantly alter the simulated retreat.

Previous proxy (e.g. Lisiecki et al., 2008) and model (e.g. Tuenter et al., 2005) based studies find evidence for different ocean overturning responses to changes in obliquity and precession.

Unfortunately, computational limits prevent implementation of a dynamic ocean here. Our slab ocean calculates ocean heat transport through linear diffusion based on the local temperature gradient and a latitude-dependent diffusion coefficient (Thompson and Pollard, 1995a), which does not strictly prescribe heat transport unlike many slab ocean models. While this gives us confidence that the model captures the basic ocean responses to orbital change, we cannot comment on the role of changes in ocean overturning; we leave these topics to future investigation.

Due to computational limitations, our experimental design only applies a single orbital configuration. The possibility exists for different orbital configurations to change the ice-volume spectral power distribution, especially given our choice of a large amplitude eccentricity cycle. While our previous research shows little variability in ice-volume magnitude and spectral power under different combinations of large amplitude obliquity and precession/eccentricity forcing (Tabor et al, 2015), those experiments did not vary eccentricity. Through observations and model sensitivity tests, studies find that eccentricity modulation of precession forcing contributes significantly to the 100 kyr ice-volume signal (e.g. Raymo, 1997; Ganopolski and Calov, 2011; Abe-Ouchi et al., 2013). Therefore, the relative timing of obliquity, precession, and eccentricity might affect our ice-volume signal strength. Still, we suspect that the roughly every 100 kyr peak in high-latitude summer insolation due to the eccentricity modulation of precession should produce a saw-tooth ice-volume cycle characteristic of the late Pleistocene as long as the ice sheets are thick enough to resist collapse from moderate high-latitude summer insolation maxima.

Asynchronous coupling between the GCM and ice sheet models can potentially alter positive ice-climate feedbacks such as circulation and ice-albedo (Herrington and Poulsen, 2012). While we do not find large discontinuities in ice-area between iterations and use an asynchronous coupling period known to accurately capture the ice-volume response to climate forcing (Pollard et al., 1990), the simulated feedbacks still might not be as large as those in a synchronously coupled system (Herrington and Poulsen, 2012). Also, our chosen orbital cycles are shorter than reality, especially that of eccentricity, and might be partly responsible for the dampened ice-volume response.

4.6 Conclusions

We use a complex Earth system model to demonstrate that removal of high-latitude Northern Hemisphere regolith can explain the initiation of 100 kyr ice-age cycles at the MPT. Experiments that simulate a regolith substrate produce North American ice sheets that mainly follow the cycles of obliquity, while experiments that simulate a crystalline bedrock substrate produce ice sheets that only completely retreat from the combined high summer insolation of obliquity and precession/eccentricity, which results in a strong ice-volume signal at the frequency of eccentricity. The difference in ice-volume cycles between bed types results from a combination of changes in ice sheet flow and climate. Simulations representing a crystalline bedrock substrate have greater average ice sheet elevation than those with a regolith substrate due to greater basal drag. These thicker ice sheets have colder surface temperatures, receive more snowfall, and have a smaller ablation zone, and therefore, require greater insolation forcing to completely retreat. Further, experiments with transient CO_2 forcing cause only minor changes in ice-volume response, suggesting that CO_2 played a secondary role in the MPT.

4.7 Acknowledgements

This research was funded by grant NSF-OCE-0902258 to C. Poulsen. We thank David Pollard and the Climate Change Research Lab at the University of Michigan for their discussion and suggestions. This manuscript was improved by the thoughtful comments of Peter Clark and two anonymous reviewers.

4.8 Appendix C

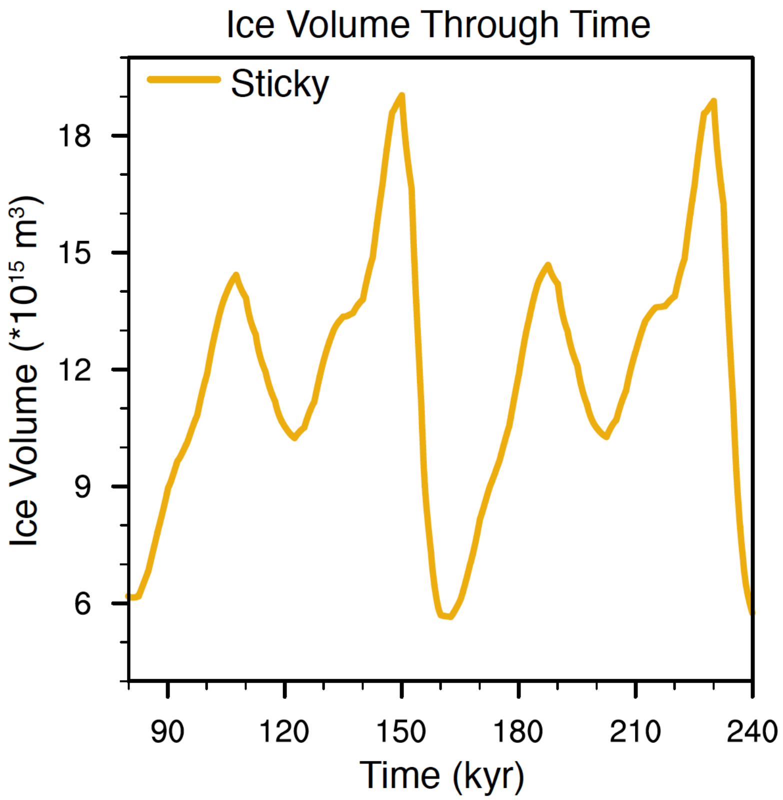

Appendix Figure 4.1: Additional orbital cycle test
Ice-volume (m^3) response to an additional orbital cycle with the sticky-bed model configuration. The ice-volume response between 80-160 kyr is nearly identical to the ice-volume response between 160-240 kyr, suggesting the ice sheets are in a cyclic equilibrium state after a spin up cycle.

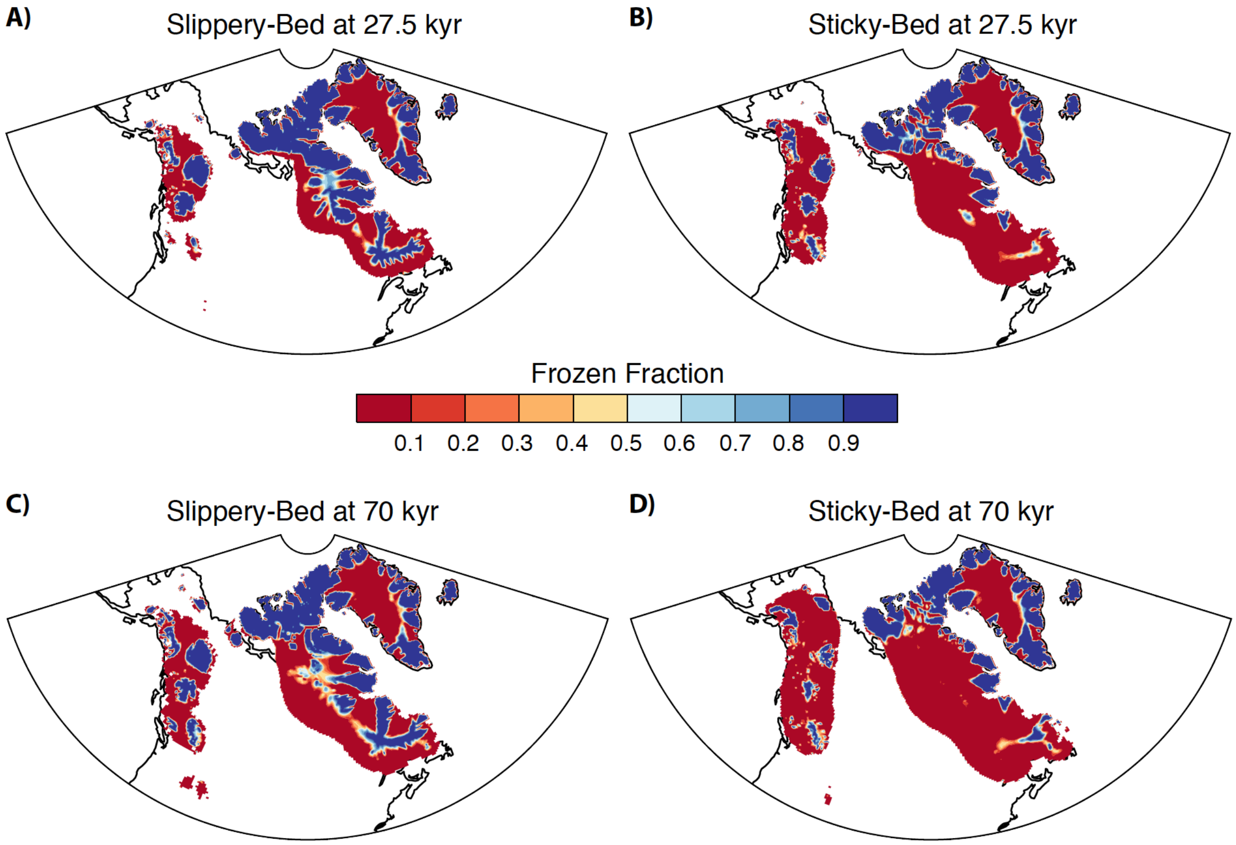

Appendix Figure 4.2: Ice bed frozen fraction during two local maxima in ice-volume
A) Areas of bed at pressure melting point of the slippery-bed experiment at 27.5 kyr. B) Areas of bed at pressure melting point of the sticky-bed experiment at 27.5 kyr. C) and D) are the same as A) and B), respectively, except at 70 kyr. The slippery-bed ice sheets (A, C) show a larger area frozen to the bed than the sticky-bed ice sheets (B, D) due to relatively less mass, which keeps the pressure melting point low. However, the areas of the slippery-bed ice sheets that are not frozen to the bed move much more rapidly than the areas of sticky-bed ice sheets at their pressure melting point.

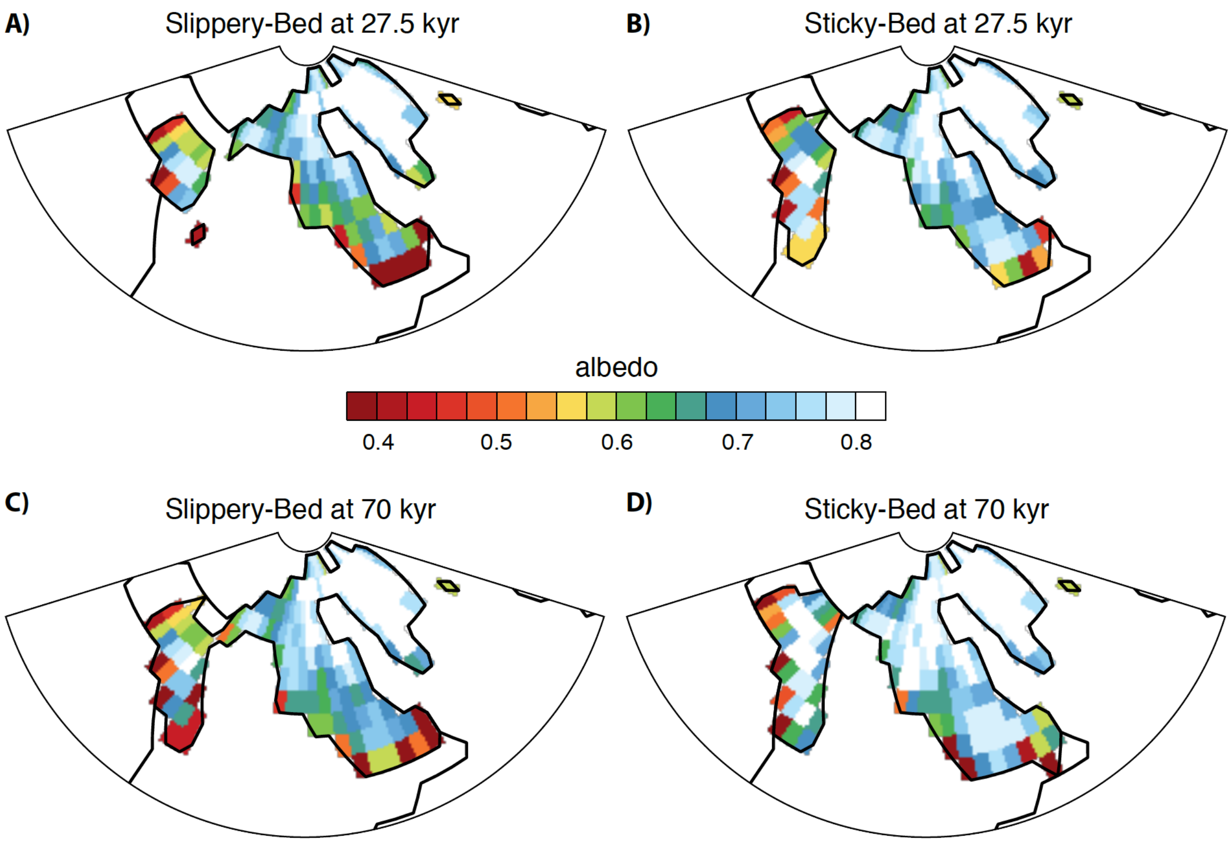

Appendix Figure 4.3: Summer surface albedo over ice sheets

Summer (JJA) surface albedo over the ice sheets for the slippery and sticky bed experiments during two local maxima in ice-volume (27.5 and 70 kyr). On average, the slippery bed ice sheets (A, C) have a lower albedo in the summer months than the sticky bed ice sheets (B, D) due to a combination of colder temperatures and greater snow cover.

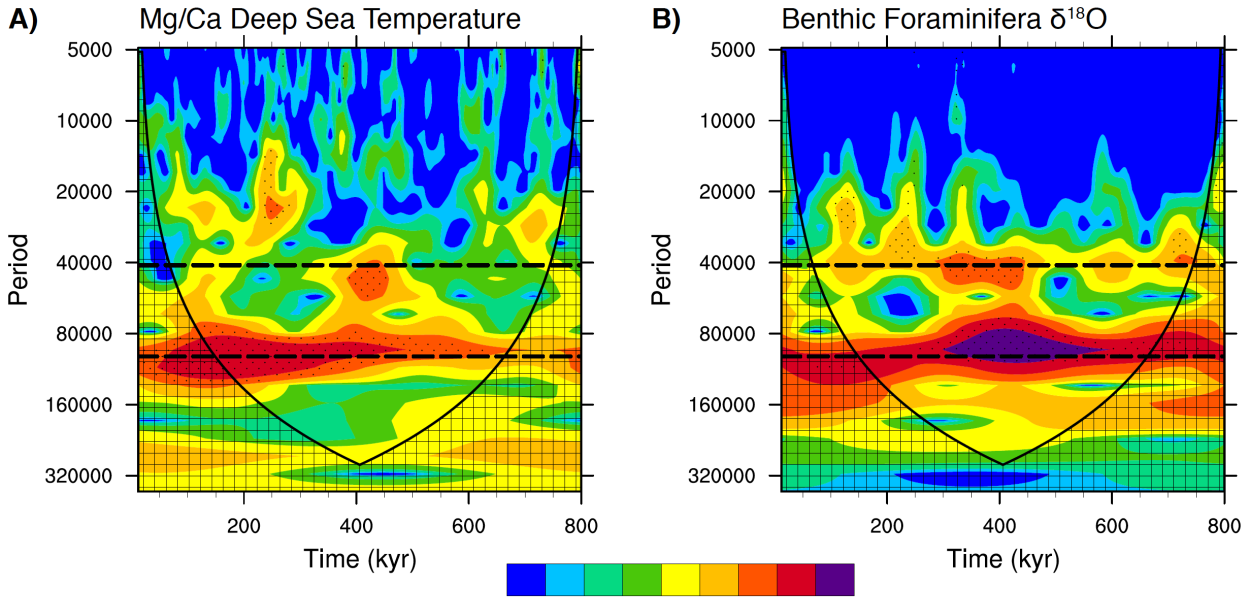

Appendix Figure 4.4: Ocean oxygen isotopic signal versus Mg/Ca temperature signal
Wavelet comparison of late Pleistocene deep-sea temperature and δ^{18}O from a single sediment core in the South Pacific (Elderfield et al., 2012). A) Wavelet analysis of standardized Mg/Ca values. The strongest signal is at the 100 kyr^{-1} frequency of eccentricity. B) Wavelet analysis of standardized δ^{18}O values. Strong, statistically significant signals are present at both 100 kyr^{-1} and 41 kyr^{-1} frequencies, indicating significant variability due to both eccentricity and obliquity. Dotted regions represent 95 % confidence and hatching represents the cone of influence.

Bibliography

Abe-Ouchi, A., Segawa, T., Saito, F., 2007. Climatic conditions for modelling the Northern Hemisphere ice sheets throughout the ice age cycle. Clim. Past 3. 423-438, doi:10.5194/cp-3-423-2007

Abe-Ouchi, A., Saito, F., Kawamura, K., Raymo, M.E., Okuno, J., Takahashi, K., Blatter, H., 2013. Insolation-driven 100,000-year glacial cycles and hysteresis of ice-sheet volume. Nature 500, 190–193. doi:10.1038/nature12374

Alder, J.R., Hostetler, S.W., Pollard, D., Schmittner, A., 2011. Evaluation of a present-day climate simulation with a new coupled atmosphere-ocean model GENMOM. Geosci. Model Dev. 4, 69-83, doi:10.5194/gmd-4-69-2011

Andrews, J.T., 1993. Changes in the silt-size and clay-size mineralogy of sediments at ocean drilling program site 645b, Baffin-Bay. Canadian J. Earth Sci. 30, 2448–2452. doi:10.1139/e93-211

Ashkenazy, Y., Tziperman, E., 2004. Are the 41kyr glacial oscillations a linear response to Milankovitch forcing? Quat. Sci. Rev.. doi:10.1016/j.quascirev.2004.04.008

Balco, G., Rovey, C.W., 2010. Absolute chronology for major Pleistocene advances of the Laurentide Ice Sheet. Geology 38, 795–798. doi:10.1130/G30946.1

Balco, G., Rovey, C.W., Stone, J., 2005. The first glacial maximum in North America. Science 307, 222–222. doi:10.1126/science.1103406

Bender, M.L., 2002. Orbital tuning chronology for the Vostok climate record supported by trapped gas composition. Earth Planet. Sci. Lett. 204, 275–289. doi:10.1016/S0012-821X(02)00980-9

Berger, A., Li, X.S., Loutre, M.F., 1999. Modelling northern hemisphere ice volume over the last 3 Ma. Quat. Sci. Rev. 18, 1–11.

Berger, A., Loutre, M.F., 1991. Insolation values for the climate of the last 10 million years. Quat. Sci. Rev. 10, 297–317. doi:10.1016/0277-3791(91)90033-Q

Bintanja, R., van de Wal, R.S.W., 2008. North American ice-sheet dynamics and the onset of 100,000-year glacial cycles. Nature 454, 869–872. doi:doi:10.1038/nature07158

Boellstorff, J. D., 1978. North American Pleistocene Stages Reconsidered in Light of Probable Pliocene-Pleistocene Continental Glaciation. Science 202(0):4.

Brovkin, V., Bendtsen, J., Claussen, M., 2002. Carbon cycle, vegetation, and climate dynamics in the Holocene: Experiments with the CLIMBER-2 model. Glob. Planet. Change. doi:10.1029/2001GB001662

Clark, P.U., Alley, R., Pollard, D., 1999. Northern Hemisphere ice-sheet influences on global climate change. Science 286, 1104–1111. doi:10.1126/science.286.5442.1104

Clark, P.U., Archer, D., Pollard, D., Blum, J.D., Rial, J.A., Brovkin, V., Mix, A.C., Pisias, N.G., Roy, M., 2006. The middle Pleistocene transition: characteristics, mechanisms, and implications for long-term changes in atmospheric pCO_2. Quat. Sci. Rev. 25, 3150–3184. doi:10.1016/j.quascirev.2006.07.008

Clark, P.U., Pollard, D., 1998. Origin of the middle Pleistocene transition by ice sheet erosion of regolith. Paleoceanography 13, 1–9. doi:10.1029/97PA02660

Elderfield, H., Ferretti, P., Greaves, M., Crowhurst, S., McCave, I.N., Hodell, D., Piotrowski, A.M., 2012. Evolution of Ocean Temperature and Ice Volume Through the Mid-Pleistocene Climate Transition. Science 337, 704–709. doi:10.1126/science.1221294

Farrell, J.W., Clemens, S.C., Gromet, L.P., 1995. Improved Chronostratigraphic Reference Curve of Late Neogene Seawater Sr-87/Sr-86. Geology 23, 403–406.

Gagliardini, O., Durand, G., Zwinger, T., Hindmarsh, R.C.A., Le Meur, E., 2010. Coupling of ice-shelf melting and buttressing is a key process in ice-sheets dynamics. Geophys.Res. Lett. 37. doi:10.1029/2010GL043334

Ganopolski, A., Calov, R., 2011. The role of orbital forcing, carbon dioxide and regolith in 100 kyr glacial cycles. Clim. Past 7, 1415–1425. doi:10.5194/cp-7-1415-2011

Gildor, H., Tziperman, E., 2001. A sea ice climate switch mechanism for the 100 kyr glacial cycles. J. Geophys. Res. 106, 9117-9133. doi: 10.1029/1999JC000120

Greve, R., 1997. A continuum mechanical formulation for shallow polythermal ice sheets, Philos. T. R. Soc. Lon. A, 355, 921–974.

Herrington, A.R., Poulsen, C.J., 2012. Terminating the Last Interglacial: The Role of Ice Sheet–Climate Feedbacks in a GCM Asynchronously Coupled to an Ice Sheet Model. J.of Clim. 25, 1871–1882. doi:10.1175/JCLI-D-11-00218.1

Hönisch, B., Hemming, N.G., Archer, D., Siddall, M., McManus, J.F., 2009. Atmospheric Carbon Dioxide Concentration Across the Mid-Pleistocene Transition. Science 324, 1551–1554. doi:10.1126/science.1171477

Horton, D.E., Poulsen, C.J., Pollard, D., 2010. Influence of high-latitude vegetation feedbacks on late Palaeozoic glacial cycles. Nat. Geosci. 3, 572–577. doi:10.1038/ngeo922

Huybers, P., 2007. Glacial variability over the last two million years: an extended depth-derived agemodel, continuous obliquity pacing, and the Pleistocene progression. Quat. Sci.Rev. 26, 37–55. doi:10.1016/j.quascirev.2006.07.013

Huybers, P., Tziperman, E., 2008. Integrated summer insolation forcing and 40,000-year glacial cycles: The perspective from an ice-sheet/energy-balance model. Paleoceanography 23. doi:10.1029/2007PA001463

Joussaume, S., Braconnot, P., 1997. Sensitivity of paleoclimate simulation results to season definitions. J. Geophys. Res. 102, 1943. doi:10.1029/96JD01989

Joyce, J.E., Tjaisma, L.R.C., Prutzman, J.M., 1993. North American glacial meltwater history for the past 2.3 m.y.: Oxygen isotope evidence from the Gulf of Mexico. Geology 21, 483. doi:10.1130/0091-7613(1993)021<0483:NAGMHF>2.3.CO;2

Kaplan, J.O., Bigelow, N.H., Prentice, I.C., Harrison, S.P., Bartlein, P.J., Christensen, T.R., Cramer, W., Matveyeva, N.V., McGuire, A.D., Murray, D.F., Razzhivin, V.Y., Smith, B., Walker, D.A., Anderson, P.M., Andreev, A.A., Brubaker, L.B., Edwards, M.E., Lozhkin, A.V., 2003. Climate change and Arctic ecosystems: 2. Modeling, paleodata-model comparisons, and future projections. J. Geophys. Res.Atm. 108. doi:10.1029/2002JD002559

Landais, A., Dreyfus, G., Capron, E., Jouzel, J., 2013. Two-phase change in CO_2, Antarctic temperature and global climate during Termination II. Nature. doi:10.1038/ngeo1985

Lawrence, K.T., Sosdian, S., White, H.E., Rosenthal, Y., 2010. North Atlantic climate evolution through the Plio-Pleistocene climate transitions. Earth Planet. Sci. Lett. 300, 329–342. doi:10.1016/j.epsl.2010.10.013

Lisiecki, L.E., 2014. Atlantic overturning responses to obliquity and precession over the last 3 Myr. Paleoceanography 29, 71–86. doi:10.1002/2013PA002505

Lisiecki, L.E., Raymo, M.E., 2005. A Pliocene-Pleistocene stack of 57 globally distributed benthic delta O-18 records. Paleoceanography 20. doi:10.1029/2004PA001071

Lisiecki, L.E., Raymo, M.E., 2007. Plio–Pleistocene climate evolution: trends and transitions in glacial cycle dynamics. Quat. Sci. Rev. 26, 56–69. doi:10.1016/j.quascirev.2006.09.005

Lisiecki, L.E., Raymo, M.E., Curry, W.B., 2008. Atlantic overturning responses to Late Pleistocene climate forcings. Nature. doi:10.1038/nature07425

Loutre, M.F., Berger, A., 2000. No glacial-interglacial cycle in the ice volume simulated under constant astronomical forcing and variable CO_2. Geophys. Res. Lett. 27, 783-786. doi: 10.1029/1999GL006081

Marcott, S.A., Bauska, T.K., Buizert, C., Steig, E.J., Rosen, J.L., 2014. Centennial-scale changes in the global carbon cycle during the last deglaciation. Nature. doi:10.1038/nature13799

Marshall, S.J., Clarke, G., 1999. Modeling North American freshwater runoff through the last glacial cycle. Quat. Res. 52, 300–315. doi:10.1006/qres.1999.2079

Martínez-Botí, M.A., Foster, G.L., Chalk, T.B., Rohling, E.J., Sexton, P.F., Lunt, D.J., Pancost, R.D., Badger, M.P.S., Schmidt, D.N., 2015. Plio-Pleistocene climate sensitivity evaluated using high-resolution CO2 records. Nature 518, 49–54. doi:doi:10.1038/nature14145

Paillard, D., 1998. The timing of Pleistocene glaciations from a simple multiple-state climate model. Nature 391, 378–381.

Peltier, W.R., 2004. Global glacial isostasy and the surface of the ice-age earth: The ICE-5G (VM2) model and GRACE. Ann. Rev. of Earth Planet. Sci. 32, 111–149. doi:10.1146/annurev.earth.32.082503.144359

Peltier, W.R., Marshall, S.J., 1995. Coupled energy-balance/ice-sheet model simulations of the glacial cycle: a possible connection between terminations and terrigenous dust. J. Geophys. Res 100. doi: 10.1029/95JD00015. issn: 0148-0227.

Pena, L.D., Goldstein, S.L., 2014. Thermohaline circulation crisis and impacts during the mid-Pleistocene transition. Science 345, 318–322. doi:10.1126/science.1249770

Petit, J.R., Jouzel, J., Raynaud, D., Barkov, N.I., Barnola, J.M., Basile, I., Bender, M., Chappellaz, J., Davis, M., Delaygue, G., Delmotte, M., Kotlyakov, V.M., Legrand, M., Lipenkov, V.Y., Lorius, C., PÉpin, L., Ritz, C., Saltzman, E., Stievenard, M., 1999. Climate and atmospheric history of the past 420,000 years from the Vostok ice core, Antarctica. Nature 399, 429–436. doi:10.1038/20859

Peucker-Ehrenbrink, B., Blum, J.D., 1998. Re-Os isotope systematics and weathering of Precambrian crustal rocks: Implications for the marine osmium isotope record. Geochim. Et

Cosmochim. Acta 62, 3193–3203. doi:10.1016/S0016-7037(98)00227-0

Pisias, N.G., Moore Jr., T.C., 1981. The evolution of the Pleistocene climate: a time series approach. Earth Planet. Sci. Lett. 52, 450–458.

Pollard, D., 1980. A simple parameterization for ice sheet ablation rate. Tellus 32, 384–388. doi:10.1111/j.2153-3490.1980.tb00965.x

Pollard, D., 1982. A Simple Ice Sheet Model Yields Realistic 100 kyr Glacial Cycles. Nature 296, 334–338.

Pollard, D., DeConto, R.M., 2012a. Description of a hybrid ice sheet-shelf model, and application to Antarctica. Geosci. Model Dev. 5, 1273–1295. doi:10.5194/gmd-5-1273-2012

Pollard, D., DeConto, R.M., 2012b. A simple inverse method for the distribution of basal sliding coefficients under ice sheets, applied to Antarctica. The Cryosphere 6, 953–971. doi:10.5194/tc-6-953-2012

Pollard, D., Muszynski, I., Schneider, S.H., Thompson, S.L., 1990. Asynchronous coupling of ice sheet and atmospheric forcing models. Annals of Glaciol.14, 247-251.

Raymo, M.E., 1997. The timing of major climate terminations. Paleoceanography 12, 577–585.

Raymo, M.E., Oppo, D.W., Flower, B.P., Hodell, D.A., 2004. Stability of North Atlantic water masses in face of pronounced climate variability during the Pleistocene. Paleoceanography 19, PA2008 doi:10.1029/2003PA000921

Refsnider, K.A., Miller, G.H., 2013. Ice-sheet erosion and the stripping of Tertiary regolith from Baffin Island, eastern Canadian Arctic. Quat. Sci. Rev. 67, 176–189. doi:10.1016/j.quascirev.2013.01.010

Rial, J.A., Oh, J., Reischmann, E., 2013. Synchronization of the climate system to eccentricity forcing and the 100,000-year problem. Nat. Geosci. 6, 289–293. doi:10.1038/NGEO1756

Robinson, A., Calov, R., Ganopolski, A., 2010. An efficient regional energy-moisture balance model for simulation of the Greenland Ice Sheet response to climate change. Cryosphere 4, 129–144. doi:10.5194/tc-4-129-2010

Rohling, E.J., Foster, G.L., Grant, K.M., Marino, G., Roberts, A.P., Tamisiea, M.E., Williams, F., 2014. Sea-level and deep-sea-temperature variability over the past 5.3 million years. Nature 508, 477. doi:10.1038/nature13230

Roy, M., Clark, P.U., Raisbeck, G.M., Yiou, F., 2004. Geochemical constraints on the regolith hypothesis for the middle Pleistocene transition. Earth Planet. Sci. Lett. 227, 281-296. doi:10.1016/j.epsl.2004.09.001

choof, C., 2007. Ice sheet grounding line dynamics: Steady states, stability, and hysteresis. J. Geophys. Res., 112, F03S28, doi:10.1029/2006JF000664.

Setterholm, D.R., Morey, G.B., 1995. An extensive pre-Cretaceous weathering profile in east-central and southwestern Minnesota. USGS Bulletin.

Shakun, J.D., Lea, D.W., Lisiecki, L.E., Raymo, M. E., 2015. An 800-kyr record of global surface ocean d18O and implications for ice volume-temperature coupling. Earth Planet. Sci. Lett. 426, 58-68. http://dx.doi.org/10.1016/j.epsl.2015.05.042

Tabor, C.R., Poulsen, C.J., Pollard, D., 2014. Mending Milankovitch's theory: obliquity amplification by surface feedbacks. Clim. Past 10, 41–50. doi:10.5194/cp-10-41-2014

Tabor, C.R., Poulsen, C.J., Pollard, D., 2015. How obliquity cycles powered early Pleistocene global ice-volume variability. Geophys. Res. Lett., 29, doi:10.1002/2015GL063322.

Thompson, S.L., Pollard, D., 1995. A Global Climate Model (GENESIS) with a Land-Surface Transfer Scheme (LSX). Part I: Present Climate Simulation. J. Clim. 8, 732–761. doi:10.1175/1520-0442(1995)008<0732:AGCMWA>2.0.CO;2

Tuenter, E., Weber, S.L., Hilgen, F.J., 2005. Sea-ice feedbacks on the climatic response to precession and obliquity forcing. Geophys. Res. Lett. 32, L24704, doi:10.1029/2005GL024122, 2005.

Tziperman, E., Gildor, H., 2003. On the mid-Pleistocene transition to 100 kyr glacial cycles and the asymmetry between glaciation and deglaciation times. Paleoceanography 18. doi:10.1029/2001PA000627

van den Berg, J., van de Wal, R., Oerlemans, H., 2008. A mass balance model for the Eurasian ice sheet for the last 120,000 years. Glob. Planet. Change 61, 194–208. doi:10.1016/j.gloplacha.2007.08.015

Chapter 5: The Contributions of Paleogeography and CO_2 to Late Cretaceous Cooling

5.1 Abstract

Proxy temperature reconstructions indicate a dramatic cooling from the Cenomanian to Maastrichtian. Yet the spatial extent of and mechanisms responsible for this cooling remain uncertain given simultaneous tectonic and greenhouse gas changes through the Late Cretaceous. Here, we compare several climate simulations using two different Earth System models with a compilation of marine proxy sea-surface temperatures from the Cenomanian and Maastrichtian to better understand Late Cretaceous climate change. Surface temperature responses are generally consistent between models and allow us to separately assess the climate effects of geography and CO_2 in the Late Cretaceous. The comparison of proxies and models confirm that Late Cretaceous cooling was a widespread phenomenon and likely due to a reduction in GHG concentrations in excess of a halving of CO_2, not changes in geography. Nevertheless, model simulations demonstrate that plate migration through the Late Cretaceous caused large regional temperature changes, which must be considered when interpreting long-term temperature trends.

5.2 Introduction

Across the Late Cretaceous (101-66 Ma), proxy temperature reconstructions suggest a cooling trend from the Cenomanian/Turonian Thermal Maximum (e.g. Huber et al., 2002; Friedrich et al., 2012; Linnert et al., 2014) to the Maastrichtian, with the possible appearance of significant polar land-ice (Miller et al., 2005). This cooling occurred in concert with large-scale tectonic changes such as restriction of the Arctic ocean and expansion of the Atlantic ocean (e.g. Sewall et al., 2007), a reduction in atmospheric CO_2 (e.g. Berner and Kothavala, 2001; Wang et al., 2014) and the radiation of angiosperms (e.g. Boyce et al., 2009), which make determining the cause of Late Cretaceous climatic change difficult. A dearth of long-term temperature records (Linnert et al., 2014) and climate simulations spanning the Late Cretaceous (Donnadieu et al., 2006) exacerbate the problem.

To investigate the mechanisms responsible for the Late Cretaceous cooling, we compare several Earth System model simulations with a compilation of marine sea-surface temperature (SST) proxy records from the Cenomanian and Maastrichtian. Model simulations allow us to separate the Late Cretaceous temperature responses due to changes in geography from responses due to reduction in CO_2. These simulations, in combination with the SST proxy compilation, provide additional insight into the extent, magnitude, and mechanisms responsible for the Late Cretaceous cooling. Although tectonic changes lead to significant regional temperature responses across the Late Cretaceous, we show that the cooling was likely a global response to a reduction in CO_2.

5.3 Methods

5.3.1 Climate simulations

Experiment	Age (Ma)	Solar Constant (Wm-2)	CO2 (ppmv)	Global MAT (°C)	EQ Temp: 5°S-5°N (°C)	N Pole Temp: 85°-90°N (°C)
CEN 4x CO2: CESM	96.4	1353.9	1120	22.80	30.76	-10.94
CEN 4x CO2: HadCM3L	96.4	1353.9	1120	22.18	31.69	-12.17
MAA 4x CO2: CESM	68.2	1357.18	1120	22.92	31.93	-9.93
MAA 4x CO2: HadCM3L	68.2	1357.18	1120	22.34	32.52	-8.00
MAA 2x CO2: CESM	68.2	1357.18	560	19.82	29.51	-23.31
MAA 2x CO2: HadCM3L	68.2	1357.18	560	19.02	29.29	-18.09

Table 5.1: Model configurations and statistics
All reported temperatures are mean annual surface temperatures.

We use the Community Earth System Model (CESM) and the Hadley Centre Model (HadCM3L) with identical paleogeographies, greenhouse gas levels (GHG), total solar irradiance (TSI), and orbital configurations. Both models contain dynamic atmosphere, ocean, sea ice, land surface, and vegetation components. Here, CESM has a 1.9x2.5° atmosphere/land-surface grid and ~1° ocean/sea-ice grid, and HadCM3L has a 2.5x3.75° grid for all model components. These models have been previously used for paleoclimate simulations (e.g. Rosenbloom et al., 2013; Lunt et al., 2010; Feng and Poulsen, 2014). Paleogeographic maps come from 0.5° Getech Plc reconstructions, based on the methods of Markwick and Valdes ((2004)), and contain both detailed topography and bathymetry. In this study, we focus on paleogeographic reconstructions of the Cenomanian (100.5-93.9 Ma) and Maastrichtian (72.1-66.0 Ma), end-member ages of the Late Cretaceous (Figure 5.1). All experiments use age appropriate TSI (Gough, 1981) with a present-day orbital configuration (Table 5.1). CO_2 concentrations are

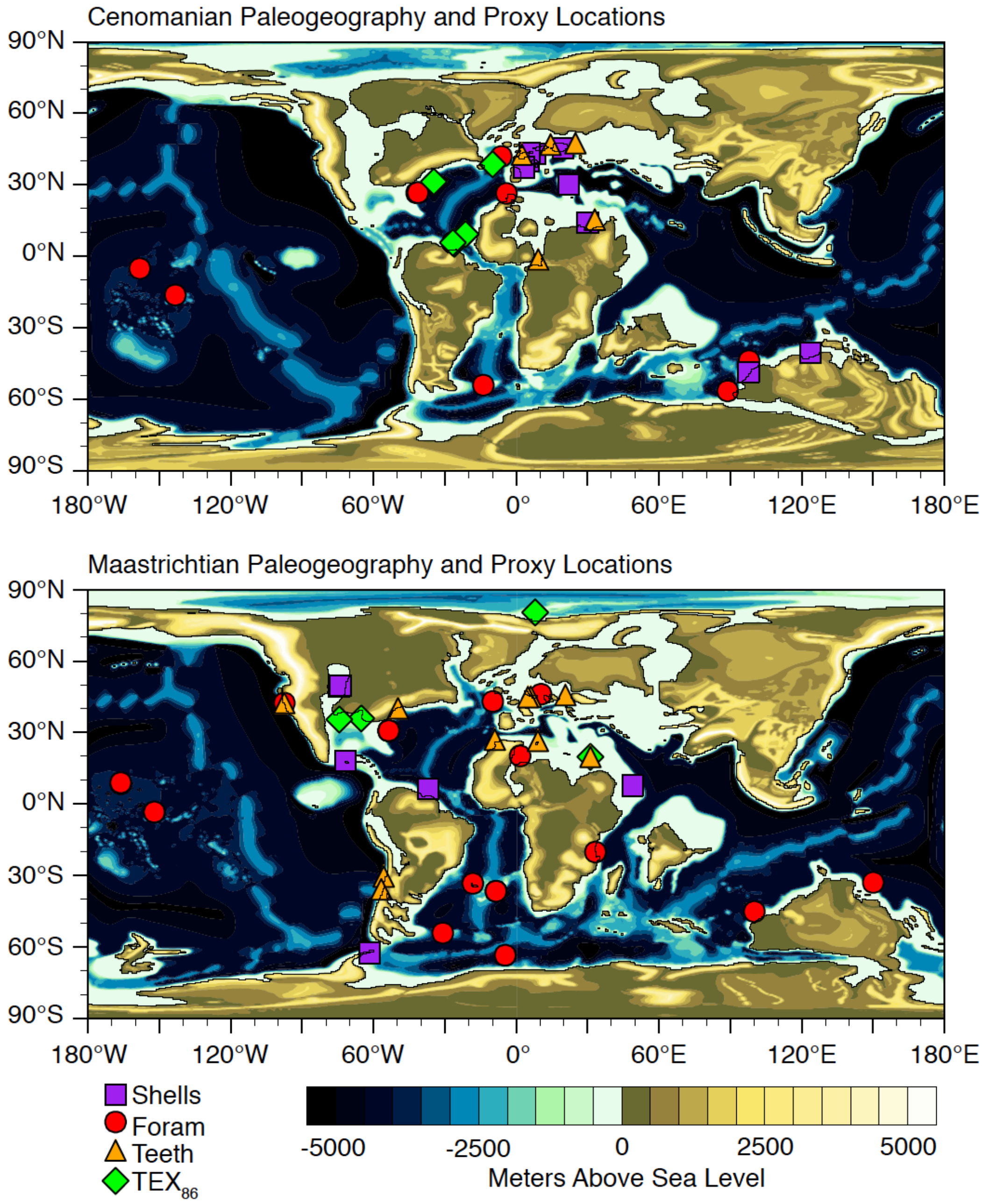

Figure 5.1: Late Cretaceous paleogeography
Getech Plc Cenomanian and Maastrichtian paleogeography with marine proxy locations.

set to either 4x or 2x preindustrial (1120 or 560 ppm), roughly representative of proxy-reconstructed averages for the mid-to-late Cretaceous (Wang et al., 2014). Here we assume modern cloud microphysical properties and atmospheric mass, though prior studies have shown these may affect the surface energy balance (Kump and Pollard, 2008; Poulsen et al., 2015).

We run all CESM simulations for 1500 years and all HadCM3L simulations for 1422 years, long enough for the upper ocean (100 m) and atmosphere to reach near-equilibrium. All results are climatologies from the final 30-years of the model runs. Below we explore three model configurations with both CESM and HadCM3L: a 4x CO_2 Cenomanian case, a 4x CO_2 Maastrichtian case, and a 2x CO_2 Maastrichtian case. See supplemental information for additional model configuration and spin-up details.

5.3.2 Proxy records

Marine SST proxy reconstructions come from a combination of planktonic foraminifera (Schönfeld et al., 1991; D'Hondt and Lindinger, 1994; Sellwood et al., 1994; Huber and Hodell, 1995; Li and Keller, 1998; Li and Keller, 1999; Norris and Wilson, 1998; Price et al., 1998; Barrera and Savin, 1999; Clarke and Jenkyns, 1999; Frank and Arthur, 1999; Pearson et al., 2001; Price and Hart, 2002; Huber et al., 2002; Norris et al., 2002; Abramovich et al., 2003; Gustafsson et al., 2003; Maestas et al., 2003; Friedrich et al., 2004; Macleod et al., 2005; Bice et al., 2006; Zakharov et al., 2006; Moriya et al., 2007; Friedrich et al., 2008; Friedrich et al., 2009; Ando et al., 2009), fish tooth enamel (Kolodny and Raab, 1988; Kolodny and Luz, 1991; Lécuyer et al., 1993; Pucéat et al., 2003; Pucéat et al., 2007; Ounis et al., 2008), shells of mollusks, bivalves, brachiopods, and belemnite rosta (Pirrie and Marshall, 1990; Ditchfield et al., 1994; Wilson and Opdyke, 1996; Carpenter et al., 2003; Voigt et al., 2003; Voigt et al., 2004; Steuber et al., 2005; Zakharov et al., 2006; El-Shazly et al., 2011; Henderson and Price, 2012; Price et al., 2012), and TEX_{86} (Schouten et al., 2003; Jenkyns et al., 2004; Forster et al., 2007a; Forster et al., 2007b; Damste et al., 2010; Alsenz et al., 2013; Vellekoop et al., 2014; Linnert et al., 2014) (**Error! Reference source not found.**). Proxy values used here represent data averages of studies from the Cenomanian and Maastrichtian based on published ages, with averaging done over the entire age and for nearby sample locations from a single study and technique. To allow for a more direct comparison, we use several standard SST calibrations that come from the works of Erez and Luz (1983) for foraminifera, Anderson and Arthur (1983) for shells, Lécuyer et al. (2013) for fish tooth enamel, and Kim et al. (2010) for TEX$_{86}$. Here, we only provide analytical and/or calibration uncertainties (Grossman and Ku, 1986; Crowley and Zachos, 2000; Kim et al., 2010; Lécuyer et al., 2013); therefore, our compilation represents a minimum estimate of proxy range over an age. To correct seawater $\delta^{18}O$ ($\delta^{18}O_{sw}$) for regional variability, we use model period-specific zonal mean salinity (Poulsen et al., 1999) (Appendix Figure 5.1) with the relationship of Broecker (1989) and assume a mean $\delta^{18}O_{sw}$ of -1‰ Vienna Mean Standard Ocean Water (VSMOW) (Shackleton and Kennett, 1975). See supplement materials for additional details on proxy data collection, averaging, and calibration.

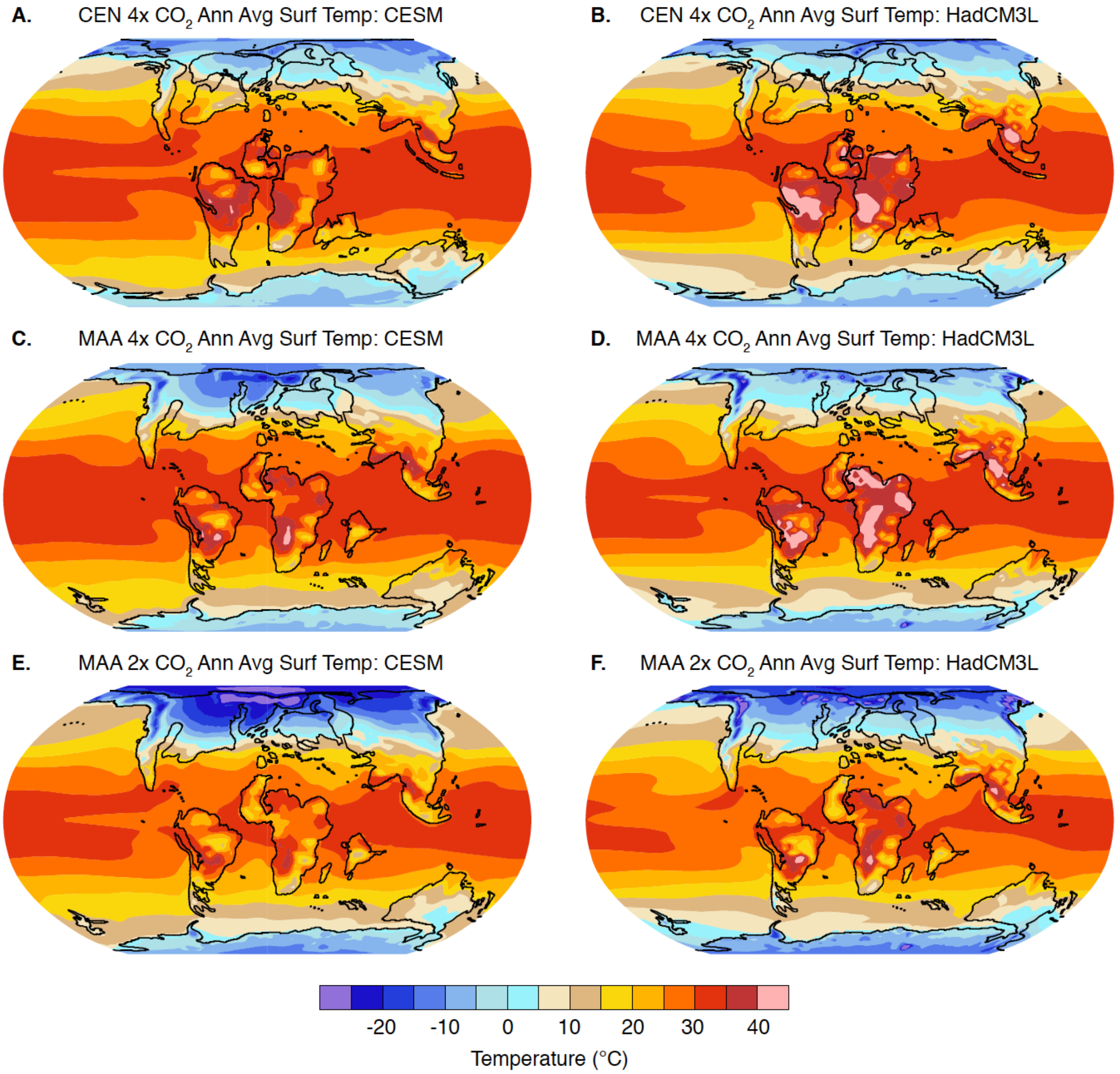

Figure 5.2: Late Cretaceous mean annual surface temperatures
Comparison of CESM and HadCM3L outputs highlight the similarities in surface temperature patterns over most of the global. Polar amplification of the global cooling response to a reduction

in CO_2 during the Maastrichtian is clearly visible in both models, particular in the Arctic.

5.4 Results

Both models produce similar global average surface temperatures (**Error! Reference source not found.**). CESM is warmer than HadCM3L by 0.67°C, mainly due to slightly higher SSTs in CESM than HadCM3L. The largest difference occurs in the high-latitudes of the South Pacific where CESM SSTs are up to 10°C warmer due to greater ocean heat transport into the region and less cloud cover (Figure 5.2, Appendix Figure 5.3). In contrast, CESM land-surface temperatures (LST) tend to be cooler than HadCM3L. Much of this difference stems from model vegetation. In mid-to-high latitudes, less dense vegetation in CESM reduces canopy masking of snow-cover and raises surface albedo (Appendix Figure 5.4). Despite these general differences, both models agree on the sign and magnitude of surface temperature change with changes in paleogeography and CO_2, particularly in the low to mid-latitudes where proxy density is greatest (Figure 5.2, Appendix Figure 5.2).

5.4.1 Response to paleogeography

In contrast to a previous Cretaceous modeling study on the role of paleogeography (Donnadieu et al., 2006), we do not find a large global surface temperature response in either model considered here. In fact, changes in geography and TSI from the Cenomanian to Maastrichtian lead to only 0.14°C of warming, almost completely in response to a 3.28 Wm^{-2} increase in solar constant across the Late Cretaceous (Appendix Figure 5.2). This is mirrored by minimal changes in global average emissivity (0.065°C), albedo (-0.100°C), and heat transport (0.094°C) with no change greater than 0.2°C for either model based our energy balance calculations. Further, emissivity and albedo responses disagree between models. Nevertheless, robust regional temperature changes exist. For instance, the North Pacific warms in both models due to a reduction in low-level clouds (Appendix Figure 5.3) and the closure of the Bering Strait, which allows less mixing with cold Arctic water (Poulsen and Zhou, 2013). Eastern North America, however, experiences widespread cooling, in places greater than 10°C, with the closure of the climate moderating Western Interior Seaway in the latest Cretaceous (Poulsen et al., 1999) (Figure 5.2). Restriction of the Drake Passage also leads to cooling by reducing the amount of warm Pacific water flowing through the Southern Ocean, while Australia warms as it detaches from Antarctica allowing flow along its southern margin. Finally, the equatorial Pacific warms due to a decline in upwelling and evaporation as the future Southeast Asian archipelago extends further south, reducing the fetch of Easterlies and weakening the strength of the Walker circulation (Poulsen et al., 1998).

5.4.2 Response to atmospheric ρCO_2

The model response to a decrease in CO_2 is greater than that due to changes in paleogeography (Appendix Figure 5.2). Reducing Maastrichtian CO_2 by a factor of 2 leads to an average cooling of 3.1 °C and 3.3 °C in CESM and HadCM3L, respectively. Based on our energy balance calculations, an increase in infrared emissivity is the greatest driver of cooling, and causes about ~2.5°C of the decrease in global surface temperature. Albedo feedbacks amplify the global cooling by ~0.76°C while heat transport provides a small amount of warming due to the larger equator-to-pole temperature gradient, contributing 0.07°C.

Polar amplification occurs in both models with decreasing CO_2, but it is also the primary source of discrepancy between simulated temperature responses (**Error! Reference source not found.**). CESM exhibits larger Arctic sea ice and water vapor feedbacks than HadCM3L (Appendix Figure 5.2, Appendix Figure 5.5). In CESM, the increase in sea ice cover leads to less evaporation from the ocean and less trapped longwave radiation, while reflected shortwave radiation remains high due to high cloud and sea-ice albedos. Greenland also becomes significantly colder in CESM, as vegetation is replaced by bare ground and snow cover increases. These responses are not as pronounced in HadCM3L because neither Arctic sea ice nor vegetation change as significantly. Further, HadCM3L maintains a similar Artic cloud cover, which reduces the emissivity feedback. The responses in Antarctica are somewhat distinct. Here, drier conditions also reduce cloud cover in CESM, but this acts to reduce the albedo and dampen polar amplification. Like in the Arctic, HadCM3L cloud-cover decreases relatively less in Antarctica, leading to only small albedo amplification from greater snow-cover. Overall, the model responses to CO_2 reduction in the Maastrichtian are not uniform, but almost the entire globe experiences some amount of cooling and the large-scale responses are consistent between models.

5.5 Discussion

5.5.1 Proxy comparison

Our compilation of marine SST proxy records suggest widespread cooling from the

Cenomanian to Maastrichtian, with general agreement between different proxies in the amount of cooling (**Figure 5.3**). With the current dataset, we find no compelling evidence for a significant increase in low-to-mid latitude SST gradients from the Cenomanian to the Maastrichtian, as might be anticipated from global cooling. In fact, SST proxy gradients are steeper in the Cenomanian than the Maastrichtian. The temperature gradient increases even more if we remove planktonic foraminifera reconstructions, under the justification that they are cold biased due to diagenetic alteration (Pearson et al., 2001). Furthermore, all proxy-based latitudinal SST gradients that do not include foraminifera are steeper than our model results (**Appendix Figure 5.6**, **Appendix Figure 5.7**, **Appendix Figure 5.8**). Even though the cool tropical SST

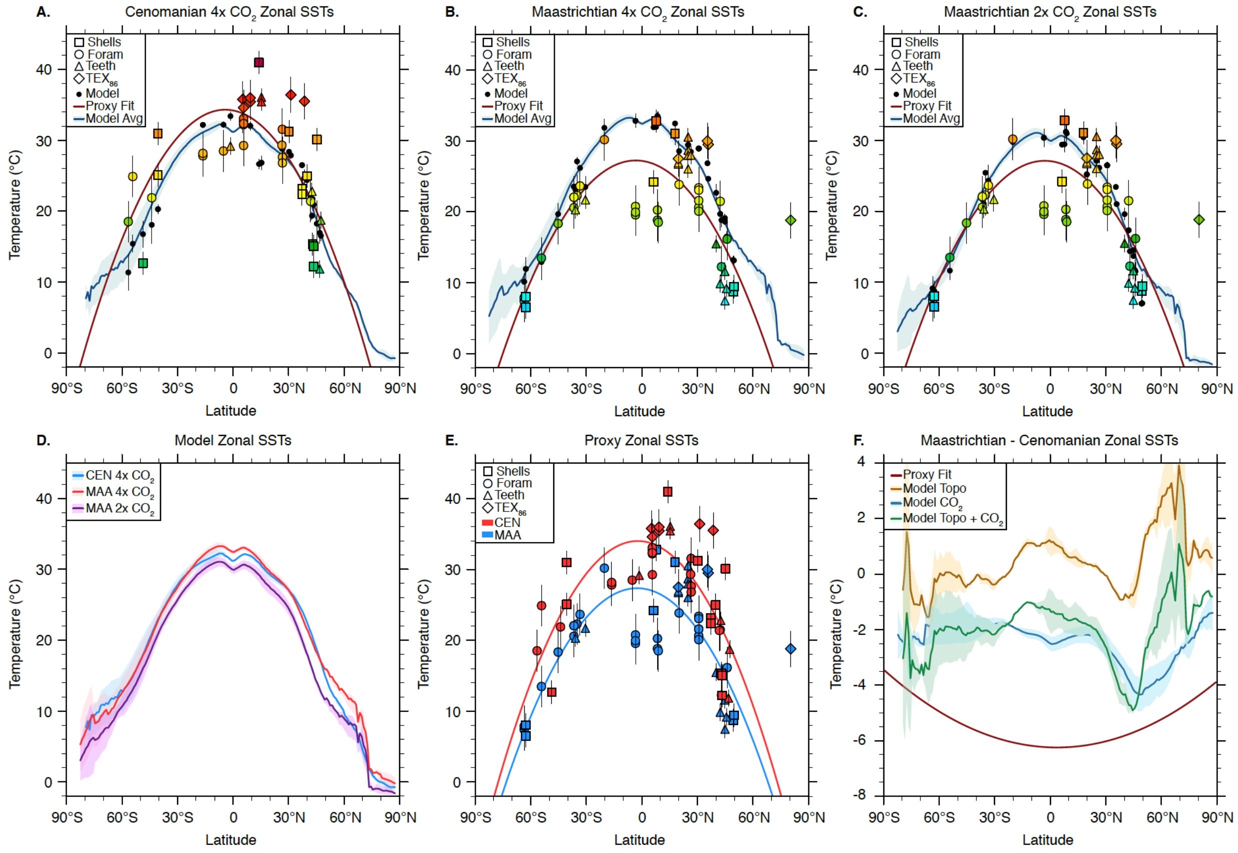

Figure 5.3: Zonal average SSTs from proxies and models

Proxy data and model zonal mean SSTs for the A) 4x CO_2 Cenomanian, B) 4x CO_2 Maastrichtian, and C) 2x CO_2 Maastrichtian. D) Zonal mean SSTs of all model simulations. E) All proxy data and parabolic fits colored by age. F) Differences in model SSTs due changes in paleogeography, reduction in CO_2, and both, as well as the difference in parabolic fits between SST proxy reconstructions from the Cenomanian and Maastrichtian. In all figures: simulated SSTs are from 2.5-m depth, line shadings represents range of model mean SSTs, vertical lines over proxy data represent method uncertainty, black dots are model SST values of proxy locations and overlaid vertical lines are model range, and maroon lines show parabolic best fits of the proxy data. See supplement information for details on data collection, parabolic fitting, and proxy uncertainty.

values from planktonic foraminifera hint at post-depositional alteration, the magnitude of cooling from the Cenomanian to Maastrichtian is on par with other reconstruction methods. This suggests a similar cooling of surface and deep-water temperatures, and is reflected in the Late Cretaceous benthic foraminifera compilation of Friedrich et al. (2012). Regardless of the proxy methods included, SST gradients imply at least seasonal Arctic sea-ice throughout the Late Cretaceous, in agreement with our model results and sea-ice proxy studies (Davies et al., 2009; Bowman et al., 2013).

5.5.2 Amount of Cooling

There is sufficient data to confirm that cooling was widespread and greater than can be explained by a factor of two reduction in atmospheric CO_2 (Figure 5.3), assuming the model sensitivity of ~3°C. In the low-to-mid latitudes, where sample density is greatest, proxies show an SST cooling of almost 6°C while the models suggest a cooling of only 2-4°C from a halving of CO_2 (Figure 5.3). Therefore, a larger GHG reduction likely occurred across the Late Cretaceous than we simulate. Based on our model results, we suspect 1120 ppm CO_2 is too low for the mid-Cretaceous since many SST proxy values are greater than the model simulated values (mean SST difference of +2.27 ±5.70 (1σ) without foraminifera), particularly in the equatorial region (Appendix Figure 5.1: Model average zonal salinities). In contrast, the 560 ppm CO_2 Maastrichtian simulations match SST proxy reconstructions fairly well and only show a small warm bias (mean SST difference of -0.65 ±4.16 (1σ) without foraminifera). Greater than 1120 ppm CO_2 values during the Cenomanian are within proxy reconstruction uncertainty (Wang et al., 2014) but model simulated CO_2 sensitivity suggests that CO_2 values on the upper-end of reconstruction estimates are necessary to capture the Cenomanian warmth.

5.6 Limitations

Data scarcity limits the extent of our comparisons. High-latitude SST changes remain uncertain due to a lack of available proxy data; therefore, little can be said about the robustness of model simulated polar amplification with a reduction in CO_2. Further, the available SST proxy records are too few and spatially biased toward the Atlantic to calculate representative global average SSTs for either the Cenomanian or Maastrichtian. Proxy uncertainties are also problematic. In this study, we chose to explore only the marine realm because of known difficulties comparing LST proxies with model simulations (e.g. Spicer et al., 2008; Feng et al., 2013; Upchurch et al., 2015). In addition, there exist relatively few, and heavily localized, LST reconstructions for the Cenomanian compared to the Maastrichtian (Spicer and Herman, 2010), which may bias our comparisons.

Here, we propose CO_2 as a mechanism for global cooling based on proxy records and model responses. Other factors not considered here such as changes in cloud microphysics (Kump and Pollard, 2008; Kiehl and Shields, 2013)), methane concentrations (Beerling and Royer, 2011), or atmospheric mass (Poulsen et al., 2015) might help the models reach SST proxy estimates for the Cenomanian. In such scenarios, Maastrichtian CO_2 concentrations could be even lower. However, the uncertainties associated with alternative warming scenarios make their impacts difficult to assess.

5.7 Conclusions and outlook

SST proxy records show that the Late Cretaceous cooling was widespread. Our model results show that a reduction in GHG concentrations, not paleogeographic evolution, can explain the global cooling. Nevertheless, geographic evolution does cause substantial region climate changes that are important for interpreting proxy records. Our findings support previous proxy temperature comparisons (Linnert et al., 2014), and CO_2 proxy records (e.g. Wang et al., 2014). While SSTs agree to first order between models and proxies, LST discrepancies remain. In particular, simulated Cenomanian annual mean LSTs for Vilyui, Central Siberia are almost 20°C colder than suggested by CLAMP LST reconstructions (Spicer et al., 2008; Spicer and Herman, 2010). The continuing model/proxy disagreement in the Siberian interior might represent missing model features such as heterogeneous topography (Spicer et al., 2008), small-scale waterways (Upchurch et al., 2015), vegetation differences (e.g. Otto-Bliesner and Upchurch, 1997; Zhou et al., 2012; Hunter et al., 2013), or adjustments to cloud microphysics (Kump and Pollard, 2008; Upchurch et al., 2015). Surprisingly, we find mid-to-high latitude LST proxy reconstructions from the Late Cretaceous are often warmer than SST proxy reconstructions at similar latitude. This is at odds with present-day latitudinal temperature gradients and our current understanding of climate, and will be an area of future study.

5.8 Acknowledgements

CESM model experiments were run on NCAR's Yellowstone cluster. We thank Getech Plc for their paleogeography reconstructions and NCAR's paleoclimate working group for their model setup assistance. Ran Feng and Rich Fiorella provided help comments and discussion.

5.9 Appendix D

5.9.1 Model descriptions

CESM

We use the Community Earth System Model (CESM) version 1.2 developed by the National Center for Atmospheric Research (NCAR). Our model component-set includes the Community Atmospheric Model version 4 (CAM4), the Community Land Model version 4 with dynamic vegetation (CLM4-DGVM), the Parallel Ocean Project model version 2 (POP2), and the Community Sea Ice model version 4 (CICE4). Additional details on the model components and performance can be found in Gent et al. (2011), and information on the DGVM is documented in Levis et al. (2004). The ocean and sea ice models run on a rotated poles grid at roughly 1° resolution with 60 vertical ocean levels. The atmosphere and land-surface models run on a finite-volume grid of 1.9x2.5°, and the atmosphere has 28 vertical levels. We run CAM4 with the Bulk Aerosol Model (BAM), a prognostic aerosol model, with aerosol concentrations and types adjusted for the Cretaceous using a method similar to Heavens et al. (2012). Here, aerosol data come from pre-industrial datasets converted into hemispherically symmetric, monthly zonal average aerosols distributions masked independently to land and sea. In addition, we add the land black carbon emissions from 62.5°N/S to all latitudes further poleward to reflect the greater vegetation cover and fire potential at high latitudes during the Cretaceous (Upchurch and Otto-Bliesner, 1998). We run all simulations for 1500 years with all model components active and synchronously coupled.

HadCM3L

We also use the Hadley Centre Model (HadCM), developed by the UK Met Office. For this study, we implement HadCM3L version 4.5, which contains dynamic atmosphere, ocean, land, and sea ice components on a 2.5x3.75° grid. The ocean and atmosphere have 19 and 20 vertical levels, respectively. Description of the similar HadCM3 model is documented in Gordon et al. (Gordon et al., 2000). We couple HadCM3L with the Top-down Representation of Interactive

Foliage and Flora Including Dynamics (TRIFFID) model with the land surface scheme MOSES 2.1 to simulate dynamic vegetation (Cox, 2001). We run the HadCM3 experiments in 4 phases:

1. 50 years with 280 ppm CO_2 and bare-ground
2. 319 years of either 560 or 1120 ppm CO_2 with TRIFFID turned on
3. 53 years with the addition of prescribed lakes
4. 1000 years with barotropic ocean flow enabled to allow non-zero vertically integrated ocean flow

For additional details on HadCM3L initialization and spin-up see Lunt et al. (2015, in review).

5.9.2 Model setup

Simulations use the paleogeographic reconstructions of Getech Plc. Following model standard practices and for improved stability, we apply model specific smoothing to the topography. For both models, we adjust total TSI for the Cenomanian and Maastrichtian based on the equation of Gough (Gough, 1981). We prescribe CO_2 concentrations as either 4x (1120 ppm) or 2x preindustrial (560 ppm). All other GHG concentrations are set to preindustrial values of 790 ppb for CH_4, 275 ppb for N_2O, and no CFCs. The orbit configuration is set to present-day. Vegetation plant functional types are model defaults; we make no adjustments for the Cretaceous. All simulations run long enough for the upper ocean to reach near-equilibrium; however, the deep ocean continues to adjust. As a result, we focus only on surface conditions.

5.9.3 Energy balance calculations

We use the zonal mean energy balance decomposition method of Heinemann (2009), which was subsequently adopted and modified by Lunt et al. (2012), and Hill et al. (2014), to explore the mechanisms responsible for surface temperature change in the Late Cretaceous with changes in paleogeography and CO_2. This method assumes incoming shortwave balances with outgoing longwave and that local imbalances are due to changes heat transport, using the following relationship:

$$\frac{S_0}{4}(1-\alpha) + H = \varepsilon\sigma T^4 \ . \ (1)$$

Here, S_0 is TSI, α is albedo, H is meridional heat convergence, ε is emissivitiy, σ ($5.67*10^{-8}$ $Wm^{-2}K^{-4}$) is the Stefan-Boltzmann constant, and T is surface temperature. With the exception of σ, values in equation (1) come from zonal averages of Earth system model outputs. We can rewrite equation (1) with respect to surface temperature as:

$$T = \left(\frac{1}{\varepsilon\sigma}\left(\frac{S_0}{4}(1-\alpha)+H\right)^{0.25}\right) \equiv E(\varepsilon, \alpha, H) \ . \ (2)$$

By substituting variables from different simulations and differencing them, we can deconstruct the various contributions to the change in surface temperature. We illustrate this below:

$$\Delta T_{emm} = E(\varepsilon, \alpha, H) - E(\varepsilon', \alpha, H) \ , \ (3)$$

$$\Delta T_{alb} = E(\varepsilon, \alpha, H) - E(\varepsilon, \alpha', H) \ , \ (4)$$

$$\Delta T_{tran} = E(\varepsilon, \alpha, H) - E(\varepsilon, \alpha, H') \ , \ (5)$$

where ΔT_{emm}, ΔT_{alb}, and ΔT_{tran} are contributions from emissivity, albedo, and heat transport to surface temperature change, and primes represent the zonal averages from the simulations being compared. The combination of surface temperature changes due to emissivity, albedo, and heat transport sum to approximate the total surface temperature response:

$$\Delta T_{total} \cong \Delta T_{emm} + \Delta T_{alb} + \Delta T_{tran} \ . \ (6)$$

This technique can be used to further decompose the climate contributions to surface temperature.

5.9.4 Proxy data

As mentioned in the main text, SST proxy values represent location and age averages. Method uncertainties roughly reflect the choices of Upchurch et al. (2015) and only accounts for calibration uncertainties. We apply these uncertainties to every averaged data point. The range in values from a particular age and site are often significantly greater than the calibration uncertainties. Therefore, uncertainties represent minimum estimates.

Point locations are consistently rotated back in time from their present-day sampling locations to the Cenomanian and Maastrichtian using the plate reconstructions from Getech Plc. Occasionally, the coarse model resolutions result in marine proxy paleo-locations over land instead of water. In these situations, we select the nearest model ocean location to represent the SST value.

To create more representative latitudinal SST gradients, parabolic fits of the proxy records include an adjustment for the deviation of the SSTs from the zonal mean based on model-simulated longitudinal heterogeneity. For example, if an equatorial proxy location has a model simulated SST of 30°C and a model zonal mean equatorial SST of 35°C, then 5°C are added to the proxy value so that it is in better agreement with the zonal average. This technique assumes that model longitudinal variability is robust regardless of mean SSTs.

Seawater $\delta^{18}O$

We assume a mean $\delta^{18}O_{sw}$ of $-1^{0}/_{00}$ VSMOW, based on the assumption of an ice-free world (Shackleton and Kennett, 1975). This assumption is widely used in Cretaceous SST reconstructions (e.g. Huber et al., 2002; Friedrich et al., 2012); however, debate remains about the potential for glaciation in the Late Cretaceous (e.g. Miller et al., 2005). A significant increase in land-ice would require less cooling in the Maastrichtian from $\delta^{18}O$ records but is not considered further in this study.

$\delta^{18}O_{sw}$ has significant regional variability in both the modern and Late Cretaceous (Zhou et al., 2008). To account for this variability, we use zonal average salinity from the model outputs (Appendix Figure 5.1) with the present-day salinity/$\delta^{18}O_{sw}$ relationship of Broecker (1989). This simple linear relationship follows:

$$\delta^{18}O_w = 0.5(PSU) - 17.12 \text{ , (7)}$$

where PSU stands for positive salinity units. In our simulations, mean ocean salinity starts at 35 PSU, which is equivalent to present-day. While not perfect, we prefer this relationship to the commonly employed present-day latitudinal $\delta^{18}O_{sw}$ correction by Zachos et al. (1994), because it indirectly accounts for precipitation and evaporation, and does not make present-day assumptions about the latitudinal distribution of $\delta^{18}O_{sw}$ (Poulsen et al., 1999). Still, this technique is inferior to model experiments that include water isotope tracking (e.g. Zhou et al., 2008).

Planktonic foraminifera

We calculate SSTs from $\delta^{18}O$ measurements of planktonic foraminifera using the calibration of Erez and Luz (1983) and a conversion to VSMOW of $0.22^{0}/_{00}$ (Bemis et al., 1998). This calibration has been widely used for foraminifera temperature reconstructions and proven accurate for a wide range of temperatures. Temperatures are calculated using the polynomial:

$$T(^\circ C) = 16.998 - 4.52[\delta^{18}O_c - (\delta^{18}O_{sw} + 0.22)] + 0.028[\delta^{18}O_c - (\delta^{18}O_{sw} + 0.22)]^2 \text{ , (8)}$$

where $\delta^{18}O_c$ is the $\delta^{18}O$ of sample calcite.

Diagenetic alteration is a potential issue for foraminifera, causing them to pickup post-depositional temperature signals from the ocean floor (e.g. Pearson et al., 2001; Norris et al., 2002). It is likely that some of the foraminifera presented in this study suffer from such alteration given the sample descriptions, relatively cool tropical SSTs, and disagreement with other SST proxy values. However, given the paucity of records and uncertainty in other included proxy techniques such as TEX_{86} (e.g. Taylor et al., 2013), we opt to include all planktonic foraminifera data. For comparison, we include zonal SST reconstructions without foraminifera as well (Appendix Figure 5.6, Appendix Figure 5.7, Appendix Figure 5.8). Even though removal of foraminifera leads to warmer tropical SST reconstructions, it does not significantly change the magnitude of cooling from the Cenomanian to the Maastrichtian, which is the main focus of this study. We assign an uncertainty of ±2.9°C for planktonic foraminifera based on Holocene core-top data from Crowley and Zachos (Crowley and Zachos, 2000) and to be consistent with the work of Upchurch (2015).

Shells and others

We use the $\delta^{18}O$ to temperature conversion of Anderson and Arthur (1983) for both aragonite and calcite of shells of mollusks, bivalves, brachiopods, and belemnite rosta based on its prevalent use in the proxy source literature. The equation is:

$$T(°C) = 16.4 - 4.14(\delta^{18}O_{c/a} - \delta^{18}O_{sw}) + 0.13(\delta^{18}O_{c/a} - \delta^{18}O_{sw})^2 \text{ , (11)}$$

where $\delta^{18}O_{c/a}$ is the $\delta^{18}O$ of sample calcite or aragonite. Like foraminifera, shells are prone to alteration (Steuber et al., 1999). We include all records here for completeness. We also show comparisons with shell SST proxy reconstructions omitted (Appendix Figure 5.7, Appendix Figure 5.8). We apply an uncertainty of ±1.6 based on 1-SD of a mollusk calibration by Grossman and Ku (1986) as in Upchurch et al. (2015).

Tooth Enamel $\delta^{18}O$

Our SST proxy compilation includes phosphate $\delta^{18}O$ records from fish tooth enamel, most of which were originally compiled by Puceat et al. (Pucéat et al., 2007). These records are considered more resistant to diagenetic alteration than foraminifera or shells, and were previously used by Puceat et al. (Pucéat et al., 2007) to argue for a near-modern latitudinal SST gradient in the Cretaceous, in contrast to reconstructions from foraminifera that suggested a shallower latitudinal SST gradient (e.g. Huber et al., 2002). Recently, there have been several recalibrations of the phosphate $\delta^{18}O$ temperature relationship. Here, we use the most recent calibration by Lecuyer et al. (2013):

$$T(°C) = 117.4 - 4.5(\delta^{18}O_{PO4} - \delta^{18}O_{sw}) \text{ , (10)}$$

where $\delta^{18}O_{PO4}$ is the $\delta^{18}O$ of sample phosphate. This calibration results in SSTs that are several degrees warmer than the calibration by Puceat et al. (2007) and several degrees cooler than the recent calibration by Puceat et al. (2010). However, the magnitude of offset between calibrations remains quite similar over the range of $\delta^{18}O_{PO4}$ values. Therefore, while the absolute temperature reconstructions differ depending on the chosen calibration, the difference between the Cenomanian and Maastrichtian records is small. In addition, the calibration of Lecuyer et al. (2013) benefits from the smallest uncertainty of ±1.2°C, which we apply to all tooth enamel SST values.

$\mathbf{TEX_{86}}$

TEX_{86} is a relatively new SST proxy method based on the ratio of different glycerol dialkyl glycerol tetraethers (GDGTs) with 86 carbons, which comprise membrane lipids in marine Crenarchaeota (Schouten et al., 2002). It has the benefit of not relying on $\delta^{18}O_{sw}$ assumptions. Here, we use the calibration of Kim et al. (2010) TEX_{86}^{H}, which provides the smallest error in warm climate conditions. The equation is:

$T(°C) = 68.4 \log(TEX_{86}) + 38.6$. (9)

Modern calibration by Kim et al. (2010) show an uncertainty of ±2.5°C, which we use in our model/proxy comparison.

We include the high-latitude Maastrichtian TEX_{86}^{H} SST value from Jenkyns et al. (2004) in our tables and plots for reference but do not include it in our analyses. We find, like several former studies (Davies et al., 2009; Spicer and Herman, 2010; Upchurch et al., 2015), that this value represents an extreme outlier from other proxy data and model results. Inclusion of this data point significantly skews our results, because it is the only available Arctic Maastrichtian SST value. Based on our other findings, it requires roughly 10°C warming from 50°N to 80°N, for which we have no physical basis.

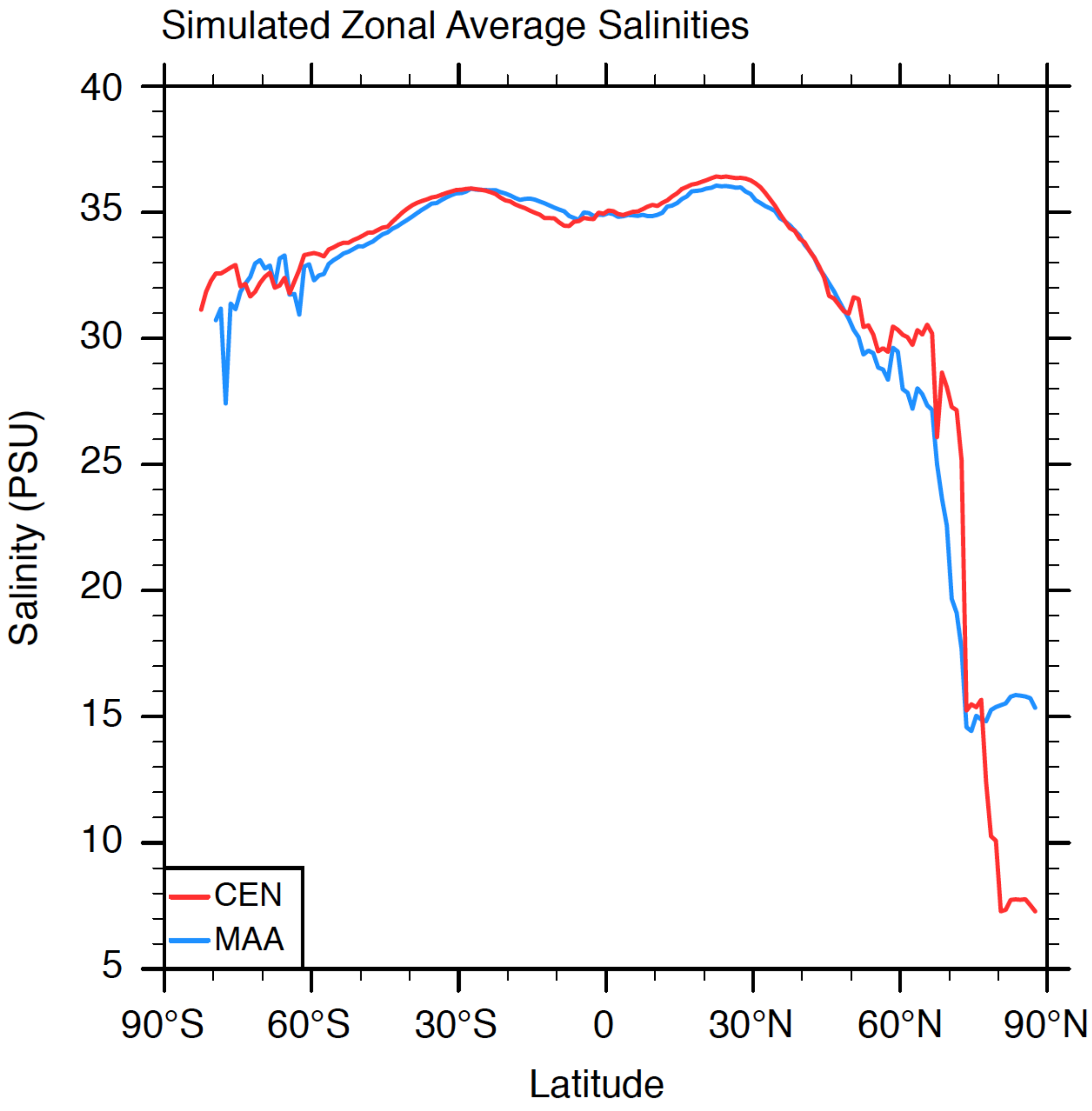

Appendix Figure 5.1: Model average zonal salinities

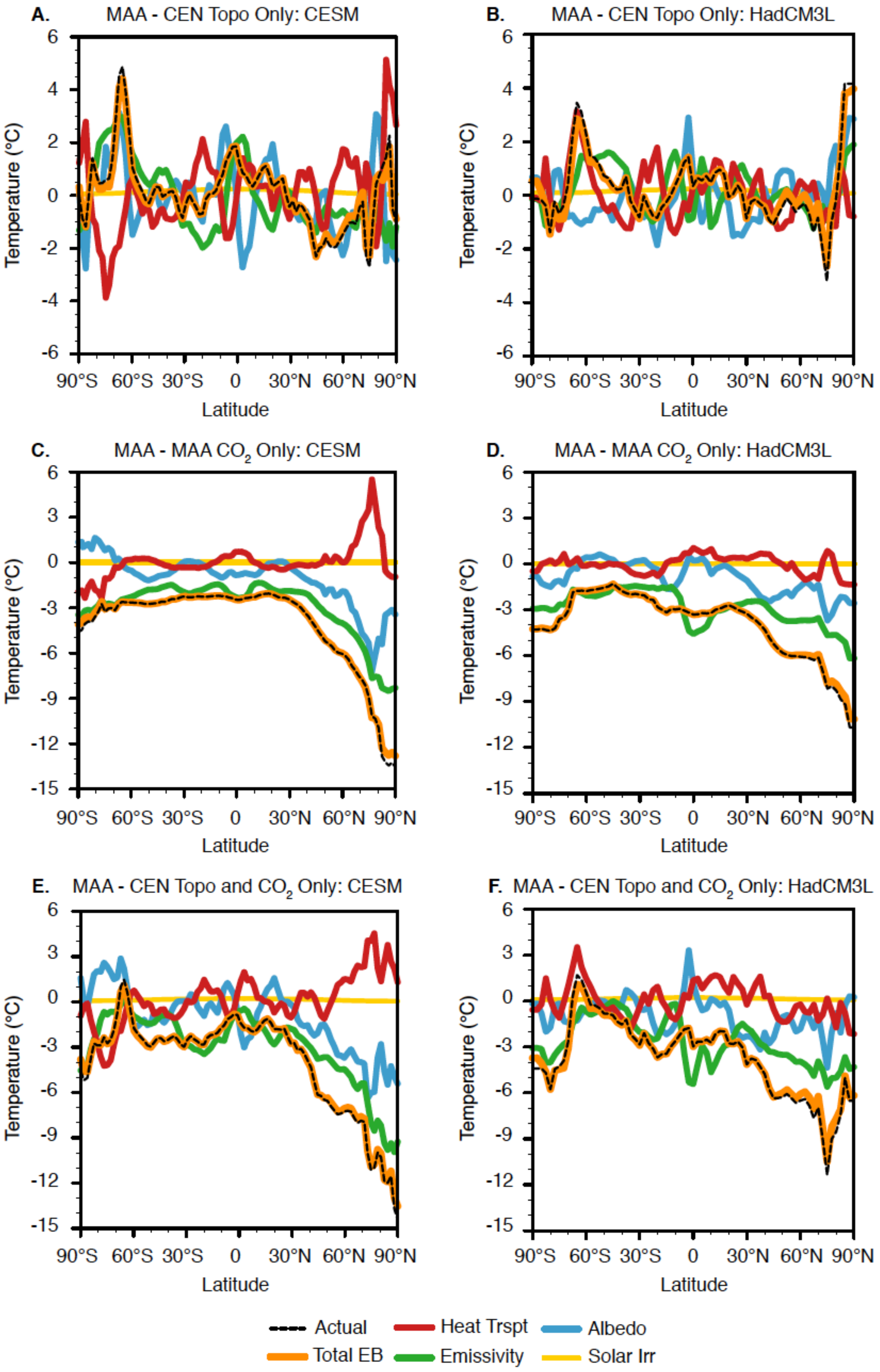
A.
MAA - CEN Topo Only: CESM
B.
MAA - CEN Topo Only: HadCM3L
C.
MAA - MAA CO$_2$ Only: CESM
D.
MAA - MAA CO$_2$ Only: HadCM3L
E.
MAA - CEN Topo and CO$_2$ Only: CESM
F.
MAA - CEN Topo and CO$_2$ Only: HadCM3L
Temperature (°C)
6
4
2
0
-2
-4
-6
3
-3
-9
-12
-15
90°S
60°S
30°S
0
30°N
60°N
90°N
Latitude
Actual
Heat Trspt
Albedo
Total EB
Emissivity
Solar Irr

Appendix Figure 5.2: Late Cretaceous energy balance calculations

Decomposition of the simulated changes in zonal mean surface temperature into contributions from heat transport (red), emissivity (green), albedo (blue), and TSI (yellow) for A) CESM and B) HadCM3L changes in geography, C) CESM and D) HadCM3L changes in CO_2, and E) CESM and F) HadCM3L changes in both geography and CO_2. See supplement methods for details on energy balance calculations.

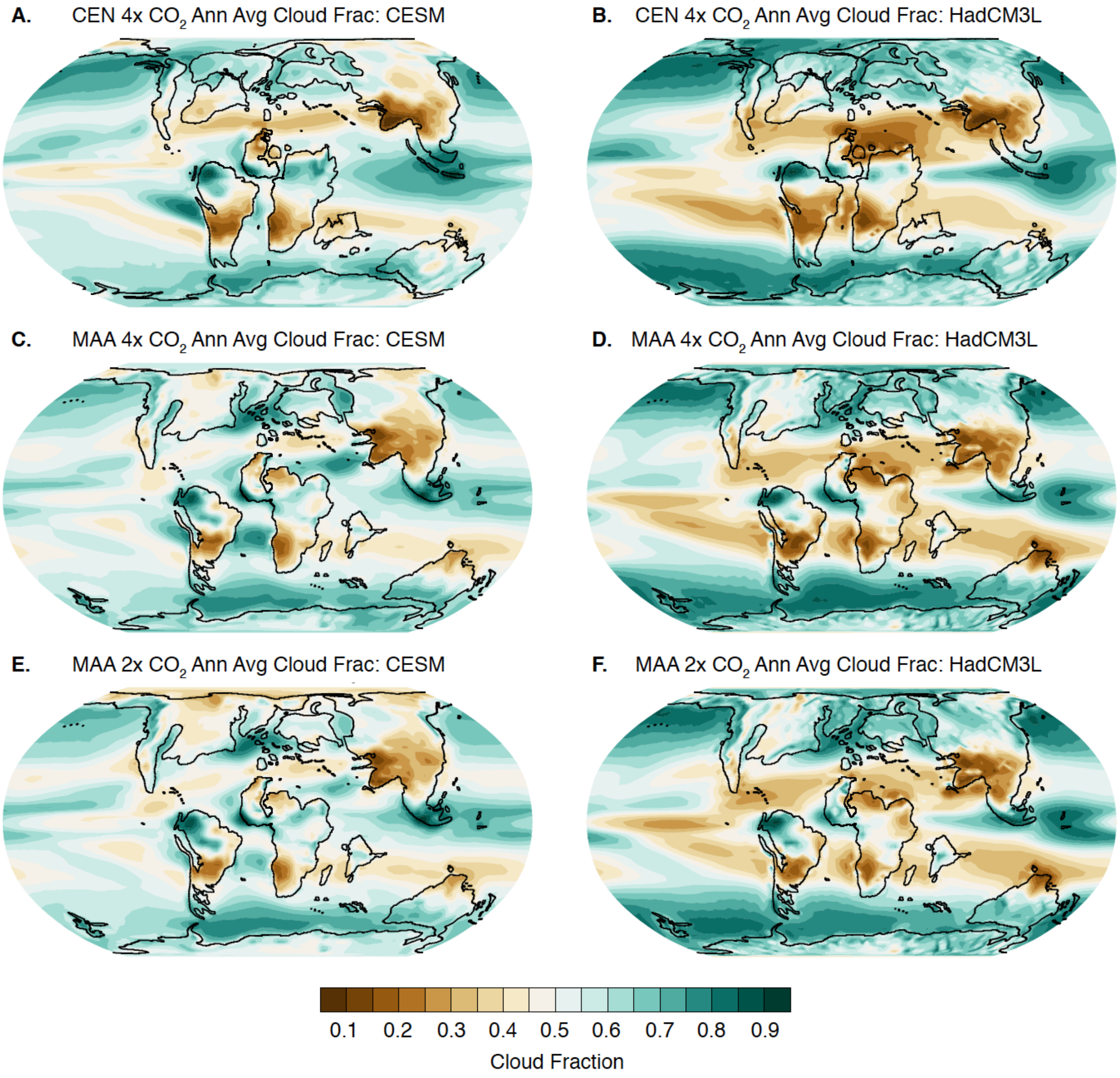

Appendix Figure 5.3: Late Cretaceous mean annual total cloud cover

Clouds remain one of the largest uncertainties in climate models. Both models show similar cloud patterns for all model configurations. However, the range of cloud cover between regions is more pronounced in HadCM3L than CESM. The configuration of the CESM aerosols for paleoclimate might be partly responsible for the discrepancies in cloud magnitude.

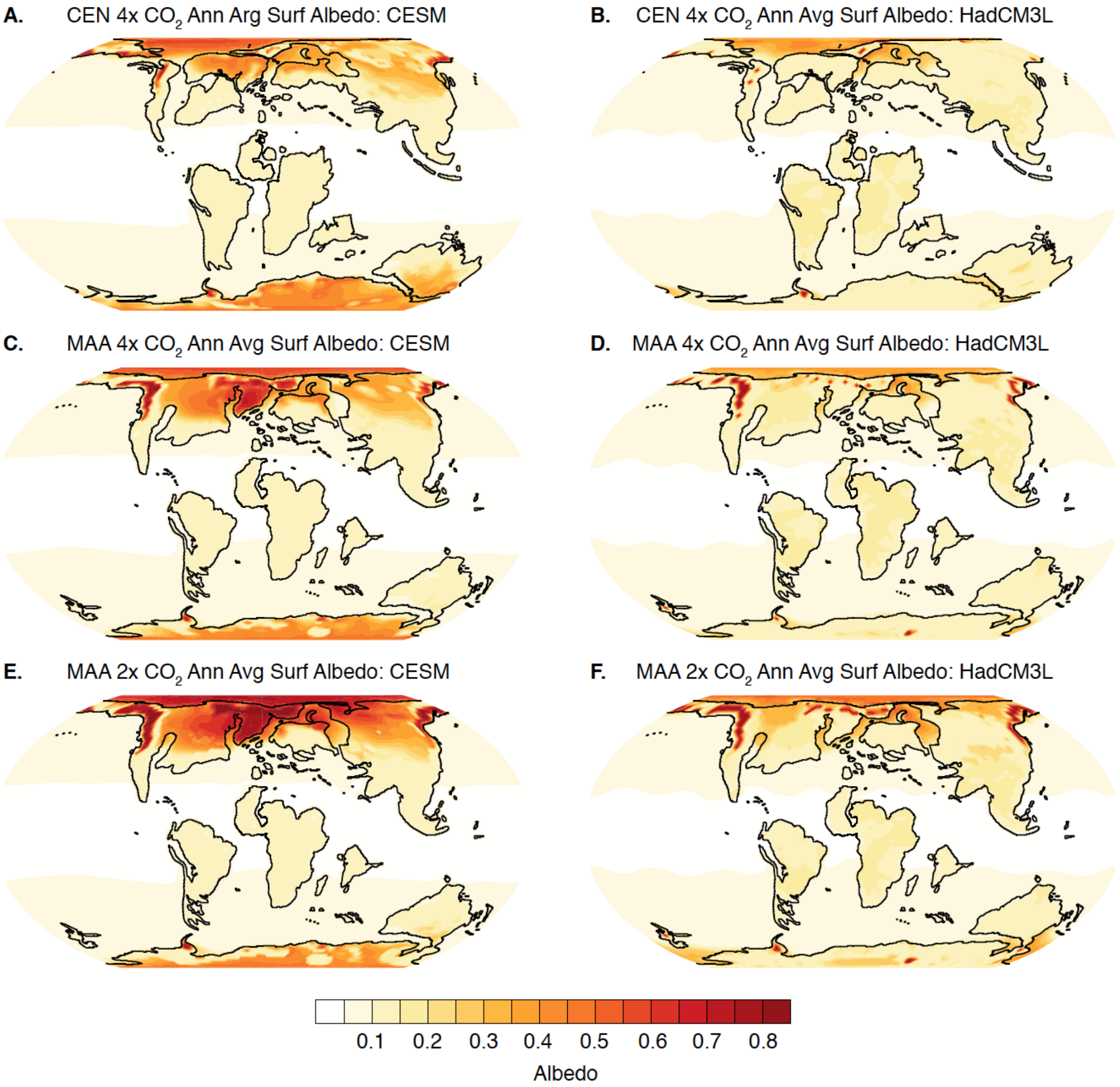

Appendix Figure 5.4: Late Cretaceous mean annual surface albedos
Model surface albedos agree in the low- and mid-latitudes. In the high-latitudes, CESM simulates higher surface albedos than HadCM3L due to differences in sea ice cover and vegetation. CESM tends to produce more sea in the Arctic than HadCM3L, which leads to greater shortwave reflection, especially in the spring and fall. CESM also grows shorter, less dense vegetation than HadCM3L in the polar regions. As a result, the tree-canopy masks less snow-cover in CESM, which raises the albedo. It appears dynamic vegetation in CESM does not want to grow the tall, dense Antarctic vegetation suggested by paleobotantical reconstructions (e.g. Upchurch et al., 1999). Modification of the vegetation model will be an important step in our future work, as some research shows vegetation can help remedy model/proxy LST discrepancies (e.g. Otto-Bliesner and Upchurch, 1998; Zhou et al., 2012).

A. CEN 4x CO_2 Ann Avg Sea Ice: CESM NH

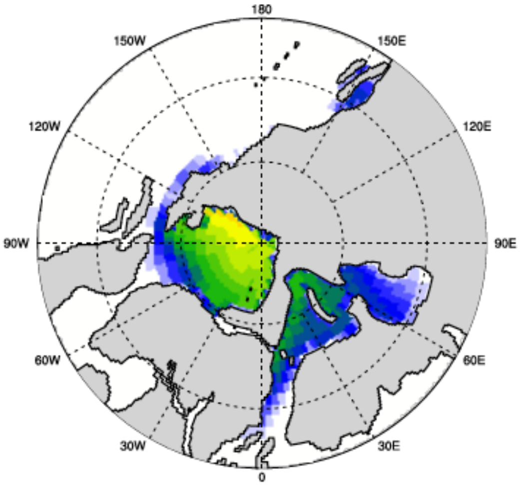

B. CEN 4x CO_2 Ann Avg Sea Ice: HadCM3L NH

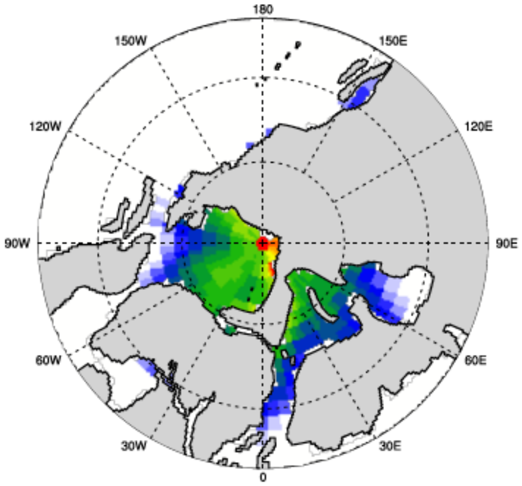

C. CEN 4x CO_2 Ann Avg Sea Ice: CESM SH

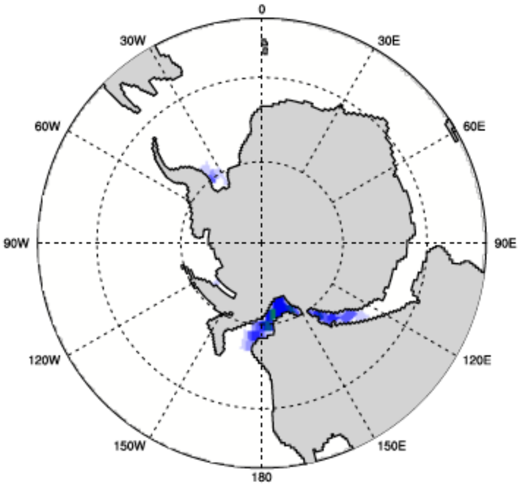

D. CEN 4x CO_2 Ann Avg Sea Ice: HadCM3L SH

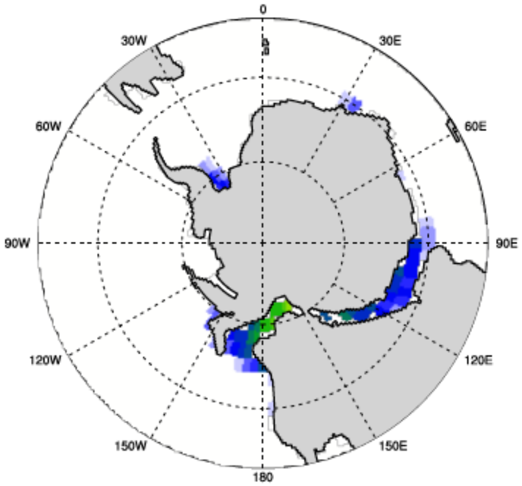

E. MAA 4x CO_2 Ann Avg Sea Ice: CESM NH

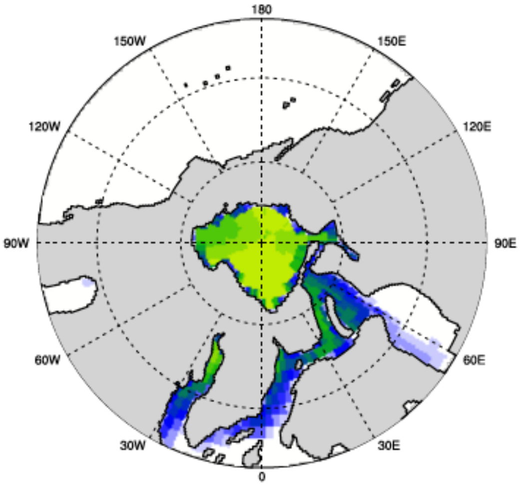

F. MAA 4x CO_2 Ann Avg Sea Ice: HadCM3L NH

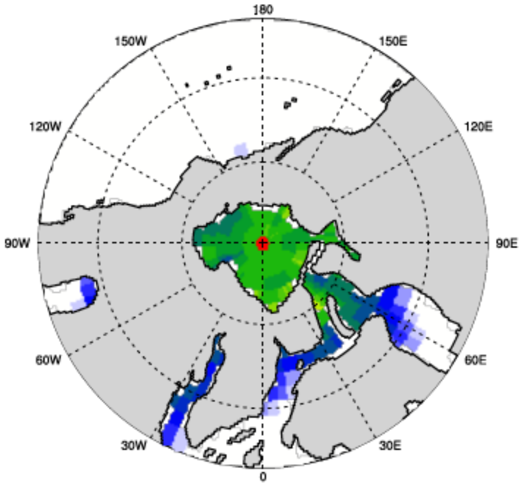

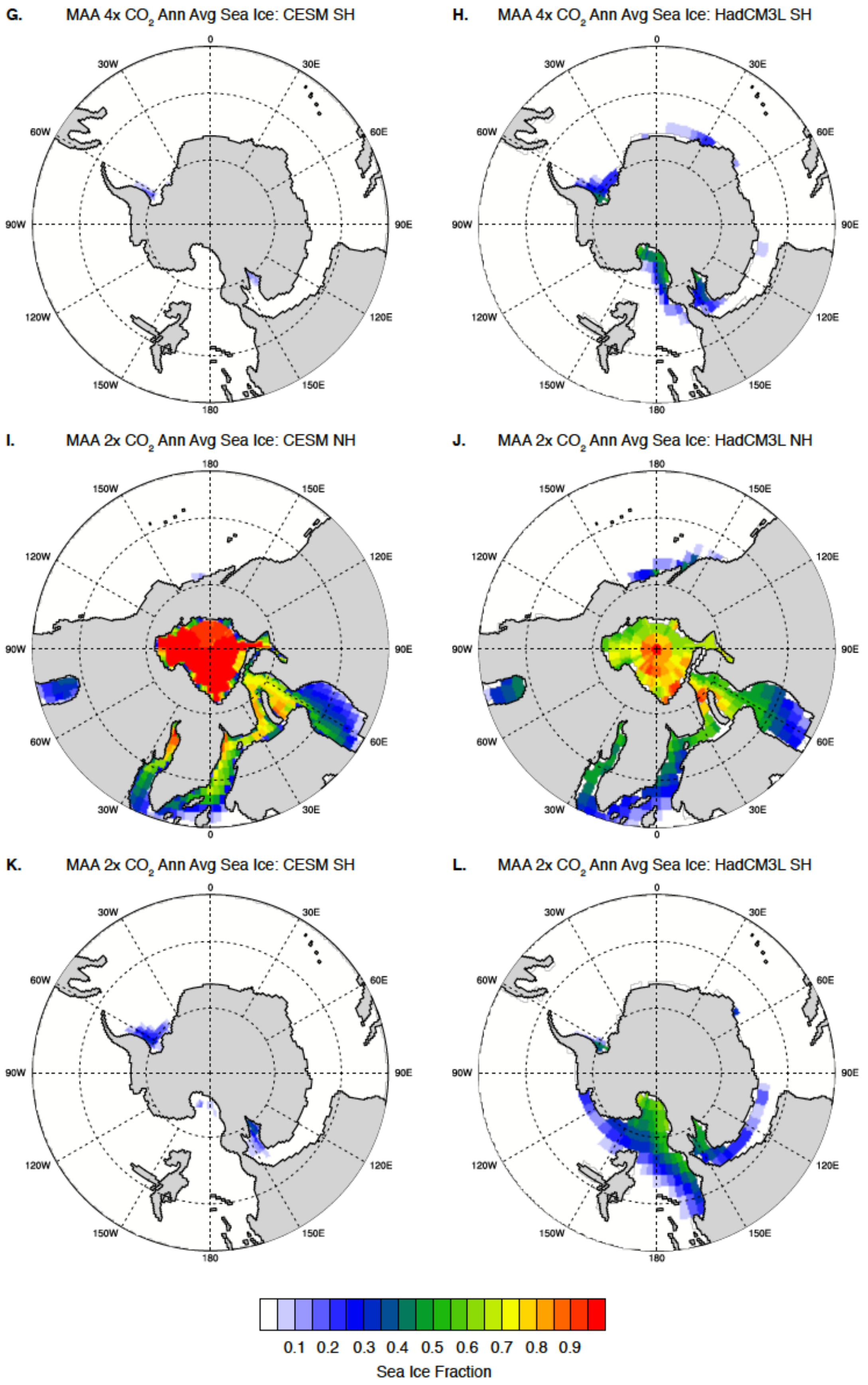

G. MAA 4x CO_2 Ann Avg Sea Ice: CESM SH

H. MAA 4x CO_2 Ann Avg Sea Ice: HadCM3L SH

I. MAA 2x CO_2 Ann Avg Sea Ice: CESM NH

J. MAA 2x CO_2 Ann Avg Sea Ice: HadCM3L NH

K. MAA 2x CO_2 Ann Avg Sea Ice: CESM SH

L. MAA 2x CO_2 Ann Avg Sea Ice: HadCM3L SH

Appendix Figure 5.5: Late Cretaceous annual mean sea ice cover

Seasonal sea ice exists in all 4x CO_2 simulations in agreement with some proxy records that find evidence for Arctic sea ice during peak Cretaceous warmth (Davies et al., 2009). The Arctic experiences an increase in sea ice concentration from the Cenomanian to Maastrichtian because the Arctic becomes more restricted in the Maastrichtian. With a reduction in CO_2, a significant amount of perennial sea ice forms in the Arctic while Antarctic sea ice remains mostly seasonal. This contrast in sea ice between hemispheres is similar to present-day where the restricted Arctic promotes retention of sea ice, and the open ocean Antarctic allows the equator drift and wasting of sea ice.

In all experiments, CESM produces greater Arctic sea ice cover and less Antarctic sea ice cover than HadCM3L. This contrast relates to the differences in open ocean SSTs between models. In general, CESM has greater ocean over turning in the high Southern latitudes, which promotes transports of warm equatorial water poleward and inhibits sea ice formation. In contrast, there is less deep-water formation in the high Northern latitudes in either model. Further, the Late Cretaceous Arctic is quite restricted from the greater ocean, especially in the Maastrichtian, which prevents warm open ocean waters from having a large effect.

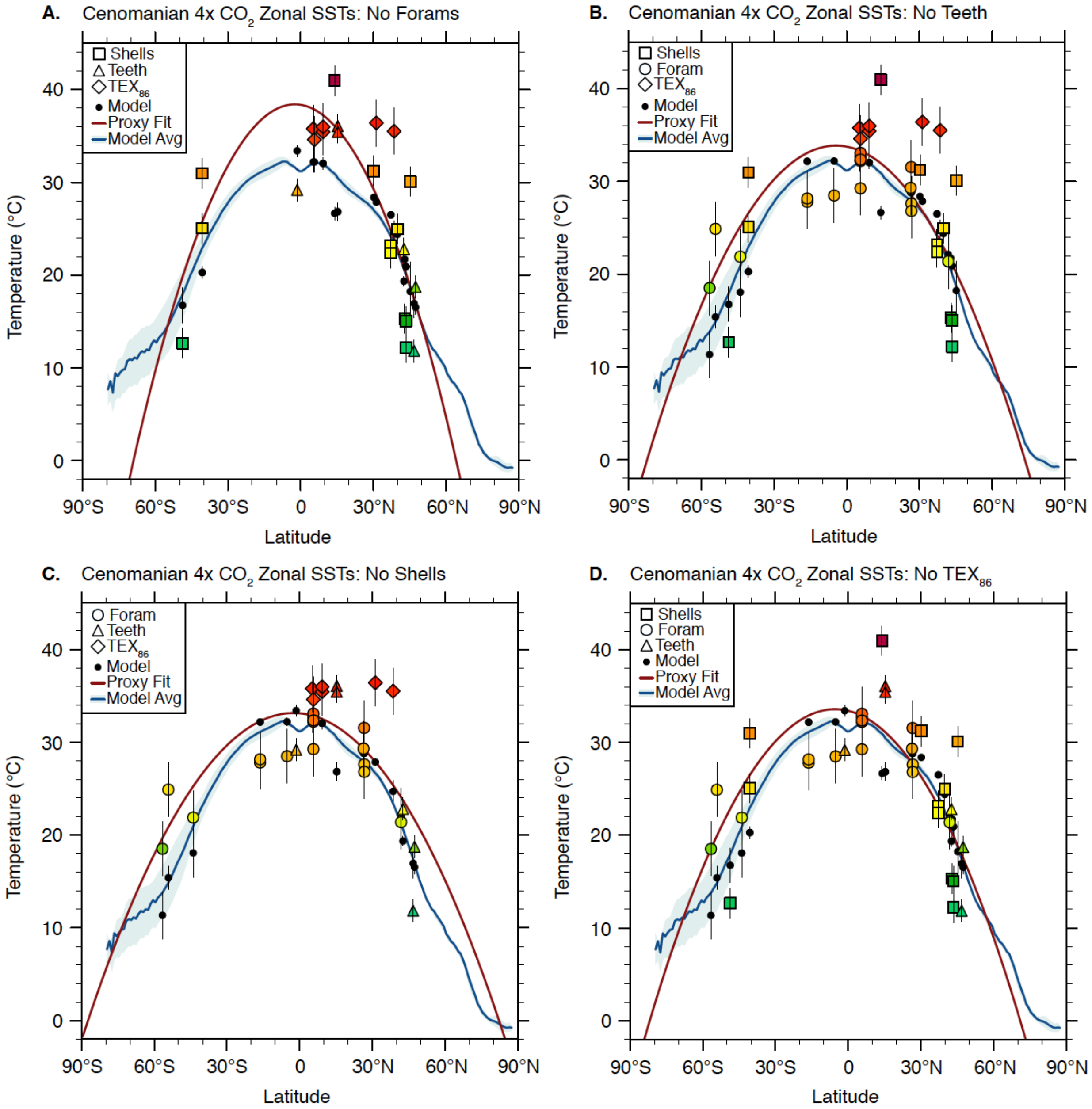

Appendix Figure 5.6: Cenomanian 4x CO$_2$ zonal mean SST reconstructions

Latitudinal temperature gradient reconstructions from the Cenomanian with the systematic removal of SST proxy reconstruction data from individual methods. Simulated 4x CO$_2$ Cenomanian zonal average SSTs with all Cenomanian proxies SST except A) foraminifera, B) fish tooth enamel, C) shells and related structures, and D) TEX$_{86}$. Removal of foraminifera leads to a significantly warmer equator and steeper equator-to-pole temperature gradient. This gradient is steeper than model simulated SSTs. It appears likely that some foraminifera are not recording a pure SST signal.

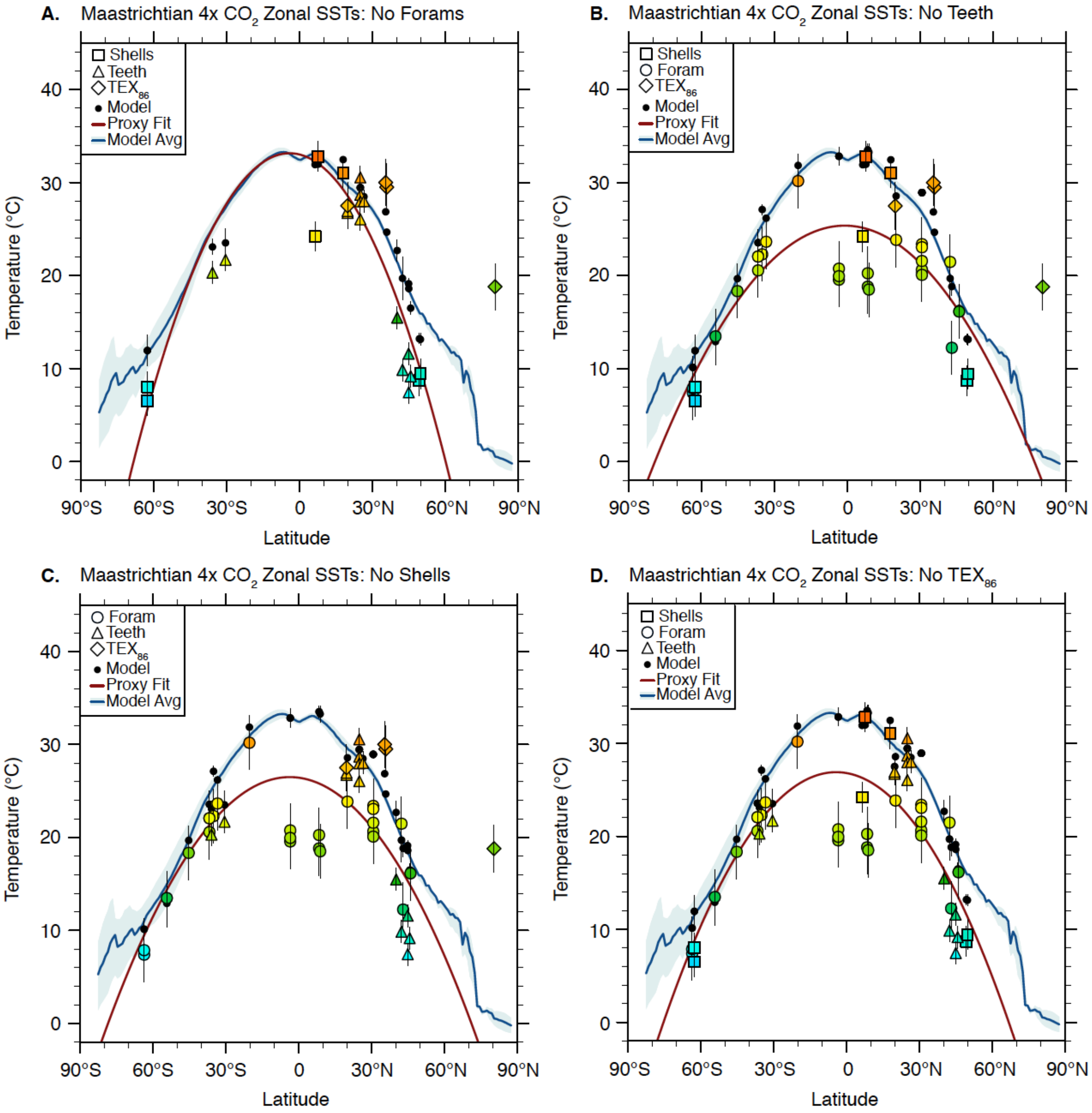

Appendix Figure 5.7: Maastrichtian 4x CO_2 zonal mean SST reconstructions

Latitudinal temperature gradient reconstructions from the Maastrichtian with the systematic removal of SST proxy reconstruction data from individual methods. Simulated 4x CO_2 Maastrichtian zonal average SSTs with all Maastrichtian proxies SST except A) foraminifera, B) fish tooth enamel, C) shells and related structures, and D) TEX_{86}. Like for the Cenomanian, removal of foraminifera leads to a significantly warmer equator and steeper equator-to-pole temperature gradient.

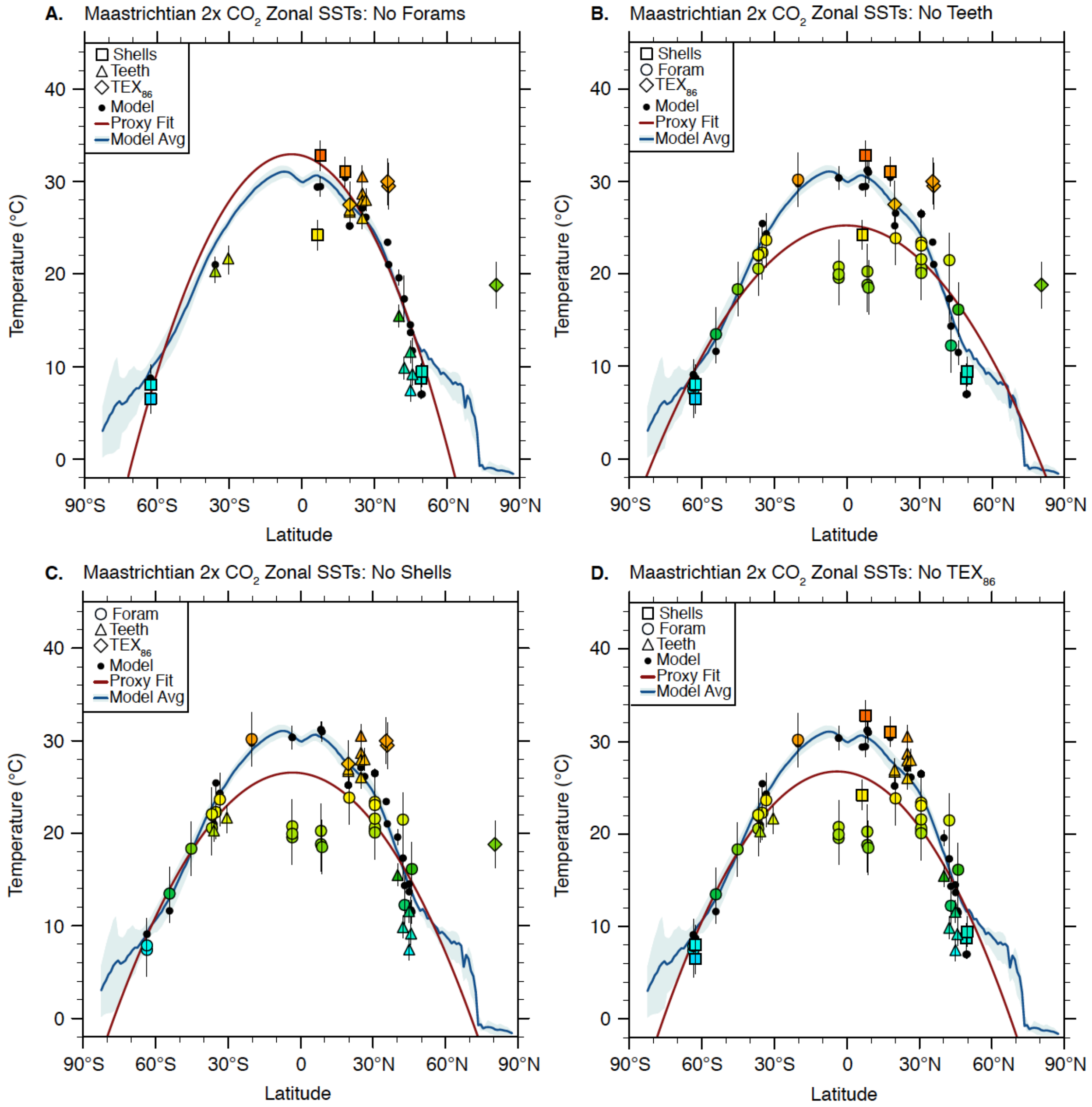

Appendix Figure 5.8: Maastrichtian 2x CO$_2$ zonal mean SST reconstructions

Figure S8. Identical to figure S7 except with simulated 4x CO$_2$ Maastrichtian data plotted.

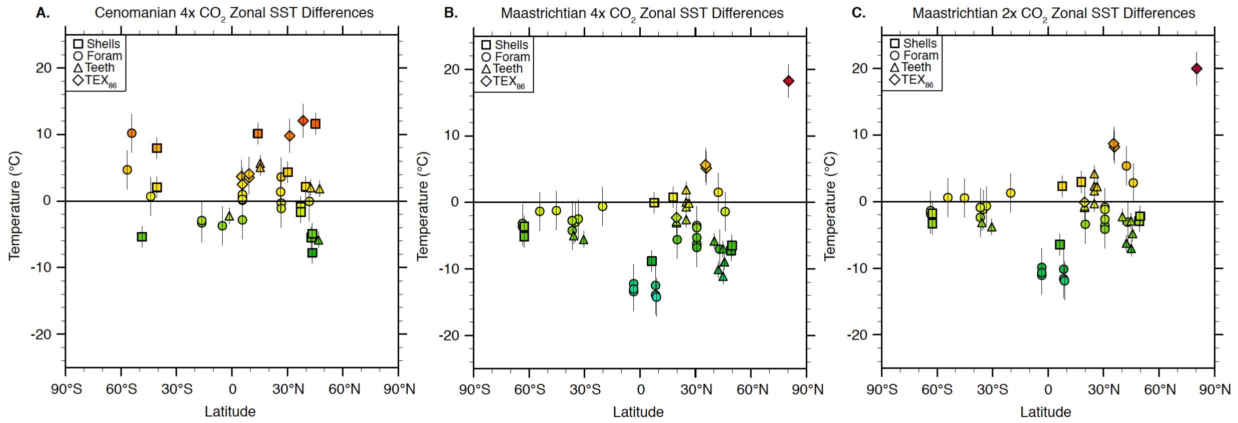

Appendix Figure 5.9: SST model/proxy discrepancies by latitude

A) Differences between Cenomanian proxies and 4x CO_2 Cenomanian simulations. B) Differences between Maastrichtian proxies and 4x CO_2 Maastrichtian simulations. C) Differences between Maastrichtian proxies and 2x CO_2 Maastrichtian simulations. In general, the 4x CO_2 Cenomanian model simulations have a cold bias while the 4x CO_2 Maastrichtian simulations have a warm bias. The 2x CO_2 Maastrichtian simulations are in better agreement with SST proxy records. A model warm bias remains in the equatorial region in the 2x CO_2 Maastrichtian, but this might be a result of diagenetic alteration of planktonic foramina. While beyond the scope of this work, calibration choices also impact model/proxy agreement. For example, the warmer fish tooth enamel calibration of Puceat et al. (2010) might result in a better agreement between models and proxies for the 2x Maastrichtian simulations.

Source	**Type**	**Age**	**Location**	**Paleo Lat**	**Paleo Lon**	**Temperature**
Abramovitch et al. 2003	Planktonic Forams	MAA	Walvis Ridge	-36.7	-8.5	22.1
Abramovitch et al. 2003	Planktonic Forams	MAA	Shatsky Rise	8.9	-166.3	18.5
Abramovitch et al. 2003	Planktonic Forams	MAA	Western Mid-Pacific Mtns	-3.4	-152.1	19.9
Alsenz et al. 2013	TEX86	MAA	Israel	19.8	31.2	27.5
Barrera and Savin 1999	Planktonic Forams	MAA	Maud Rise	-63.6	-3.6	7.9
Carpenter et al. 2003	Fish otolith	MAA	South Dakota	49.7	-73.9	9.4
Clarke and Jenkyns 1999	Composite Forams	MAA	Exmouth Plateau	-45.2	100.1	18.3
Dhondt and Lindinger 1994	Planktonic Forams	MAA	Walvis Ridge	20.1	1.6	23.9
Ditchfield et al. 1994	Mollusk	MAA	James Ross Island, AA	-62.6	-61.8	8.0
Frank and Arthur 1999	Planktonic Forams	MAA	Rio Grande Rise	-33.4	-18.2	23.6
Frank and Arthur 1999	Planktonic Forams	MAA	Blake Nose	30.7	-53.6	23.1
Frank and Arthur 1999	Planktonic Forams	MAA	Goban Spur	43.0	-9.8	12.2

Friedrich et al. 2004	Planktonic Forams	MAA	Blake Nose	30.7	-53.6	21.6
Friedrich et al. 2009	Planktonic Forams	MAA	Walvis Ridge	-36.7	-8.5	22.1
Friedrich et al. 2009	Planktonic Forams	MAA	Maud Rise	-63.6	-3.6	7.4
Huber et al. 1995	Planktonic Forams	MAA	Falkland Plateau	-54.2	-30.9	13.5
Huber et al. 1995	Planktonic Forams	MAA	Falkland Plateau	30.7	-53.6	20.6
Huber et al. 2002	Planktonic Forams	MAA	Blake Nose	30.7	-53.6	20.1
Huber et al. 2002	Planktonic Forams	MAA	Western Mid-Pacific Mtns	-3.4	-152.1	20.8
Huber et al. 2002	Planktonic Forams	MAA	Shatsky Rise	8.4	-166.2	20.3
Jenkyns et al. 2004	TEX86	MAA	Alpha Ridge	80.4	7.9	18.8
Kolodny and Luz 1991	Tooth Enamel	MAA	Morocco	25.0	-7.0	30.6
Kolodny and Luz 1991	Tooth Enamel	MAA	California, USA	42.4	-97.5	9.9
Kolodny and Raab 1988	Tooth Enamel	MAA	Israel	19.8	31.2	26.7
Lecuyer et al. 1993	Tooth Enamel	MAA	Morocco	25.0	-7.0	28.0
Li and Keller 1998	Planktonic Forams	MAA	Walvis Ridge	-36.7	-8.5	20.6
Li and Keller 1999	Planktonic Forams	MAA	Western Mid-Pacific Mtns	-3.4	-152.1	19.6
Linnert et al. 2014	TEX86	MAA	Mississippi, USA	35.9	-65.2	29.5
MacLeod et al. 2005	Planktonic Forams	MAA	Blake Nose	30.7	-53.6	23.4
Maestas et al. 2003	Planktonic Forams	MAA	California	42.4	-97.5	21.5
Ounis et al. 2008	Tooth Enamel	MAA	Tunisia	26.5	9.1	28.0
Pearson et al. 2001	Planktonic Forams	MAA	Lindi, Tanzania	-20.2	33.3	30.2
Pirrie and Marshall 1990	Mollusk	MAA	James Ross Island, AA	-62.6	-61.8	6.5
Puceat et al. 2003	Tooth Enamel	MAA	Israel	19.8	31.2	27.0
Puceat et al. 2003	Tooth Enamel	MAA	Morocco	25.0	-7.0	26.1
Puceat et al. 2003	Tooth Enamel	MAA	Eben-Emae, Belgium	44.9	4.9	11.6
Puceat et al. 2007	Tooth Enamel	MAA	Las Tablas, Chile	-30.5	-54.7	21.7
Puceat et al. 2007	Tooth Enamel	MAA	Algarrobo, Chile	-35.8	-55.8	20.3
Puceat et al. 2007	Tooth Enamel	MAA	Morocco	25.0	-7.0	28.7

Puceat et al. 2007	Tooth Enamel	MAA	Nasilov, Poland	45.7	20.7	9.2
Puceat et al. 2007	Tooth Enamel	MAA	New Jersey, USA	40.2	-49.7	15.5
Puceat et al. 2007	Tooth Enamel	MAA	Maastricht, The Netherlands	44.9	6.1	7.5
Schoenfeld et al. 1991	Planktonic Forams	MAA	Northern Germany	46.0	10.4	16.1
Steuber et al. 2005	Rudist	MAA	Jamaica	17.9	-71.9	31.0
Steuber et al. 2005	Rudist	MAA	Oman	7.7	48.9	32.8
Vellekoop et al. 2013	TEX86	MAA	Texas, USA	35.4	-74.4	30.0
Wilson and Opdyke 1996	Rudist	MAA	Wobejebato Guyot	6.4	-36.9	24.2
Zakharov et al. 2006	Planktonic Forams	MAA	Shatsky Rise	8.4	-166.2	18.8
Zakharov et al. 2006	Rudist	MAA	South Dakota	49.3	-74.4	8.7
Zakharov et al. 2006	Planktonic Forams	MAA	Ontong-Java Plateau	-35.0	152.0	22.3
Zakharov et al. 2006	Planktonic Forams	MAA	Blake Nose	30.7	-53.6	20.3
Ando et al. 2009	Planktonic Forams	CEN	Blake Nose	26.7	-41.3	26.8
Bice et al. 2006	Planktonic Forams	CEN	Demerara Rise	5.7	-26.6	32.4
Clarke and Jenkyns 1999	Composite Forams	CEN	Exmouth Plateau	-43.9	97.9	21.9
El-Shazy et al. 2011	Rudist	CEN	Czech Republic	45.2	19.6	30.1
El-Shazy et al. 2011	Rudist	CEN	Egypt	14.0	30.0	41.0
Forster et al. 2007a	TEX86	CEN	Demerara Rise	5.2	-26.0	35.8
Forster et al. 2007a	TEX86	CEN	Cape Verde Basin	9.3	-21.3	35.4
Forster et al. 2007b	TEX86	CEN	Demerara Rise	5.7	-26.6	34.6
Friedrich et al. 2008	Planktonic Forams	CEN	Demerara Rise	5.7	-26.6	33.1
Gustafsson et al. 2003	Planktonic Forams	CEN	Goban Spur	41.9	-6.3	21.4
Henderson and Price 2012	Mollusk	CEN	Northern Australia	-40.6	123.6	31.0
Henderson and Price 2012	Mollusk	CEN	Northern Australia	-40.6	123.6	25.1
Huber et al. 1995	Planktonic Forams	CEN	Falkland Plateau	-54.2	-13.8	24.9
Huber et al. 1995	Planktonic Forams	CEN	Naturaliste Plateau	-56.6	88.9	18.5
Huber et al.	Planktonic	CEN	Blake Nose	26.7	-41.3	27.6

2002	Forams					
Kolodny and Luz 1991	Tooth Enamel	CEN	Angola	-1.4	9.2	29.2
Kolodny and Raab 1988	Tooth Enamel	CEN	Israel	15.3	33.0	36.1
Kolodny and Raab 1991	Tooth Enamel	CEN	Israel	15.3	33.0	35.4
Moriya et al. 2007	Planktonic Forams	CEN	Demerara Rise	5.7	-26.6	32.7
Norris and Wilson 1998	Planktonic Forams	CEN	Blake Plateau	26.6	-41.9	31.6
Norris et al. 2002	Planktonic Forams	CEN	Demerara Rise	5.7	-26.6	32.2
Price and Hart 2001	Planktonic Forams	CEN	Western Mid-Pacific Mtns	-16.3	-143.3	27.8
Price et al. 1998	Planktonic Forams	CEN	Western Mid-Pacific Mtns	-16.3	-143.3	28.2
Price et al. 1998	Planktonic Forams	CEN	Shatsky Rise	-5.2	-158.3	28.5
Price et al. 2012	belemnite rostra	CEN	Boologooro	-48.7	97.7	12.7
Puceat et al. 2003	Tooth Enamel	CEN	France	42.6	2.4	22.8
Puceat et al. 2007	Tooth Enamel	CEN	Germany	46.8	14.4	11.9
Puceat et al. 2007	Tooth Enamel	CEN	Poland	47.4	24.9	18.7
Schouten et al. 2003	TEX86	CEN	North Atlantic	31.3	-34.7	36.4
Schouten et al. 2003	TEX86	CEN	Cape Verde Basin	9.3	-21.3	36.0
Sellwood et al. 1994	Planktonic Forams	CEN	Demerara Rise	5.7	-26.6	29.3
Sellwood et al. 1994	Planktonic Forams	CEN	Mazagan Plateau	26.4	-4.1	29.3
Sinninghe Damsté et al. 2010	TEX86	CEN	Newfoundland Basin	38.6	-9.9	35.5
Steuber et al. 2005	Rudist	CEN	France	39.9	5.2	25.0
Steuber et al. 2005	Rudist	CEN	Croatia	30.2	22.1	31.2
Voigt et al. 2003	brachiopods	CEN	England	43.4	5.7	15.1
Voigt et al. 2003	brachiopods	CEN	Tagle East	37.3	3.4	22.4
Voigt et al. 2004	brachiopods	CEN	England	43.4	5.7	12.2
Voigt et al. 2004	brachiopods	CEN	Spain	37.3	3.4	23.2
Voigt et al. 2004	brachiopods	CEN	France	43.0	7.7	15.3

Appendix Table 5.1: All Cretaceous SST proxy data
See supplemental methods for details on collection, averaging, calibration, and uncertainty.

Bibliography

Abramovich, S., Keller, G., Stüben, D., and Berner, Z., 2003, Characterization of late Campanian and Maastrichtian planktonic foraminiferal depth habitats and vital activities based on stable isotopes: Palaeogeography Palaeoclimatology Palaeoecology, v. 202, no. 1-2, p. 1–29, doi: 10.1016/S0031-0182(03)00572-8.

Alsenz, H., Regnery, J., Ashckenazi-Polivoda, S., Meilijson, A., Ron-Yankovich, L., Illner, P., Abramovich, S., Almogi-Labin, A., Feinstein, S., Berner, Z., and Püttmann, W., 2013, Characterization of late Campanian and Maastrichtian planktonic foraminiferal depth habitats and vital activities based on stable isotopes: Palaeogeography Palaeoclimatology Palaeoecology, v. 392, no. C, p. 350–358, doi: 10.1016/j.palaeo.2013.09.013.

Anderson, T.F., Kaplan, R., Veizer, J., and Land, L.S., 1983, Stable isotopes in sedimentary geology: Soc Econ Paleont Min.

Ando, A., Nakano, T., Kaiho, K., and Kobayashi, T., 2009, Onset of seawater 87Sr/86Sr excursion prior to Cenomanian–Turonian Oceanic Anoxic Event 2? New Late Cretaceous strontium isotope curve from the central Pacific Ocean: Journal of Foraminiferal Research, v39, no 4, p. 322-334.

Barrera, E., and Savin, S.M., 1999, Evolution of late Campanian-Maastrichtian marine climates and oceans: Geological Society of American-Special Papers, v. 332.

Beerling, D.J., and Royer, D.L., 2011, Convergent Cenozoic CO2 history: Nature Geoscience, v. 4, no. 7, p. 418–420, doi: 10.1038/ngeo1186.

Bemis, E.B., Spero, H.J., Bijma, J., and Lea, D.W., 1998, Reevaluation of the oxygen isotopic composition of planktonic foraminifera: Experimental results and revised paleotemperature equations: Paleoceanography, v. 13, no. 2, p. 150-160.

Berner, R.A., and Kothavala, Z., 2001, GEOCARB III: a revised model of atmospheric CO2 over Phanerozoic time: American Journal of Science, v. 301, p. 182-204.

Bice, K.L., Birgel, D., Meyers, P.A., Dahl, K.A., Hinrichs, K.U., and Norris, R.D., 2006, A multiple proxy and model study of Cretaceous upper ocean temperatures and atmospheric CO2 concentrations: Paleoceanography, v. 21, no. 2, doi: 10.1029/2005PA001203.

Bowman, V.C., Francis, J.E., and Riding, J.B., 2013, Late Cretaceous winter sea ice in Antarctica?: Geology, v. 41, no. 12, p. 1227–1230, doi: 10.1130/G34891.1.

Boyce, C.K., Brodribb, T.J., Feild, T.S., and Zwieniecki, M.A., 2009, Angiosperm leaf vein evolution was physiologically and environmentally transformative: Proceedings of the Royal Society B: Biological Sciences, v. 276, no. 1663, p. 1771–1776, doi: 10.1080/00241160310004657.

Broecker, W.S., 1989, The Salinity Contrast Between the Atlantic and Pacific Oceans During Glacial Time: Paleoceanography, v. 4, no. 2, p. 207–212, doi: 10.1029/PA004i002p00207.

Carpenter, S.J., Erickson, J.M., and Holland, F.D., 2003, Migration of a Late Cretaceous fish: Nature, v. 423, no. 6935, p. 70–74, doi: 10.1038/nature01588.

Clarke, L.J., and Jenkyns, H.C., 1999, New oxygen isotope evidence for long-term Cretaceous climatic change in the Southern Hemisphere: Geology, v. 27, no. 8, p. 699–702.

Cox, P. M., Betts, R. A., Jones, C. D., Spall, S. A., and Totterdell,I. J.:Modelling vegetation and the carbon cycle as interactive elements of the climate system, in: Meteorology at the Millennium,edited by Pearce, R., pp. 259–279, Academic Press, 2001.

Crowley, T.J., and Zachos, J.C., 2000, Comparison of zonal temperature profiles for past warm time periods: Warm Climates in Earth History, p. 50-76.

D'Hondt, S., and Lindinger, M., 1994, A stable isotopic record of the Maastrichtian ocean-climate system: South Atlantic DSDP Site 528: Palaeogeography, v. 112, p. 363-378.

Damste, J.S.S., van Bentum, E.C., Reichart, G.-J., Pross, J., and Schouten, S., 2010, Earth and Planetary Science Letters: Earth and Planetary Science Letters, v. 293, no. 1-2, p. 97–103, doi: 10.1016/j.epsl.2010.02.027.

Davies, A., Kemp, A.E.S., and Pike, J., 2009, Late Cretaceous seasonal ocean variability from the Arctic: Nature, v. 460, no. 7252, p. 254–U118, doi: 10.1038/nature08141.

Ditchfield, P.W., Marshall, J.D., and Pirrie, D., 1994, High latitude palaeotemperature variation: New data from the Thithonian to Eocene of James Ross Island, Antarctica: Palaeogeography, v. 107, p. 79-101.

Donnadieu, Y., Pierrehumbert, R., Jacob, R., and Fluteau, F., 2006, Modelling the primary control of paleogeography on Cretaceous climate: Earth and Planetary Science Letters, v. 248, no. 1-2, p. 426–437, doi: 10.1016/j.epsl.2006.06.007.

El-Shazly, S., Košťák, M., Kloučková, B., Saber, S.G., Felieh Salama, Y., Mazuch, M., and Žák, K., 2011, Carbon and oxygen stable isotopes of selected Cenomanian and Turonian rudists from Egypt and Czech Republic, and a note on changes in rudist diversity: Bulletin of Geosciences,, p. 209–226, doi: 10.3140/bull.geosci.1151.

Erez, J., and Luz, B., 1983, Experimental paleotemperature equation for planktonic foraminifera: Geochimica Et Cosmochimica Acta, v. 47, p. 1025-1031.

Feng, R., and Poulsen, C.J., 2014, Andean elevation control on tropical Pacific climate and ENSO: Paleoceanography, v. 29, no. 8, p. 795–809, doi: 10.1002/(ISSN)1944-9186.

Feng, R., Poulsen, C.J., Werner, M., Chamberlain, C.P., Mix, H.T., and Mulch, A., 2013, Early Cenozoic evolution of topography, climate, and stable isotopes in precipitation in the North American Cordillera: American Journal of Science, v. 313, no. 7, p. 613–648, doi: 10.2475/07.2013.01.

Forster, A., Schouten, S., Baas, M., and Damste, J.S.S., 2007a, Mid-Cretaceous (Albian-Santonian) sea surface temperature record of the tropical Atlantic Ocean: Geology, v. 35, no. 10, p. 919–922, doi: 10.1130/G23874A.1.

Forster, A., Schouten, S., Moriya, K., Wilson, P.A., and Sinninghe Damsté, J.S., 2007b, Tropical warming and intermittent cooling during the Cenomanian/Turonian oceanic anoxic event 2: Sea surface temperature records from the equatorial Atlantic: Paleoceanography, v. 22, no. 1, doi: 10.1029/2006PA001349.

Frank, T.D., and Arthur, M.A., 1999, Tectonic forcings of Maastrichtian ocean-climate evolution: Paleoceanography, v. 14, no. 2, p. 103–117.

Friedrich, O., Erbacher, J., Moriya, K., Wilson, P.A., and Kuhnert, H., 2008, Warm saline intermediate waters in the Cretaceous tropical Atlantic Ocean: Nature Geoscience, v. 1, no. 7, p. 453–457, doi: 10.1038/ngeo217.

Friedrich, O., Herrle, J.O., Kößler, P., and Hemleben, C., 2004, Early Maastrichtian stable isotopes: changing deep water sources in the North Atlantic?: Palaeogeography Palaeoclimatology Palaeoecology, v. 211, no. 1-2, p. 171–184, doi: 10.1016/j.palaeo.2004.05.004.

Friedrich, O., Herrle, J.O., Wilson, P.A., Cooper, M.J., Erbacher, J., and Hemleben, C., 2009, Early Maastrichtian carbon cycle perturbation and cooling event: Implications from the South Atlantic Ocean: Paleoceanography, v. 24, no. 2, p. n/a–n/a, doi: 10.1029/2008PA001654.

Friedrich, O., Norris, R.D., and Erbacher, J., 2012, Evolution of middle to Late Cretaceous oceans--A 55 m.y. record of Earth's temperature and carbon cycle: Geology, v. 40, no. 2, p. 107–110, doi: 10.1130/G32701.1.

Gent, P.R., Danabasoglu, G., Donner, L.J., Holland, M.M., Hunke, E.C., Jayne, S.R., Lawrence, D.M., Neale, R.B., Rasch, P.J., Vertenstein, M., Worley, P.H., Yang, Z.-L., and Zhang, M., 2011, The Community Climate System Model Version 4: Journal of Climate, v. 24, no. 19, p. 4973–4991, doi: 10.1175/2011JCLI4083.1.

Gordon, C., Cooper, C., Senior, C.A., Banks, H., and Gregory, J.M., 2000, The simulation of SST, sea ice extents and ocean heat transports in a version of the Hadley Centre coupled model without flux adjustments: Climate Dynamics, v. 16, p. 147-168.

Gough, D.O., 1981, Solar interior structure and luminosity variations: Physics of Solar Variations, v. 74, p. 21-34.

Grossman, E.L., and Ku, T.L., 1986, Oxygen and carbon isotope fractionation in biogenic aragonite: temperature effects: Chemical Geology: Isotope Geoscience section, v. 59; p. 59-74.

Gustafsson, M., Holbourn, A., and Kuhnt, W., 2003, Changes in Northeast Atlantic temperature and carbon flux during the Cenomanian/Turonian paleoceanographic event: the Goban Spur stable isotope record: Palaeogeography Palaeoclimatology Palaeoecology, v. 201, no. 1-2, p. 51–66, doi: 10.1016/S0031-0182(03)00509-1.

Heavens, N.G., Shields, C.A., and Mahowald, N.M., 2012, A paleogeographic approach to aerosol prescription in simulations of deep time climate: Journal of Advances in Modeling Earth Systems, v. 4, no. 4, p. n/a–n/a, doi: 10.1029/2012MS000166.

Heinemann, M., Jungclaus, J.H., and Marotzke, J., 2009, Warm Paleocene/Eocene climate as simulated in ECHAM5/MPI-OM: Climate of the Past, v. 5, p. 785-802.

Henderson, R.A., and Price, G.D., 2012, Paleoenvironment and paleoecology from oxygen and carbon isotopes of subtropical mollusks from the Late Cretaceous (Cenomanian) of Bathurst Island, Australia: Palaios, v. 27, no. 9, p. 617–626, doi: 10.2110/palo.2011.p11-120r.

Hill, D.J., Haywood, A.M., Lunt, D.J., Hunter, S.J., Bragg, F.J., Contoux, C., Stepanek, C., Sohl, L., Rosenbloom, N.A., Chan, W.L., Kamae, Y., Zhang, Z., Abe-Ouchi, A., Chandler, M.A., et al., 2014, Evaluating the dominant components of warming in Pliocene climate simulations: Climate of the Past, v. 10, no. 1, p. 79–90, doi: 10.5194/cp-10-79-2014.

Huber, B.T., Hodell, D.A., Hamilton, C.P., 1995, Middle–Late Cretaceous climate of the southern high latitudes: stable isotopic evidence for minimal equator-to-pole thermal gradients:

Geological Society of America, v. 107, no. 10, p. 1164-1191.

Huber, B.T., Norris, R.D., and MacLeod, K.G., 2002, Deep-sea paleotemperature record of extreme warmth during the Cretaceous: Geology.

Hunter, S.J., Haywood, A.M., Valdes, P.J., Francis, J.E., and Pound, M.J., 2013, Palaeogeography, Palaeoclimatology, Palaeoecology: Palaeogeography Palaeoclimatology Palaeoecology, v. 392, no. C, p. 41–51, doi: 10.1016/j.palaeo.2013.08.009.

Jenkyns, H.C., Forster, A., Schouten, S., and Damste, J., 2004, High temperatures in the Late Cretaceous Arctic Ocean: Nature, v. 432, no. 7019, p. 888–892, doi: 10.1038/nature03143.

Kiehl, J.T., and Shields, C.A., 2013, Sensitivity of the Palaeocene-Eocene Thermal Maximum climate to cloud properties: Philosophical Transactions of the Royal Society A: Mathematical, Physical and Engineering Sciences, v. 371, no. 2001, p. 20130093–20130093, doi: 10.1016/0169-5347(90)90081-N.

Kim, J.H., van der Meer, J., Schouten, S., Helmke, P., Willmott, V., Sangiorgi, F., Koç, N., Hopmans, E.C., and Damste, J.S.S., 2010, New indices and calibrations derived from the distribution of crenarchaeal isoprenoid tetraether lipids: Implicationsfor past sea surface temperature reconstructions: Geochimica Et Cosmochimica Acta, v. 74, no. 16, p. 4639–4654, doi: 10.1016/j.gca.2010.05.027.

Kolodny, Y., and Luz, B., 1991, Oxygen isotopes in phosphates of fossil fish—Devonian to Recent: The Geochemical Society, p. 105-119.

Kolodny, Y., and Raab, M., 1988, Oxygen isotopes in phosphatic fish remains from Israel: paleothermometry of tropical Cretaceous and Tertiary shelf waters: Palaeogeography, v. 64, p. 59-67.

Kump, L.R., and Pollard, D., 2008, Amplification of Cretaceous Warmth by Biological Cloud Feedbacks: Science, v. 320, no. 5873, p. 195–195, doi: 10.1126/science.1153883.

Lécuyer, C., Amiot, R., Touzeau, A., and Trotter, J., 2013, Calibration of the phosphate d18O thermometer with carbonate-water oxygen isotope fractionation equations: Chemical Geology, v. 347, no. C, p. 217–226, doi: 10.1016/j.chemgeo.2013.03.008.

Lécuyer, C., Grandjean, P., O'Neil, J.R., and Cappetta, H., 1993, Thermal excursions in the ocean at the Cretaceous—Tertiary boundary (northern Morocco): δ 18 O record of phosphatic fish debris: Palaeogeography, v. 105, p. 235-243.

Levis, S., Bonan, G.B., Vertenstein, M., and Oleson, K.W., 2004, The Community Land Model"s Dynamic Global Vegetation Model (CLM-DGVM): Technical Description and User"s Guide: National Center For Atmospheric Research.

Li, L., and Keller, G., 1999, Variability in Late Cretaceous climate and deep waters: evidence from stable isotopes: Marine Geology, v. 161, p. 171-190.

Li, L.Q., and Keller, G., 1998, Maastrichtian climate, productivity and faunal turnovers in planktic foraminifera in south Atlantic DSDP sites 525A and 21: Marine Micropaleontology, v. 33, no. 1-2, p. 55–86.

Linnert, C., Robinson, S.A., Lees, J.A., Bown, P.R., guez, I.P.E.R.-R.I., Petrizzo, M.R., Falzoni, F., Littler, K., Arz, J.E.A., and Russell, E.E., 2014, Evidence for global cooling in the Late

Cretaceous: Nature Communications, v. 5, p. 1–7, doi: 10.1038/ncomms5194.

Lunt, D.J., Dunkley Jones, T., Heinemann, M., Huber, M., LeGrande, A., Winguth, A., Loptson, C., Marotzke, J., Roberts, C.D., Tindall, J., Valdes, P., and Winguth, C., 2012, A model–data comparison for a multi-model ensemble of early Eocene atmosphere–ocean simulations: EoMIP: Climate of the Past, v. 8, no. 5, p. 1717–1736, doi: 10.5194/cp-8-1717-2012-supplement.

Lunt, D.J., Valdes, P.J., Jones, T.D., Ridgwell, A., Haywood, A.M., Schmidt, D.N., Marsh, R., and Maslin, M., 2010, CO2-driven ocean circulation changes as an amplifier of Paleocene-Eocene thermal maximum hydrate destabilization: Geology, v. 38, no. 10, p. 875–878, doi: 10.1130/G31184.1.

Macleod, K.G., Huber, B.T., and Isaza-Londoño, C., 2005, North Atlantic warming during global cooling at the end of the Cretaceous: Geology, v. 33, no. 6, p. 437, doi: 10.1130/G21466.1.

Maestas, Y., MacLeod, K.G., Douglas, R., Self-Trail, J., and Ward, P.D., 2003, Late Cretaceous foraminifera, paleoenvironments, and paleoceanography of the Rosario Formation, San Antonio del Mar, Baja California, Mexico: Journal of Foraminiferal Research, v. 33, no. 3, p. 179–191.

Markwick, P.J., and Valdes, P.J., 2004, Palaeo-digital elevation models for use as boundary conditions in coupled ocean–atmosphere GCM experiments: a Maastrichtian (late Cretaceous) example: Palaeogeography Palaeoclimatology Palaeoecology, v. 213, no. 1-2, p. 37–63, doi: 10.1016/j.palaeo.2004.06.015.

Miller, K.G., et al. 2005, The Phanerozoic Record of Global Sea-Level Change: Science, v. 310, no. 5752, p. 1293–1298, doi: 10.1126/science.1116412.

Moriya, K., Wilson, P.A., Friedrich, O., Erbacher, J., and Kawahata, H., 2007, Testing for ice sheets during the mid-Cretaceous greenhouse using glassy foraminiferal calcite from the mid-Cenomanian tropics on Demerara Rise: Geology, v. 35, no. 7, p. 615–618, doi: 10.1130/G23589A.1.

Norris, R.D., and Wilson, P.A., 1998, Low-latitude sea-surface temperatures for the mid-Cretaceous and the evolution of planktic foraminifera: Geology, v. 26, no. 9, p. 832-826.

Norris, R.D., Bice, K.L., Magno, E.A., and Wilson, P.A., 2002, Jiggling the tropical thermostat in the Cretaceous hothouse: Geology, v. 30, no. 4, p. 299-302.

Otto-Bliesner, B.L., and Upchurch Jr, G.R., 1997, Vegetation-induced warming of high-latitude regions during the Late Cretaceous period: Nature, v. 385, p. 804-807.

Ounis, A., Kocsis, L., Chaabani, F., and Pfeifer, H.-R., 2008, Rare earth elements and stable isotope geochemistry (δ13C and δ18O) of phosphorite deposits in the Gafsa Basin, Tunisia: Palaeogeography Palaeoclimatology Palaeoecology, v. 268, no. 1-2, p. 1–18, doi: 10.1016/j.palaeo.2008.07.005.

Pearson, P.N., Ditchfield, P.W., Singano, J., Harcourt-Brown, K.G., Nicholas, C.J., Olsson, R.K., Shackleton, N.J., and Hall, M.A., 2001, Warm tropical sea surface temperatures in the Late Cretaceous and Eocene epochs: Nature, v. 413, no. 6855, p. 481–487.

Pirrie, D., and Marshall, J.D., 1990, High-paleolatitude late Cretaceous paleotemperatures: new data from James Ross Island, Antarctica: Geology, v. 18, p. 31-34.

Poulsen, C.J., Barron, E.J, Peterson, W.H., and Wilson, P.A.,1999, A reinterpretation of mid-Cretaceous shallow marine temperatures through model-data comparison: Paleoceanography, v. 14, p. 679-697.

Poulsen, C.J., and Zhou, J., 2013, Sensitivity of Arctic Climate Variability to Mean State: Insights from the Cretaceous: Journal of Climate, v. 26, no. 18, p. 7003–7022, doi: 10.1175/JCLI-D-12-00825.1.

Poulsen, C.J., Seidov, D., Barron, E.J. and Peterson, W.H., 1998, The impact of paleogeographic evolution on the surface oceanic circulation and the marine environment within the mid-Cretaceous Tethys: Paleoceanography, v. 13, no. 5, p. 546-559.

Poulsen, C.J., Tabor, C., and White, J.D., 2015, Long-term climate forcing by atmospheric oxygen concentrations: Science, v. 348, no. 6240, p. 1238–1241, doi: 10.1126/science.1260670.

Price, G.D., and Hart, M.B., 2002, Isotopic evidence for Early to mid-Cretaceous ocean temperature variability: Marine Micropaleontology, v. 46, p. 45-48.

Price, G.D., Sellwood, B.W., and Corfield, R.M., 1998, Isotopic evidence for palaeotemperatures and depth stratification of Middle Cretaceous planktonic foraminifera from the Pacific Ocean: Geological Magazine, v. 135, no. 2, p. 183-191.

Price, G.D., Williamson, T., Henderson, R.A., and Gagan, M.K., 2012, Barremian-Cenomanian palaeotemperatures for Australian seas based on new oxygen-isotope data from belemnite rostra: Palaeogeography Palaeoclimatology Palaeoecology, v. 358-360, no. C, p. 27–39, doi: 10.1016/j.palaeo.2012.07.015.

Pucéat, E., Joachimski, M.M., Bouilloux, A., Monna, F., Bonin, A., Motreuil, S., Morinière, P., Hénard, S., Mourin, J., Dera, G., and Quesne, D., 2010, Earth and Planetary Science Letters: Earth and Planetary Science Letters, v. 298, no. 1-2, p. 135–142, doi: 10.1016/j.epsl.2010.07.034.

Pucéat, E., Lécuyer, C., Donnadieu, Y., Naveau, P., Cappetta, H., Ramstein, G., Huber, B.T., and Kriwet, J., 2007, Fish tooth δ18O revising Late Cretaceous meridional upper ocean water temperature gradients: Geology, v. 35, no. 2, p. 107, doi: 10.1130/G23103A.1.

Pucéat, E., Lécuyer, C., Sheppard, S.M.F., Dromart, G., Reboulet, S., and Grandjean, P., 2003, Thermal evolution of Cretaceous Tethyan marine waters inferred from oxygen isotope composition of fish tooth enamels: Paleoceanography, v. 18, no. 2, p. n/a–n/a, doi: 10.1029/2002PA000823.

Rosenbloom, N.A., Otto-Bliesner, B.L., Brady, E.C., and Lawrence, P.J., 2013, Simulating the mid-Pliocene Warm Period with the CCSM4 model: Geoscientific Model Development, v. 6, no. 2, p. 549–561, doi: 10.5194/gmd-6-549-2013.

Schouten, S., Hopmans, E.C., Forster, A., van Breugel, Y., Kuypers, M.M.M., and Sinninghe Damsté, J.S., 2003, Extremely high sea-surface temperatures at low latitudes during the middle Cretaceous as revealed by archaeal membrane lipids: Geology, v. 31, no. 12, p. 1069, doi: 10.1130/G19876.1.

Schouten, S., Hopmans, E.C., Schefuss, E., and Damste, J., 2002, Distributional variations in marine crenarchaeotal membrane lipids: a new tool for reconstructing ancient sea water temperatures?: Earth and Planetary Science Letters, v. 204, no. 1-2, p. 265–274.

Schönfeld, J., Sirocko, F., and Jørgensen, N.O., 1991, Oxygen isotope composition of Upper Cretaceous chalk at Lägerdorf (NW Germany): its original environmental signal and palaeotemperature interpretation: Cretaceous Research, v.12, p. 27-46.

Sellwood, B.W., Price, G.D., and Valdest, P.J., 1994, Cooler estimates of Cretaceous temperatures: Nature, v. 370, p. 453-455.

Sewall, J.O., van de Wal, R.S.W., van der Zwan, K., van Oosterhout, C., Dijkstra, H.A., and Scotese, C.R., 2007, Climate model boundary conditions for four Cretaceous time slices: Climate of the Past, v. 3, no. 4, p. 647–657.

Spicer, R.A., and Herman, A.B., 2010, The Late Cretaceous environment of the Arctic: A quantitative reassessment based on plant fossils: Palaeogeography Palaeoclimatology Palaeoecology, v. 295, no. 3-4, p. 423–442, doi: 10.1016/j.palaeo.2010.02.025.

Spicer, R.A., Ahlberg, A., Herman, A.B., Hofmann, C.C., Raikevich, M., Valdes, P.J., and Markwick, P.J., 2008, The Late Cretaceous continental interior of Siberia: A challenge for climate models: Earth and Planetary Science Letters, v. 267, no. 1-2, p. 228–235, doi: 10.1016/j.epsl.2007.11.049.

Steuber, T., Rauch, M., Masse, J.P., Graaf, J., and Malkoč, M., 2005, Low-latitude seasonality of Cretaceous temperatures in warm and cold episodes: Nature, v. 437, no. 7063, p. 1341–1344, doi: 10.1038/nature04096.

Taylor, K.W.R., Huber, M., Hollis, C.J., Hernandez-Sanchez, M.T., and Pancost, R.D., 2013, Global and Planetary Change: Global and Planetary Change, v. 108, no. C, p. 158–174, doi: 10.1016/j.gloplacha.2013.06.011.

Upchurch, G.R., Otto-Bliesner, B.L., and Scotese, C., 1998, Vegetation–atmosphere interactions and their role in global warming during the latest Cretaceous: Philosophical Transactions of the Royal Society of London B, v. 353, p. 97-112.

Upchurch, G.R., Jr, Kiehl, J., Shields, C., Scherer, J., and Scotese, C., 2015, Latitudinal temperature gradients and high-latitude temperatures during the latest Cretaceous: Congruence of geologic data and climate models: Geology, v. 43, no. 8, p. 683–686, doi: 10.1130/G36802.1.

Vellekoop, J., Sluijs, A., Smit, J., Schouten, S., Weijers, J.W.H., Sinninghe Damste, J.S., and Brinkhuis, H., 2014, Rapid short-term cooling following the Chicxulub impact at the Cretaceous-Paleogene boundary: Proceedings of the National Academy of Sciences, v. 111, no. 21, p. 7537–7541, doi: 10.1073/pnas.1319253111.

Voigt, S., Gale, A.S., and Flögel, S., 2004, Midlatitude shelf seas in the Cenomanian-Turonian greenhouse world: Temperature evolution and North Atlantic circulation: Paleoceanography, v. 19, no. 4,, doi: 10.1029/2004PA001015.

Voigt, S., Wilmsen, M., Mortimore, R.N., and Voigt, T., 2003, Cenomanian palaeotemperatures derived from the oxygen isotopic composition of brachiopods and belemnites: evaluation of Cretaceous palaeotemperature proxies: International Journal of Earth Science. doi: 10.1007/s00531-003-0315-1.

Wang, Y., Huang, C., Sun, B., Quan, C., Wu, J., and Lin, Z., 2014, Earth-Science Reviews: Earth-Science Reviews, v. 129, no. C, p. 136–147, doi: 10.1016/j.earscirev.2013.11.001.

Wilson, P.A., and Opdyke, B.N., 1996, Equatorial sea-surface temperatures for the Maastrichtian revealed through remarkable preservation of metastable carbonate: Geology, v. 24, no. 6, p. 555-558.

Zakharov, Y.D., Popov, A.M., and Shigeta, Y., 2006, New Maastrichtian oxygen and carbon isotope record: additional evidence for warm low latitudes: Geosciences Journal, v. 10, no. 3, p. 347-367.

Zhou, J., Poulsen, C.J., pollard, D., and White, T.S., 2008, Simulation of modern and middle Cretaceous marine delta O-18 with an ocean-atmosphere general circulation model: Paleoceanography, v. 23, no. 3, doi: 10.1029/2008PA001596.

Zhou, J., Poulsen, C.J., Rosenbloom, N., Shields, C., and Briegleb, B., 2012, Vegetation-climate interactions in the warm mid-Cretaceous: Climate of the Past, v. 8, no. 2, p. 565–576, doi: 10.5194/cp-8-565-2012.

Shackleton, N.J., Kennett, J.P., 1975, Paleotemperature history of the Cenozoic and the initiation of Antarctic glaciation: Oxygen and carbon isotope analyses in DSDP sites 277, 279, and 281: DSDP 729, doi:10.2973/dsdp.proc.29.117.1975.

Zachos, J.C., Stott, L.D., and Lohmann, K.C., 1994, Evolution of early Cenozoic marine temperatures: Paleoceanography, v. 9, no. 2, p. 353-387.

Chapter 6: Conclusions and Future Work

Below I summarize the major finding of Chapters 2-5, highlight the key questions answered by my dissertation, and discuss continuing and future research.

6.1 Summary of results

Chapter 2: By independently forcing the Earth System model with cycles of obliquity and precession, I show that Northern Hemisphere high-latitude summer temperature changes with changes in orbit are not exclusively controlled by the amount of summer insolation. Instead, obliquity dominated changes in annual average high-latitude insolation enhances vegetation and sea-ice responses relative to precession. These feedbacks amplify the high-latitude surface albedo response and in turn, the summer surface temperature sensitivity to obliquity forcing. As a result, the model produces a larger ice-volume response to changes in obliquity than would be anticipated from summer insolation changes alone and helps resolve why the ice-volume response to obliquity is so much greater than precession. Consequently, June 65°N insolation, which is commonly employed in Milankovitch forcing experiments, does a poor job of forecasting the ice-volume response to orbital changes. Further, Chapter 2 demonstrates the importance of using complex Earth system models to explore problems in paleoclimatology. For example, previous modeling studies on the subject did not include dynamic vegetation and therefore, did not capture this important feedback.

Chapter 3: This chapter builds upon the findings of Chapter 2. Here I vary obliquity and precession simultaneously in a series of orbital configurations to explore North American land-ice responses under more realistic orbital scenarios. The results of Chapter 3 demonstrate that the surface albedo feedbacks, which amplified high-latitude climate sensitivity to obliquity cycles in Chapter 2, remain under high eccentricity and varying precession. I also show that spring and fall seasonal offsets of precession forcing have a small impact on ice-volume and are of secondary importance to changes in summer insolation. Finally, my results illustrate that cycle duration differences between obliquity and precession, in combination with signal amplification from albedo feedbacks, allow obliquity to produce about 60% of the ice-volume power. If I modulate the precession ice-volume component by eccentricity or including a small ice-volume response from Antarctica, the global ice-volume spectral power shifts almost completely to the obliquity cycle frequency, in agreement with early Pleistocene ice-volume proxy records.

Chapter 4: In this chapter, I explore the hypothesis that gradual removal of regolith in the high-latitudes of North American by multiple cycles of ice advance and retreat caused the MPT. I find that a low shear regolith bed allows for thin, extensive ice sheets that follow the 41 kyr cycles of obliquity, while high shear crystalline bedrock produces thicker, more sluggish ice sheets that only completely retreat from the combined high summer insolation forcing of obliquity and precession. With a reduction in basal sliding, a shift occurs in the modeled ice-volume cycles from 41 kyr to 100 kyr power, which agrees with ice-volume proxy records. As in previous chapters, climate feedbacks are important for amplifying the ice sheet responses. The thicker ice sheets produced from greater basal drag have colder surface temperatures, receive more snowfall, and have a smaller ablation zone, which makes them more resistant to moderate summer insolation increases. Surprisingly, model experiments that include transient CO_2 forcing do not show a significantly different ice-volume response from those with fixed CO_2, suggesting that CO_2 forcing was of secondary importance to the MPT.

Chapter 5: Here I investigate the role of paleogeography and CO_2 in the proxy identified cooling of the Late Cretaceous using two climate models with detailed paleogeographies of the Cenomanian and Maastrichtian, and a comprehensive compilation of SST proxy records. My results show that the Late Cretaceous cooling was global and likely the result of a reduction in CO_2, not changes in geography. In both models, a reduction in CO_2 from the Cenomanian to Maastrichtian results in a global cooling of ~3°C and significant polar amplification. Given model sensitivity and proxy temperature reconstructions, I propose that CO_2 decreased by more than 75% from the Cenomanian to Maastrichtian. Even though geographic changes cannot explain the Late Cretaceous cooling, they do cause significant regional climate changes that must be considered when interpreting long-term proxy records. Despite model agreement in the climate responses with changes in geography and CO_2, some model/proxy temperature discrepancies remain, especially in the high-latitude continental interiors.

6.2 Key findings

My dissertation highlights the value of Earth system models to understanding Earth's climate history. While proxy records provide a wealth of information about past climates, their spatial and temporal coverage remain limited. Model simulations help fill these gaps in our global understanding by providing dynamically feasible solutions to problems in paleoclimatology. More specifically, my dissertation stresses the importance of model complexity. Often, paleoclimate simulations use reduced complexity due to high computational cost. However, reduced complexity oversimplifies the Earth system, which can be particularly erroneous when studying paleoclimatology. I find several important feedbacks in my research that are often neglected by the paleoclimate modeling community. Yet, despite relatively greater complexity, my experiments also lack some potentially important aspects of the Earth system, which limit my conclusions. Heading forward, more proxy records, reduced model parameterization, and additional model intercomparison will be necessary to advance our understanding of the past. By doing so, we will be able to better understand our future.

Below, I summarize important questions in paleoclimatology answered by my dissertation:

1) **What produced the 41 kyr glacial cycles of the early Pleistocene?**

My research shows that no single factor led to the 41 kyr glacial cycles of the early Pleistocene. Instead, amplification of the obliquity forcing by high-latitude albedo feedbacks, seasonal offset of the precession forcing, and differences in orbital cycle duration all act to amplify the ice-volume response to obliquity relative to precession. As a result, creating the "41 kyr world" of the early Pleistocene only requires a small amount of hemispheric offset in the global ice-volume response to precession.

2) **What led to the appearance of a 100 kyr ice-volume cycle?**

Several hypotheses exist for the appearance of a 100 kyr ice-volume cycle between 1.2 and 0.7 Ma. Using a complex Earth system model, I show that the regolith hypothesis for the MPT can simulate the appearance of an eccentricity ice-volume signal. Further, my results do not support the common alternative MPT hypotheses that draw-down of CO_2 or changes in CO_2 cycling led to the appearance of the 100 kyr ice-volume cycles.

3) **What caused Late Cretaceous cooling?**

My compilation of proxy SST records suggests that the Late Cretaceous cooling was a global phenomenon. Model simulations of the Cenomanian and Maastrichtian do not show a significant global temperature response to changes paleogeography, despite large regional differences. In contrast, a simulated reduction in CO_2 matches the proxy inferred cooling well. Therefore, I propose that the Late Cretaceous cooling was in response to a reduction in GHG concentrations, not feedbacks relating to geographic change.

6.3 Continuing and future work

This dissertation helps clarify several outstanding questions in paleoclimatology. However, there are many additional questions associated with these topics that I am currently researching or plan to begin researching in the near future.

1) **Reevaluating the ice-volume proxy records**

In all of my Pleistocene ice-volume cycle experiments, I use $\delta^{18}O$ values from foraminifera in deep-sea sediments to define the glacial cycles (Lisiecki and Raymo, 2005). I assume these measurements linearly record the global ice-volume signal, but this might not be strictly true (Elderfield et al., 2012). $\delta^{18}O$ values capture both temperature and land-ice changes, and studies suggest that ocean overturning responds differently and inconsistently to changes in obliquity and precession through time (Lisiecki et al., 2008; Rohling et al., 2014). Therefore, deep-ocean $\delta^{18}O$ records may not simply reflect changes in ice-volume. I plan to test the validity of this common assumption using POP2 ocean model with prognostic water isotopologue calculations under a series of different orbital and mean-state conditions. Model results will allow for better interpretation of Plio-Pleistocene $\delta^{18}O$ records and improve our understanding of the climate dynamics that led to key glacial and interglacial periods of the Pleistocene.

2) **The role of vegetation in the Late Cretaceous**

In the Late Cretaceous experiments presented here, dynamic vegetation comes from present-day plant functional types where flowering plants make up about 80 % of all floras. However, paleobotanical research suggests that proliferation of angiosperms did not occur until the early-to-mid-Cretaceous (Coiffard et al., 2012). Because angiosperms have significantly greater conductance than gymnosperms, their appearance and eventual dominance potentially had a profound impact on continental climate (Boyce et al., 2009). Idealized removal of angiosperms in present-day model simulations leads to tropical drying and warming (Boyce et al., 2010). I plan to simulate this vegetation transition with more realistic Cenomanian and Maastrichtian boundary conditions in an attempt to explain the low-latitude cooling and mid-latitude moistening observed over this period.

3) **Late Cretaceous ocean circulation changes**

Even though I find that changes in geography across the Late Cretaceous were not responsible for the proxy identified global cooling, neodymium isotopic records suggest significant changes in ocean circulation over this period (Robinson and Vance, 2012). To understand the mechanisms responsible for these apparent circulation shifts, I will use the Cretaceous model results presented here with an offline neodymium isotope tracer model (Arsouze et al., 2006) to explore ocean circulation changes in the latest Cretaceous. Model results will help determine if latest Cretaceous circulation changes were due to changes in geography, GHG concentrations, or neodymium sources.

You made it. Congratulations!

Bibliography

Arsouze, T., J. Dutay, F. Lacan, and C. Jeandel (2007), Modeling the neodymium isotopic composition with a global ocean circulation model, Chem. Geo., 239(1-2), 165–177, doi:10.1016/j.chemgeo.2006.12.006.

Boyce, C. K., T. J. Brodribb, T. S. Feild, and M. A. Zwieniecki (2009), Angiosperm leaf vein evolution was physiologically and environmentally transformative, Proc. Royal Soc, B: Bio. Sci., 276(1663), 1771–1776, doi:10.1080/00241160310004657.

Boyce, C. K., and J. E. Lee (2010), An exceptional role for flowering plant physiology in the expansion of tropical rainforests and biodiversity, Proc. Royal Soc. B: Bio. Sci., 277(1699), 3437–3443, doi:10.1080/00241160310004657.

Coiffard, C., B. Gomez, V. Daviero-Gomez, and D. L. Dilcher (2012), Rise to dominance of angiosperm pioneers in European Cretaceous environments, Proc. Nat. Acad. Sci., 109(51), 20955–20959, doi:10.1073/pnas.1218633110.

Elderfield, H., P. Ferretti, M. Greaves, S. Crowhurst, I. N. McCave, D. Hodell, and A. M. Piotrowski (2012), Evolution of ocean temperature and ice volume through the mid-Pleistocene climate transition, Science, 337(6095), 704–709, doi:10.1126/science.1221294.

Lisiecki, L. E., and M. E. Raymo (2005), A Pliocene-Pleistocene stack of 57 globally distributed benthic delta O-18 records, Paleoceanography, 20(1), doi:10.1029/2004PA001071.

Lisiecki, L.E., M.E. Raymo, and W.B. Curry, (2008). Atlantic overturning responses to Late Pleistocene climate forcings. Nature. doi:10.1038/nature07425

Poulsen, C. J., E. J. Barron, W. H. Peterson, and P. A. Wilson (1999), A reinterpretation of mid-Cretaceous shallow marine temperatures through model-data comparison, Paleoceanography, 14(6), 679-697.

Robinson, S. A., and D. Vance (2012), Widespread and synchronous change in deep-ocean circulation in the North and South Atlantic during the Late Cretaceous, Paleoceanography, 27(1), doi:10.1029/2011PA002240.

Rohling, E. J. et al. (2013), Making sense of paleoclimate sensitivity, Nature, 1–10, doi:10.1038/nature11574.